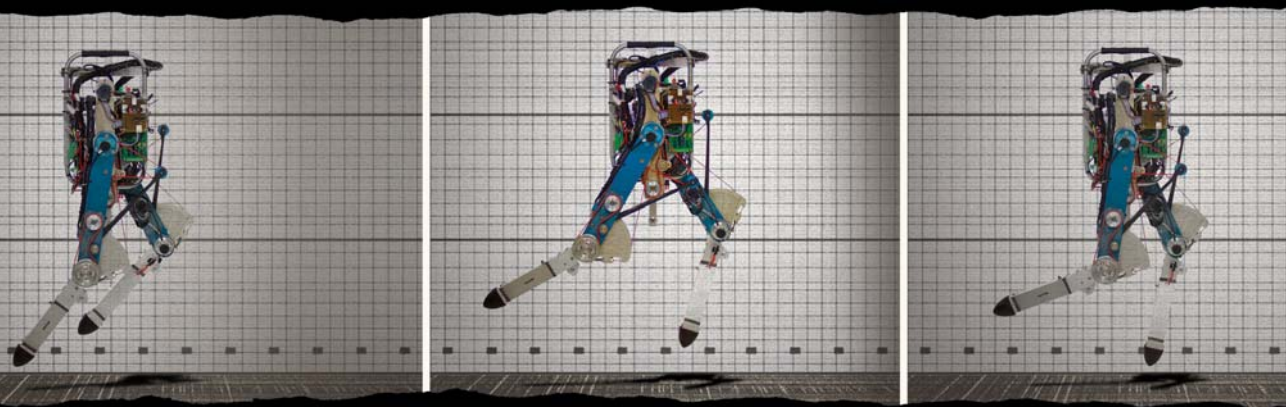


Robotic **Bipedal** Running



Daniël Karssen

Robotic Bipedal Running

Increasing disturbance rejection

J.G.D. Karssen

Robotic Bipedal Running

Increasing disturbance rejection

Proefschrift

ter verkrijging van de graad van doctor
aan de Technische Universiteit Delft,
op gezag van de Rector Magnificus, prof. ir. K.C.A.M. Luyben,
voorzitter van het College voor Promoties
in het openbaar te verdedigen op vrijdag 18 januari 2013 om 12:30 uur
door

Johannes Gerhard Daniël KARSSSEN

werktuigkundig ingenieur
geboren te Naarden

Dit proefschrift is goedgekeurd door de promotor:

Prof. dr. F.C.T. van der Helm

Copromotor: Dr. ir. M. Wisse

Samenstelling promotiecommissie:

Rector Magnificus	voorzitter
Prof. dr. F.C.T. van der Helm	Technische Universiteit Delft, promotor
Dr. ir. M. Wisse	Technische Universiteit Delft, copromotor
Prof. dr. ir. H. van der Kooij	Universiteit Twente, Technische Universiteit Delft
Prof. dr. ir. J.L. Herder	Technische Universiteit Delft, Universiteit Twente
Prof. dr. ir. J.M.A. Scherpen	Rijksuniversiteit Groningen
Prof. dr. K. Mombaur	Ruprecht-Karls-Universität Heidelberg, Duitsland
Dr. A.J. van Soest	Vrije Universiteit Amsterdam
Prof. dr. H.E.J. Veeger	Technische Universiteit Delft, Vrije Universiteit Amsterdam, reservelid

This research was financially supported by the Dutch Technology Foundation STW (project number DW07462).



ISBN 978-94-6186-110-8

A digital copy of this thesis can be downloaded from <http://repository.tudelft.nl>.

Contents in brief

Summary	xiii
Samenvatting	xv
1. Introduction	1
2. Nonlinear Leg Stiffness	9
3. Center-of-Mass Offset	33
4. Running Robot Phides	57
5. Swing-Leg Retraction on Simple Models	75
6. Swing-Leg Retraction on Realistic Models	93
7. Discussion, conclusions and future directions	129
Appendix A. Foot placement control	139
References	159
Acknowledgements	169
About the author	171
Propositions	173
Stellingen	175

Contents

Summary	xiii
Samenvatting	xv
1. Introduction	1
1.1 Motivation	2
1.2 Gait synthesis	3
1.3 Overview of research field	3
1.3.1 Spring leg runners	4
1.3.2 Running humanoids	4
1.4 Problem statement	5
1.5 Research goal	6
1.6 Approach	6
1.7 Thesis outline	8
2. Nonlinear Leg Stiffness	9
2.1 Introduction	10
2.2 Nonlinear spring-mass model	11
2.3 Disturbance rejection measures	13
2.3.1 Largest allowable disturbance	14
2.3.2 Largest allowable random disturbances	14
2.3.3 Basin of attraction	15
2.3.4 Floquet multipliers	15
2.3.5 Gait Sensitivity Norm	15
2.3.6 Selected measures	18
2.4 Optimization	19
2.4.1 Optimization procedure	19
2.4.2 Optimal nonlinear stiffness	21
2.4.3 Optimal linear stiffness	23
2.5 Disturbance rejection of optimal linear and nonlinear stiffness profiles	23
2.6 Discussion	24
2.6.1 Explanation of the improved disturbance rejection	24
2.6.2 Applicability	29
2.6.3 Parameter Sensitivity	29
2.6.4 Effect of the energy level	30
2.6.5 Comparisons with related studies	30
2.7 Conclusion	31

3. Center-of-Mass Offset	33
3.1 Introduction	34
3.2 Disturbance rejection	35
3.3 Model	36
3.3.1 Torque parameterization	37
3.3.2 Equations of motion	37
3.3.3 Events	38
3.3.4 Parameter values	39
3.4 Limit cycle analysis	39
3.5 The largest 1-step controllable disturbance	41
3.5.1 The general problem	41
3.5.2 Simplification 1: Only torque limit	42
3.5.3 Simplification 2: Linearization	42
3.6 Results	43
3.7 Discussion	45
3.7.1 Parameter variations	46
3.7.2 Two-step strategies	49
3.7.3 Validation of simplifications	51
3.7.4 Limitations	53
3.8 Conclusion	55
4. Running Robot Phides	57
4.1 Introduction	58
4.2 Overall design layout	59
4.3 Mechanical realization	61
4.4 Controller	64
4.4.1 Electronics	64
4.4.2 Control architecture	66
4.5 Results	67
4.5.1 Gait characteristics	67
4.5.2 Motions	69
4.5.3 Knee actuation performance	71
4.6 Conclusion	72

5. Swing-Leg Retraction on Simple Models	75
5.1 Introduction	76
5.2 Simulation Model	77
5.3 Disturbance rejection	79
5.3.1 Stability	80
5.3.2 Single disturbance	81
5.3.3 Multiple disturbances	84
5.3.4 Parameter variations	85
5.4 Other Benefits	85
5.4.1 Foot speed	86
5.4.2 Impact losses	86
5.4.3 Slipping	87
5.4.4 Impact forces	88
5.5 Discussion	88
5.5.1 Optimal retraction rates	88
5.5.2 Implications for running robots	88
5.5.3 Implementation of swing-leg retraction on running robots	90
5.6 Conclusions	90
6. Swing-Leg Retraction on Realistic Models	93
6.1 Introduction	94
6.2 Models and Experimental Platform	96
6.2.1 SLIP model	97
6.2.2 Realistic model	99
6.2.3 Physical Robot	103
6.3 Impact Losses	105
6.3.1 Methods	105
6.3.2 Results	105
6.3.3 Discussion	106
6.4 Overall Energetic Efficiency	108
6.4.1 Methods	108
6.4.2 Results	110
6.4.3 Discussion	112
6.5 Impact Forces and Footing Stability	112
6.5.1 Methods	112
6.5.2 Results	113
6.5.3 Discussion	114
6.6 Stability	115
6.6.1 Method	115

6.6.2	Results	115
6.6.3	Discussion	117
6.7	Disturbance rejection	117
6.7.1	Method	117
6.7.2	Results	119
6.7.3	Discussion	122
6.8	Discussion	123
6.8.1	Realistic model validation	123
6.8.2	Effect of starting point	124
6.8.3	Are the trends of the models consistent?	126
6.8.4	Optimal retraction rate	127
6.9	Conclusion	128
7.	Discussion, conclusions and future directions	129
7.1	Recapitulation	130
7.2	Discussion	131
7.2.1	Transfer of results from simple models to realistic models and robots	131
7.2.2	Understanding of the human running gait to improve orthoses and prostheses	132
7.2.3	Addition of feet	134
7.3	Conclusions	135
7.4	Future directions	136
7.4.1	Combining	136
7.4.2	Extending	136
7.4.3	Applying	137
Appendix A.	Foot placement control	139
A.1	Introduction	140
A.2	Model description	141
A.2.1	Equations of motion	142
A.2.2	Stepping constraints	144
A.3	Walking gait	145
A.4	Control problem	145
A.5	Dynamic Foot Placement controller	149
A.5.1	0-step strategy	149
A.5.2	1-step strategy	149
A.5.3	2-step strategy	151
A.5.4	$(N > 2)$ -step strategy	152

A.6 Control performance	152
A.6.1 Number of steps	152
A.6.2 Time response	154
A.7 Discussion	155
A.8 Conclusion	157
References	159
Acknowledgements	169
About the author	171
Propositions	173
Stellingen	175

Summary

Robotic Bipedal Running

Increasing disturbance rejection

The goal of the research presented in this thesis is to increase the understanding of the human running gait. The understanding of the human running gait is essential for the development of devices, such as prostheses and orthoses, that enable disabled people to run or that enable able people to increase their running performance. Although these devices are currently being developed, there is not much insight yet in the fundamentals of the running gait. This fundamental knowledge is required for improving these devices. One of the big unknowns is how these devices affect the ability of the user to handle disturbances, like sudden pushes or variations in floor height.

To gain insight in the fundamentals of the human running gait and the disturbance rejection behavior in particular, the gait synthesis approach is taken. In this approach, the running gait is studied by synthesizing the human running on simulation models and on robots. This allows studying the effects of specific system parameters in a simplified and controlled environment. A number of simulation models and a physical running robot have been developed. The simulation models vary in complexity, from simple simulation models based on the well-known spring loaded inverted pendulum (SLIP) model to simulation models that closely resemble the physical running robot. The simple simulation models are useful to get fundamental insights, due to their simple dynamics. The results of the simple models are validated with the more realistic models and physical running robot.

This thesis focuses on the effect of three important system parameters on the disturbance rejection behavior. These three parameters are: the leg stiffness profile, the location of the center-of-mass, and the swing-leg retraction rate. These three parameters were selected, based on our experience with walking robots. The research in this thesis shows that the effects of these parameters are the following.

The *leg stiffness profile* has a significant influence on the disturbance rejection behavior. For a simple running model, we show that nonlinear leg springs can improve the disturbance rejection up to a factor 7 compared to the optimal linear leg spring. The optimal leg stiffness profile for the maximal disturbance rejection behavior is strongly nonlinear. These results show that the generally used linear leg springs are far from optimal in terms of disturbance rejection behavior.

The *location of the center-of-mass* of the torso also has a large influence on the disturbance rejection. The optimal center-of-mass location depends on the type of

the expected disturbance, which is above the hip for floor height disturbances and below the hip for push disturbances on the center-of-mass. The commonly used center-of-mass location at the hip is far from optimal. An offset of the center-of-mass location can increase the disturbance rejection up to a factor 10 compared to the center-of-mass at the hip.

The *swing-leg retraction rate*, the speed of the backwards rotation of the front leg prior to touchdown, affects the disturbance rejection rate. We show that this effect is maximal at a mild retraction rate, which is much lower than the retraction rate for ground speed matching. The optimal retraction rate decreases with increasing running velocity. Besides improving disturbance rejection, swing-leg retraction can also reduce energetic losses, impact forces, and the risk of slipping. However, we show that all of the benefits of swing-leg retraction occur at different retraction rates, which indicates that there is an inherent tradeoff to consider when selecting the retraction rate for a robot control system. In addition, the effect of the retraction rate on these benefits is strongly model and/or parameter dependent, making it difficult to make general rules on how to select the retraction rate.

Besides the above-mentioned results, this research also revealed the following insights. Firstly, not all results from simple running model studies transfer well to more realistic models and robots. This is especially the case for studies on effects that involve impact dynamics, as impact dynamics greatly depend on the leg morphology. Secondly, the gait sensitivity norm, the disturbance rejection measured introduced by Hobbelen for walking systems, is also suitable for running systems. Finally, the implementation of a spring in parallel with the actuator in the knee joint can greatly reduce the required actuator torque and power.

Overall, the results of this thesis show that there are many opportunities to improve the disturbance rejection performance of bipedal running robots. This can be done either by mechanical changes to the robotics system, e.g. implementing a nonlinear leg spring or placing the center-of-mass away from the hip, or by changes to the controller, e.g. implementing swing-leg retraction. The results of this thesis also point out promising directions for the development of better running orthoses and prostheses. Most promising is the implementation of nonlinear springs in exoskeletons, because the results show a large improvement in the disturbance rejection behavior and because nonlinear springs are relatively easy to implement in exoskeletons.

Samenvatting

Robotisch tweebenig rennen

Het verbeteren van het verstoringsgedrag

Het onderzoek dat in dit proefschrift wordt gepresenteerd heeft als doel de menselijke renbeweging beter te begrijpen. Het begrijpen van de menselijke renbeweging is noodzakelijk voor de ontwikkeling van hulpmiddelen die gehandicapte mensen laten rennen, zoals hardloopportheses, en voor hulpmiddelen die gezonde mensen beter laat rennen. Deze hulpmiddelen worden nu al ontwikkeld, maar het ontbreekt nog aan fundamenteel inzicht in de renbeweging. Een grote onbekende factor is wat de invloed van deze hulpmiddelen is op hoe goed de gebruiker om kan gaan met verstoringen, zoals een onverwachte duw of hoogteverschillen in de ondergrond.

Om meer inzicht te krijgen in de menselijke renbeweging en het verstoringsgedrag in het bijzonder, analyseren we de renbeweging met behulp van simulatiemodellen en robots. Deze onderzoeksaanpak heeft als voordeel, boven het analyseren van rennende mensen, dat geselecteerde parameters kunnen worden onderzocht in een gecontroleerde en versimpelde omgeving. Voor dit onderzoek zijn een aantal simulatiemodellen en een robot ontwikkeld. De simulatiemodellen variëren in complexiteit, van zeer vereenvoudigde simulatiemodellen tot gedetailleerde simulatiemodellen van de robot. De vereenvoudigde simulatiemodellen worden gebruikt voor het verkrijgen van fundamentele inzichten, die vervolgens worden gevalideerd met behulp van de gedetailleerde simulatiemodellen en de robot.

Dit onderzoek richt zich op de invloed van drie belangrijke parameters op het verstoringsgedrag. Deze parameters zijn: het stijfheidsprofiel van de beenveer, de locatie van het massazwaartepunt en de rotatiesnelheid van het zwaaibeen. De keuze voor deze parameters is gebaseerd op onze ervaring met lopende robots. De resultaten van het onderzoek naar deze parameters zijn als volgt.

Het *stijfheidsprofiel van de beenveer* heeft een significante invloed op het verstoringsgedrag. Het onderzoek laat zien dat, voor een vereenvoudigd simulatiemodel, met niet-lineaire beenveren het verstoringsgedrag wel 7 keer beter kan zijn dan mogelijk is met de beste lineaire beenveren. Het stijfheidsprofiel dat het beste verstoringsgedrag geeft is zeer niet lineair. Deze resultaten laten zien dat de lineaire veren, die nu voornamelijk worden gebruikt, zorgen voor een verre van optimaal verstoringsgedrag.

De *locatie van het massazwaartepunt* van het bovenlichaam heeft ook een grote invloed op het verstoringsgedrag. De optimale locatie voor het zwaartepunt hangt af van welk soort verstoringen er zijn. Voor verstoringen in de vloerhoogte is de optimale locatie boven de heup en voor duwverstoringen is de optimale locatie onder

de heup. Veel robots hebben een massazwaartepunt precies op de heup, wat zorgt voor een sterk verminderd verstoringsgedrag. Door het massazwaartepunt niet op de heup te leggen kan het verstoringsgedrag tot wel 10 keer beter worden.

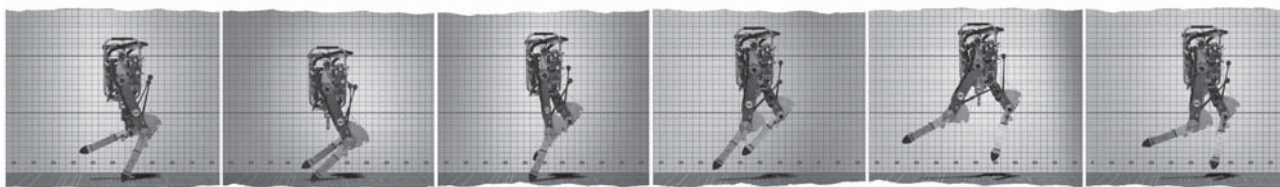
Het *roteren van het zwaaibeen* vlak voordat het been de grond raakt beïnvloed het verstoringsgedrag, omdat het de beenhoek bij het neerkomen afhankelijk maakt van wanneer het been de grond raakt. Uit het onderzoek blijkt dat het optimaal is om het been langzaam achterwaarts te zwaaien, met een rotatiesnelheid die langzamer is dan de rotatiesnelheid die nodig is om de voet ten opzichte van de grond stil te houden. Naast het verbeteren van het verstoringsgedrag heeft het achterwaarts zwaaien van het been ook als voordeel dat de krachten en de energieverliezen bij het neerkomen worden verminderd. Alleen de rotatiesnelheid waarbij dit maximaal werkt is anders dan voor het verbeteren van het verstoringsgedrag. Dit geeft aan dat een afweging gemaakt moet worden tussen de verschillende voordelen bij het maken van een keuze voor de rotatiesnelheid. Tevens is het effect van de rotatiesnelheid op de voordelen sterk afhankelijk van de beenmorfologie en de massaverdeling, wat het lastig maakt om een richtlijn te geven voor het selecteren van de beste rotatiesnelheid.

Naast de bovengenoemde resultaten heeft dit onderzoek nog de volgende inzichten opgeleverd. Ten eerste heeft dit onderzoek tevens laten zien dat niet alle resultaten van onderzoek met sterk vereenvoudigde renmodellen opgaan voor meer realistische renmodellen en robots. Dit is voornamelijk het geval voor onderzoek dat betrekking heeft op wat er gebeurt als de voet contact met de grond maakt, omdat dit gedrag sterk afhankelijk is van de beenmorfologie. Ten tweede is gebleken dat de 'gait sensitivity norm', een maat voor het verstoringsgedrag van lopende robots die door Hobbelen is geïntroduceerd, ook geschikt is voor het kwantificeren van het verstoringsgedrag van rennende robots. Als laatste heeft dit onderzoek ook laten zien dat het gebruik van een veer parallel met de motor in de kniegewrichten het vereiste motorkoppel en motorvermogen sterk kan verminderen.

Samenvattend laten de resultaten uit dit proefschrift zien dat er veel mogelijkheden zijn voor het verbeteren van het verstoringsgedrag van tweebeinige rennende robots. De verbeteringen kunnen komen door mechanische aanpassingen, zoals het toepassen van niet lineaire veren of het verplaatsen van het massazwaartepunt, of door veranderingen aan de regelaar, bijvoorbeeld door het been achterwaarts te laten zwaaien vlak voordat de robot contact maakt met de grond. De resultaten uit dit proefschrift geven tevens mogelijke opties voor het verbeteren van renhulpmiddelen. De meest veelbelovende optie is het toepassen van niet lineaire veren in exoskeletten, want niet lineaire beenveren lieten een grote verbetering van het verstoringsgedrag zien en het implementeren van niet lineaire veren in exoskeletten is relatief gemakkelijk.

1

Introduction



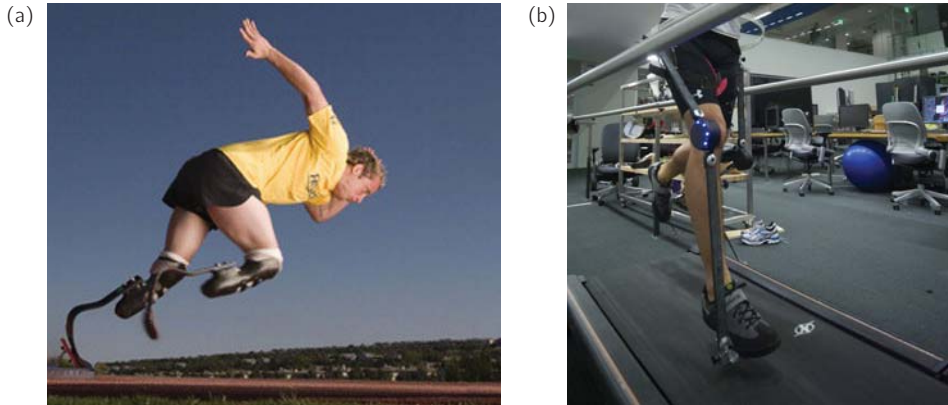


Figure 1.1: Two examples of devices that improve the running performance. (a) The Cheetah Flex-Foot by Össur, which enables lower leg amputees to run (Össur, 2012). (b) The leg exoskeleton by Elliott (2012), which aims to reduce the metabolic cost of running.

1.1 Motivation

The goal of the research presented in this thesis is to increase the understanding of the human running gait. The understanding of the human running gait is essential for the development of devices, such as prostheses and orthoses, that enable disabled people to run or that enable able people to increase their running performance.

Recently, prostheses and orthoses have been developed specifically for running. The most famous running prosthesis is the Cheetah Flex-Foot by Össur (Figure 1.1a), which is a lower leg prosthesis (for below-knee amputees). With this prosthesis, the runner Oscar Pistorius managed to reach the semifinals of the 400m at the normal Olympics in 2012. Also recently, Elliott (2012) developed a leg exoskeleton that aims to decrease the metabolic cost of running (Figure 1.1b). This exoskeleton does not yet decrease the metabolic cost of running, but it has shown to decrease the metabolic cost of hopping in place (Grabowski and Herr, 2009).

Although these devices are currently being developed, there is not much insight yet into the fundamentals of the running gait. This fundamental knowledge is required for improving these devices. One of the big unknowns is how these devices affect the ability of the user to handle disturbances, like sudden pushes or floor height variations. From the research into the walking gait, it is known that disturbance rejection is one of the key challenges of bipedal locomotion (Hobbelen and Wisse, 2007a).

1.2 Gait synthesis

The human running gait is commonly studied with *gait analysis*. In gait analysis, the running gait is studied by analyzing the gait parameters of a running human under a variety of circumstances. However, in this research we use *gait synthesis* instead of gait analysis. In gait synthesis, the running gait is studied by synthesizing the human running on simulation models and on robots. We use gait synthesis as it has the following two advantages over gait analysis.

The main advantage of gait synthesis over gait analysis is that it allows studying the effects of specific system parameters in a simplified and controlled environment. In simulation and robot experiments, it is possible to include only the essential elements, whereas in human experiments the full complexity has to be taken into account. For example, in all studies presented in this thesis, the models and robots are limited to 2-dimensional motion, something that is almost impossible in human experiments. In addition, the simulation and robot experiments are more controlled and transparent than human experiments, as the control used by humans is largely unknown and hard to affect. This makes it easier to find the cause of a studied effect in a simulation or robot experiment.

A second advantage of gait synthesis is that in simulation and robot experiments data can be easier collected than in human experiments, which allows more quantifiable studies. In human experiments, it can be difficult or even impossible to measure all relevant quantities, like the amount of control effort. In addition, a fewer number of experiments are needed with simulation and robot experiments as they have a higher repeatability than human experiments. Finally, simulation experiments take less time in general, as they can run in parallel and often run faster than real-time.

Although gait synthesis has the above-mentioned advantages over gait analysis, it should be used in conjunction with gait analysis. Gait analysis can be used to validate the results of gait synthesis. The insights gathered with gait synthesis can be used in gait analysis, by using the gained insights to focus on specific gait characteristics in gait analysis. At the end of this thesis, in Section 7.2.2, it is discussed how the results of this thesis can be used in gait analysis.

1.3 Overview of research field

Over the years, synthesis of the running gait has been performed with a wide variety of robots. These robots have different levels of complexity, which vary from the simple hopping robots by Raibert (1986) to complete humanoids like Asimo (Hirose and

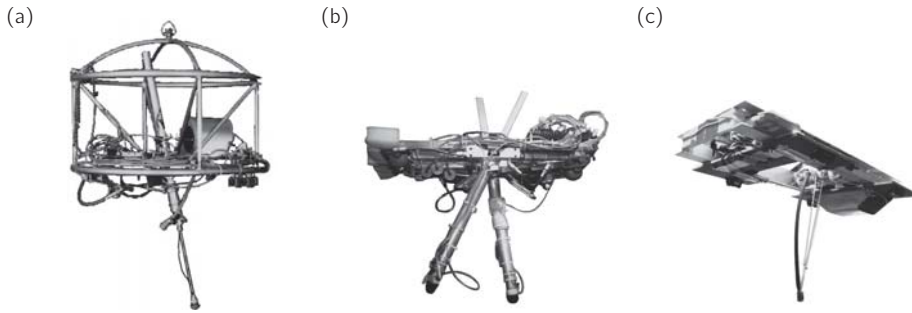


Figure 1.2: Three examples of spring leg runners. (a) 3D Hopper by Raibert (1986). (b) Planer Biped by Hodgins et al. (1986). (c) Bow Leg Hopper by Zeglin and Brown (1998).

Ogawa, 2007). In this section, an overview is given of hopping and running robots, which are categorized into two groups: spring leg runners and running humanoids.

1.3.1 Spring leg runners

Inspired by Raibert's work in the 80's (Raibert, 1986), many hopping and running robots have been built that consist of spring-like leg(s) attached to a torso (Ahmadi and Buehler, 2006; Andrews et al., 2011; Sato and Buehler, 2004; Zeglin and Brown, 1998), of which Figure 1.2 shows three examples. Due to the springs in the legs, these robots are able to run in a humanlike way with a long flight duration. However, it is not clear how much insight the spring leg runners give into the human running gait, as their morphology is not humanlike. The leg inertia of these robots is very low compared to humans. An extreme example of this is the Bow Leg Hopper by Zeglin and Brown (1998) that has a leg inertia around the hip which is only 1% of the torso inertia. In addition, the spring leg runners have telescopic legs, which is a big difference from the human leg morphology with rotational knee and ankle joints.

1.3.2 Running humanoids

Robots that do have a human morphology are humanoid robots (Figure 1.3). These robots have legs that resemble human legs, with knee and ankle joints and substantial leg inertia. A number of humanoid robots have achieved a running gait (Hirose and Ogawa, 2007; Kajita et al., 2005; Nagasaka et al., 2004; Tajima et al., 2009). All of these running humanoids were primarily built for walking for which they used the ZMP control method (Vukobratovic and Juricic, 1969). This control method generates joint trajectories that keep the Zero Moment Point within the support polygon. Kajita et al. (2005) have extended this control method to allow a flight phase in which there is no support polygon. Some humanoids needed hardware upgrades to allow them

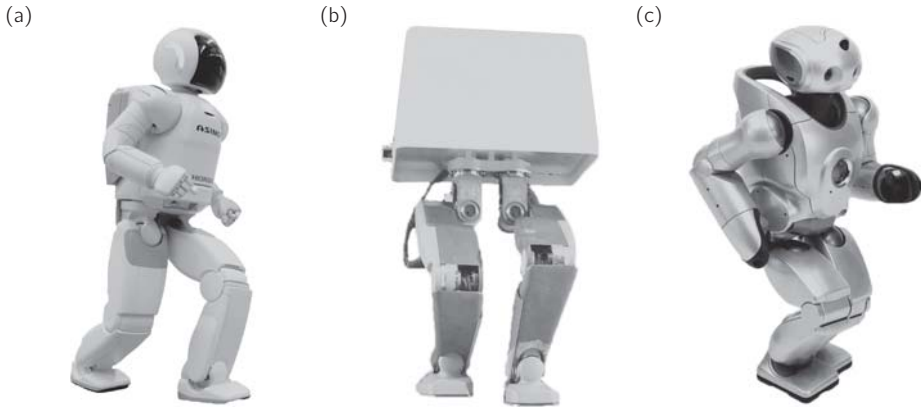


Figure 1.3: Three examples of running humanoids. (a) Asimo by Honda (Hirose and Ogawa, 2007). (b) HRP-2LR (Kajita et al., 2005). (c) Qrio by Sony (Nagasaka et al., 2004).

to run, like the addition of a toe joint to HRP-2 (Kajita et al., 2005). Although the running humanoids have a human morphology, they do not have a humanlike gait. The best performing humanoid, Asimo, has a flight duration of about 25% (Honda, 2012), whereas humans have a flight duration up to 60% (Weyand et al., 2009). The limited flight duration is caused by the lack of leg springs and the relatively high robot mass due to the autonomous nature and the versatility of these robots.

The disturbance rejection capabilities of both spring leg runners and running humanoids are not well reported. There are no quantitative results of disturbance rejection reported. And only for a couple of robots, qualitative evidence of their disturbance rejection is available. For example, the 3D biped of Raibert is shown running over a grass surface and is able to recover after a somersault (MIT Leg Laboratory, 2012; Playter, 1994). Although this shows that at least some running robots have a high disturbance rejection, it does not give much insight into the disturbance rejection behavior as it is unknown what contributed to this high disturbance rejection.

1.4 Problem statement

Although many robots have been built to research the running gait, not been paid much attention has been paid to one of the most important elements of the running gait, disturbance rejection. Handling unexpected disturbances is important, as they are common in real-life situations. Almost all running experiments are done on level

ground, so that there are no ground height disturbances. Also, the disturbance rejection performance of most of the existing running robots is not even reported.

1.5 Research goal

The goal of this thesis is to increase the understanding of the human running gait by means of gait synthesis, with a focus on the disturbance rejection behavior. The influence of the mechanical properties and the control system are investigated, as both affect the disturbance rejection behavior. To achieve this research goal, the following questions are addressed:

1. How is the disturbance rejection behavior affected by the following mechanical properties:
 - (a) the stiffness profile of the leg compliance;
 - (b) the center-of-mass location of the torso?
2. How is the disturbance rejection behavior affected by the following controller property:
 - (a) the swing-leg retraction rate?

These three properties were selected, based on our research on walking robots, where we have shown that these properties have a large effect on the walking performance (Hobbelen, 2008). In answering these questions, the focus will be on the disturbance rejection performance. However, other performance criteria, like energy efficiency, will also be taken into account, as there probably are trade-offs between the criteria.

1.6 Approach

The (sub)questions posed in the research goal are addressed independently, i.e. each property is varied while keeping all the other properties in the default setting. This way the effects of the single property variation on the performance can be singled out. Once the individual contributions of all property variations are known, the most effective property variations can be selected and combined. The default setting is chosen based on the most commonly used parameters. These parameters are, for the three investigated properties, a linear leg spring, a torso center-of-mass located at the hip, and a zero swing-leg retraction rate.

The effect of each property variation is studied using a simple simulation model, a realistic model, and a robot. The simple simulation models are the simplest models

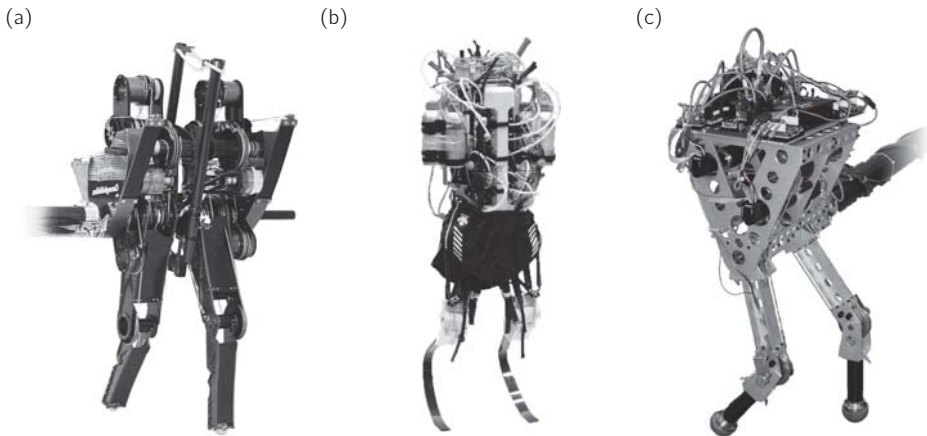


Figure 1.4: Three examples of recently built robots that have the leg compliance of the spring leg runners combined with the humanlike morphology of the humanoids. (a) Mabel by Grizzle et al. (2009). (b) Athlete Robot by Niiyama and Kuniyoshi (2009). (c) KURMET by Knox (2008).

that allow studying the desired property variation and are all modifications of the well-known spring loaded inverted pendulum (SLIP) model. These simple models are useful to get fundamental insights, due to their simple dynamics. In addition, the simple models have a short computational time, which makes them practical for operations that require a high number of runs, like optimizations. To validate the results of the simple models, a more realistic model is used. This realistic model closely resembles the physical running robot, which is used to validate the results of the simulation studies.

The robot used for this research will be a combination of the spring leg runners and the running humanoids. It will have the leg compliance of the spring leg runners combined with the humanlike morphology of the humanoids. This will make the results of this research more relevant for the human running gait. Since the start of this research, more robots have been developed based on this philosophy (Grizzle et al., 2009; Hutter et al., 2011; Knox, 2008; Niiyama and Kuniyoshi, 2009) of which three examples are shown in Figure 1.4.

This approach is partly based on the successful approach applied previously in the Delft Biorobotics Laboratory on the synthesis of the walking gait (de Boer, 2012; Hobbelen, 2008; Wisse, 2004).

1.7 Thesis outline

The remainder of this thesis consists of two parts. The first part, chapters 2 to 4, focuses on the effects of mechanical properties on the performance. The second part, chapters 5 and 6, focuses on the effects that the controller has on the performance. The content of the chapters is as follows:

Chapter 2 addresses question 1a about the effect of the leg stiffness profile on the disturbance rejection performance. In this chapter, an optimization study is presented in which the leg stiffness profile of a simple running model is optimized to maximize the disturbance rejection behavior.

Chapter 3 addresses question 1b about the effect of the center-of-mass location of the torso on the disturbance rejection performance. This effect is studied with a simulation model that consists of a torso with distributed mass attached to a massless compliant leg.

Chapter 4 discusses the running robot that was developed as part of this thesis work and that was used in the studies of Chapter 6. This running robot differs from existing running robots in that it has kneed legs instead of telescopic legs and that the leg compliance is in parallel and not in series with the actuation.

Chapters 5 and 6 address question 2a about the effect of swing-leg retraction on the performance. In Chapter 5, the effect of the swing-leg retraction rate on a simulation model with telescopic legs is discussed. In Chapter 6, the study of Chapter 5 is extended to a more realistic model and a running robot.

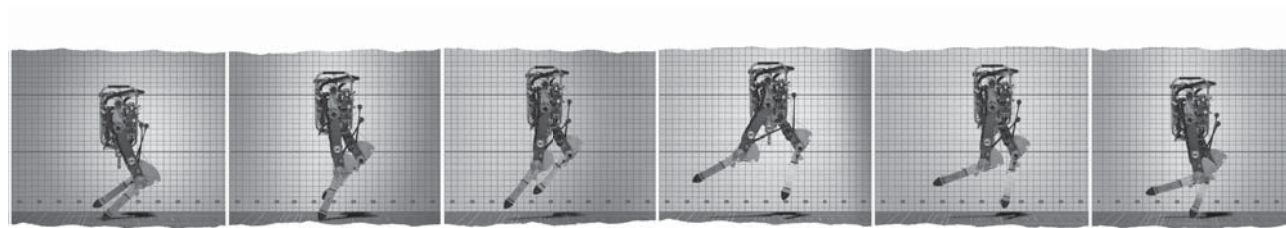
Chapter 7 presents a general discussion and conclusion of the work presented in this thesis.

Appendix A presents a study about foot placement of walking robots, which is not in line with the topic of this thesis, but was part of the work done within this PhD project.

There exists some overlap between the chapters, because Chapters 2 to 5 are written as separate papers that have been submitted or accepted for international conferences or journals. Chapter 3 is based on the MSc thesis of Tim van Ooijen.

Running with improved disturbance rejection by using nonlinear leg springs

J. G. Daniël Karssen and Martijn Wisse,
The International Journal of Robotics Research,
vol. 30, 13: pp. 1585-1595.



Abstract

Most running robots and running models use linear leg springs. Nonlinear leg springs have the potential to improve the performance of running robots and models, but it is not clear to what extent. In this chapter, the effect of nonlinear leg springs on the disturbance rejection behavior is investigated. The optimal leg stiffness profile is determined by optimizing the Gait Sensitivity Norm, a measure for disturbance rejection. The results of this optimization show that the optimal leg stiffness profile is strongly nonlinear, and that the disturbance rejection is a factor of 7 better than it would be with the optimal linear leg stiffness. The cause for this great improvement is that nonlinear leg springs allow stable limit cycles that are much further away from the fall modes.

2.1 Introduction

For bipedal running motions, leg springs are useful, because running is a gait that is characterized by large changes in potential and kinetic energy. During the stance phase, a part of the energy can be stored in spring-like elements in the leg. These spring-like elements can help in reducing the cost of transport (Alexander, 1988; Cavagna et al., 1977) and can reduce the damaging impact forces during touchdown (Liu and Nigg, 2000). Human running can effectively be modeled with a simple spring-mass model, which has a spring as leg and a point mass as body (Blickhan, 1989; McMahon and Cheng, 1990). The same model has also been used to design running robots with spring-like leg behavior. For some robots, this behavior is the result of having actual mechanical leg springs (Ahmadi and Buehler, 2006; Hurst and Rizzi, 2008; Owaki et al., 2009; Raibert, 1986; Zeglin and Brown, 1998). Others use actuators and control schemes to mimic spring-like leg behavior (Chevallereau et al., 2005). However, almost all of the research (both for human running and for robot running) is done with linear springs, presumably for ease of modeling, without considering the limitations of this simplifying assumption. Only two studies have looked at the effect of nonlinear leg springs. Rummel and Seyfarth (2008) investigated the effect of the nonlinearity introduced by the use of a two-segment leg with a linear torsion spring in the knee joint. They found that this nonlinearity increases the speed range over which stable running is possible. Owaki and Ishiguro (2007) compared a linear and a quadratic leg spring and found that a quadratic leg spring results in a faster convergence to a limit cycle. Although both of these studies involved only a single (and somewhat randomly chosen) type of nonlinearity, the observed performance increases were of such significance that they warrant a

thorough study of all possible nonlinear springs.

The key performance criterion for such a study is the disturbance rejection behavior, currently one of the main challenges for running robots due to floor irregularities, actuator limitations, and sensor noise. One might think that energetic efficiency is also important, but in the simple point mass model all linear and nonlinear springs will lead to perfectly lossless motions. Therefore, we will not address efficiency, but thoroughly study the disturbance rejection behavior. The earlier studies investigated stability (Rummel and Seyfarth, 2008) and convergence speed (Owaki and Ishiguro, 2007), two measures that provide a partial measure for the disturbance rejection behavior. Currently, for running motions there is no complete measure, which can quantify the disturbance rejection behavior within a reasonable computation time. Fortunately, for walking motions such a measure (the Gait Sensitivity Norm by Hobbelen and Wisse (2007a)) has recently been introduced, which can be adapted and validated for running motions.

The goal of this chapter is to find how much the disturbance rejection can really be improved if the optimal nonlinear leg stiffness profile is used. We aim to provide the reader with (1) an indication of the upper bound on the disturbance rejection improvement by the use of nonlinear leg stiffness, and (2) a guide towards designing optimal leg stiffness profiles. The remainder of this chapter is organized as follows. Section 2.2 describes the simple running model with nonlinear leg springs that is used in this study. Section 2.3 describes how the disturbance rejection behavior of this model is quantified. Next, Section 2.4 describes how the disturbance rejection behavior is optimized and shows the optimal stiffness profiles. The disturbance rejection behavior of the optimal linear and nonlinear leg spring profiles is compared in Section 2.5. The differences in disturbance rejection behavior are discussed in Section 2.6 and the chapter ends with the conclusions in Section 2.7.

2.2 Nonlinear spring-mass model

For this study, we use the simple spring-mass model, which is widely used for analyzing running motions (Blickhan, 1989; Ghigliazza et al., 2005; Poulakakis and Grizzle, 2009b; Schwind and Koditschek, 1997; Seyfarth et al., 2002). The model consists of a point mass on a massless spring (see Figure 2.1). Some refer to it as the Spring Loaded Inverted Pendulum (SLIP) model, because the spring describes an inverted pendulum motion during the stance phase (Schwind and Koditschek, 1997). The low complexity of this model makes it suitable to study fundamental properties of running and it is shown that in spite of its low complexity it is a good model for human and robot running (Blickhan and Full, 1993; Full and Koditschek, 1999).

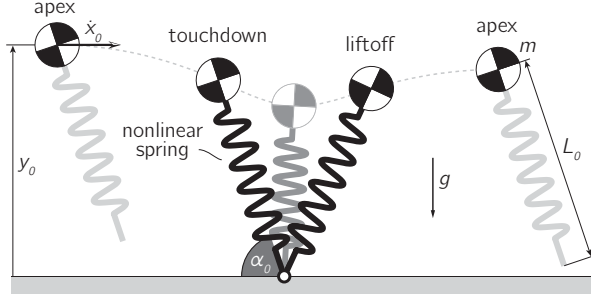


Figure 2.1: A simple running model consisting of a point mass on a massless spring. In this study, the spring can have any nonlinear stiffness profile. Besides spring properties, the model has four parameters, leg length L_0 , mass m , gravity constant g , and angle-of-attack α_0 and two initial conditions, apex height y_0 and apex velocity \dot{x}_0 .

The model has two distinct phases, a flight phase and a stance phase. During the flight phase, the point mass follows a ballistic trajectory, as the spring does not apply any force. The flight phase ends and the stance phase starts when the leg touches down with a touchdown angle, called the angle-of-attack α_0 . During the stance phase, the motion is given by:

$$m \begin{bmatrix} \ddot{x} \\ \ddot{y} \end{bmatrix} = \begin{bmatrix} -\cos \alpha \\ \sin \alpha \end{bmatrix} F_s + \begin{bmatrix} 0 \\ -mg \end{bmatrix}, \quad (2.1)$$

where α is the angle that the leg makes with the ground and F_s is the spring force. The stance phase ends, at liftoff, when the spring leg is at its rest length L_0 .

For this study, we use a constant angle-of-attack controller, which results in the same angle-of-attack for every step. The used angle-of-attack in this controller is a free parameter in the optimization.

The spring force F_s can be a linear or nonlinear function of the leg compression ΔL ,

$$F_s = f(\Delta L), \quad \text{with } \Delta L = L_0 - L. \quad (2.2)$$

The parameterization of the stiffness profile f is described in Section 2.4.1. Besides the parameters for the stiffness profile, the model has four parameters: leg length L_0 , mass m , gravity constant g , and angle-of-attack α_0 . By means of normalization ($L_0 = 1\text{m}$, $m = 1\text{kg}$, $g = 1\text{m/s}^2$), the number of free parameters is reduced by three, leaving only the spring profile and the angle-of-attack as free parameters.

We define the start of a step as the apex point during the flight phase. At the apex point the vertical velocity is zero and the state of the model is described by two initial

conditions, apex height y_0 and horizontal velocity \dot{x}_0 . We map the initial conditions of a step onto the initial conditions of the next step with the stride function S .

$$\mathbf{v}_{n+1} = S(\mathbf{v}_n), \quad \text{with } \mathbf{v} = \begin{bmatrix} y_0 \\ \dot{x}_0 \end{bmatrix}. \quad (2.3)$$

The stride function can have zero, one, or more fixed points, i.e. motions where the initial conditions result in the same initial conditions after a single step,

$$\mathbf{v}^* = S(\mathbf{v}^*). \quad (2.4)$$

If the model is started in a fixed point, it will keep on repeating the same motion. This motion is called a limit cycle and in the next section, we discuss how disturbance response of a limit cycle can be quantified.

The model has two fall modes, namely a fall backwards and a trip. For a certain range of initial conditions, the behavior (i.e. falling backwards, tripping, or not falling) is determined by the stiffness profile of the leg spring, the key effect to be studied in this chapter. However, beyond certain limits, a fall is sure to occur, no matter the stiffness profile. A trip surely occurs when the foot is below the ground at the apex point, which is given by:

$$y_0 < L_0 \sin \alpha_0. \quad (2.5)$$

A fall backwards is sure to occur when the initial conditions result in a velocity vector at touchdown that points behind the foot. This limit on the initial conditions is given by:

$$\begin{aligned} \tan \alpha_0 &< \frac{\dot{y}_{td}}{\dot{x}_{td}}, \\ \text{with } \dot{y}_{td} &= \sqrt{2g(y_0 - L_0 \sin \alpha_0)}, \\ \dot{x}_{td} &= \dot{x}_0. \end{aligned} \quad (2.6)$$

These two limits will be discussed and illustrated further in Section 2.6.1 and Figure 2.11.

2.3 Disturbance rejection measures

In this study, we aim to optimize the disturbance rejection of the running model by adjusting the leg stiffness profile. This optimization requires a measure that quantifies the disturbance rejection. A variety of such measures is available, which we describe in Sections 2.3.1 to 2.3.4. Unfortunately, all of these measures are

either too unrealistic or too computationally intensive for the optimization procedure. Therefore, in Section 2.3.5 we extensively describe the Gait Sensitivity Norm, a measure that is both fast computable and that is a good approximation of the real disturbance behavior, but which has not previously been used for running models. Finally in Section 2.3.6 we summarize how the various measures are used in the remainder of the chapter.

2.3.1 Largest allowable disturbance

The largest deterministic disturbance that a model can handle without falling is often used as disturbance rejection measure (McGeer, 1990b; Pratt et al., 2001; Wisse et al., 2005b). This measure quantifies the maximal disturbance a model can handle, but does not take into account the convergence rate after a disturbance. In this chapter, we determine the largest allowable disturbance, for a floor height and push disturbance. These disturbances are implemented as a change in the initial conditions, which for the floor height disturbance e_{floor} is,

$$y_0 = y_0^* + e_{floor}, \quad (2.7)$$

$$\dot{x}_0 = \dot{x}_0^*, \quad (2.8)$$

and for the push disturbance e_{push} ,

$$y_0 = y_0^*, \quad (2.9)$$

$$\dot{x}_0 = \dot{x}_0^* + e_{push}, \quad (2.10)$$

in which y_0^* and \dot{x}_0^* are the initial conditions for the limit cycle. Determining the largest allowable disturbance is computationally intensive, because it involves simulating many steps.

2.3.2 Largest allowable random disturbances

A better, but more computationally intensive, method to determine the disturbance rejection behavior is to disturb the model with multiple disturbances in succession instead of a single disturbance. With multiple disturbances in succession, the maximal disturbance capability and the convergence rate are both taken into account. There are many ways to define a multi disturbances measure. In this chapter, we use maximal floor height variation as defined by Hobbelen and Wisse (2007a). They quantified the disturbance rejection as the maximal variance of a Gaussian white noise sequence that, when applied as successive floor height disturbances, causes the model to fall exactly four times in an 80-step trial. In this 80-step trial, the model is restarted in its fixed point after a fall. This disturbance rejection measure

is noisy, due to the random disturbances it uses to test the disturbance rejection. To decrease the noise, the maximal floor height variation is calculated 10 times and averaged. The maximal floor height variation is even more computationally intensive than the largest allowable disturbance, as it involves the simulation of many 80-step trials. For our running model, it takes in the order of ten minutes to calculate the maximal floor height variation for a single parameter set.

2.3.3 Basin of attraction

The total set of initial conditions that result in a steady running motion is called the basin of attraction. The shape and size of the basin of attraction indicates how sensitive the model is for initial condition changes (van der Linde, 2001; Schwab and Wisse, 2001). The basin of attraction can have a highly irregular shape, making it computationally intensive to determine the exact shape, as for each possible initial condition a trail of many steps has to be run.

2.3.4 Floquet multipliers

The stability of the linearized step-to-step behavior is also used as indicator of the disturbance rejection behavior (Hürmüzlü and Moskowitz, 1986; McGeer, 1990b; Strogatz, 1994). This stability is expressed in terms of Floquet multipliers, which are the eigenvalues of the linearized step-to-step map A . This map A is found by linearizing the stride function S (equation 2.3) around the fixed point \mathbf{v}^* ,

$$\Delta \mathbf{v}_{n+1} = A \Delta \mathbf{v}_n, \quad \text{with } \Delta \mathbf{v}_n = \mathbf{v}_n - \mathbf{v}^*. \quad (2.11)$$

The Floquet multipliers indicate how fast small deviations from the limit cycle converge back to the limit cycle. A system is stable if the magnitude of all the Floquet multipliers is smaller than one. Our running model has two Floquet multipliers as it has two initial condition variables. One of these Floquet multipliers is one, due to the conservative nature of the model. An advantage of Floquet multipliers is that they require little computation time as it uses a linearized step-to-step function. A disadvantage is that Floquet multipliers are not a good predictor of how well the model can handle large disturbances (Hobbelen and Wisse, 2007a; Schwab and Wisse, 2001).

2.3.5 Gait Sensitivity Norm

Recently, Hobbelen and Wisse (2007a) introduced the Gait Sensitivity Norm, a new disturbance rejection measure. They showed that this measure is a good measure for the disturbance rejection performance of walking models as well as walking prototypes in the presence of real-world disturbances. The Gait Sensitivity Norm is also fast computable, as it uses a linearized step-to-step function, which makes it useful for

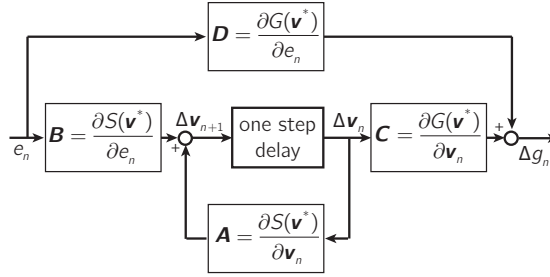


Figure 2.2: Block diagram of the step-to-step discrete system that describes the relation between an input disturbance e and an output gait indicator Δg . The internal states of this system are the initial conditions to a step $\Delta \mathbf{v}$. The sensitivity matrices \mathbf{A} , \mathbf{B} , \mathbf{C} , and \mathbf{D} are the derivatives of the stride function S and the gait indicator function G to the initial condition \mathbf{v}_n and the input disturbance e respectively. Adapted from Hobbelen and Wisse (2007a).

optimization. In this section, we will first give a short introduction of the Gait Sensitivity Norm and then discuss the implementation and validation of this measure for our running model.

The Gait Sensitivity Norm uses a gait indicator to predict the disturbance rejection performance. The gait indicator should quantify how likely the model is to fall. Examples of gait indicators are step time, step length and kinetic energy. The Gait Sensitivity Norm $\|\frac{\partial g}{\partial e}\|_2$ is defined as the H_2 -norm of the gait indicator g in the steps after a disturbance e :

$$\left\| \frac{\partial g}{\partial e} \right\|_2 = \frac{1}{e} \sqrt{\sum_{n=0}^{\infty} (g_n - g^*)^2}, \quad (2.12)$$

in which g^* is the gait indicator in an unperturbed step and g_n is the gait indicator in the n -th step after the disturbance. For model simulation studies, it is not necessary to simulate many steps, as the Gait Sensitivity Norm can be calculated from the linearized response of the stride function:

$$\left\| \frac{\partial g}{\partial e} \right\|_2 = \sqrt{\text{trace}(\mathbf{D}^T \mathbf{D}) + \sum_{n=0}^{\infty} \text{trace}(\mathbf{B}^T (\mathbf{A}^T)^n \mathbf{C}^T \mathbf{C} \mathbf{A}^n \mathbf{B})}, \quad (2.13)$$

in which \mathbf{A} , \mathbf{B} , \mathbf{C} , and \mathbf{D} are the sensitivity matrices, which describe the sensitivity of the initial condition \mathbf{v}_{n+1} and the gait indicator g_n to changes in the previous initial condition \mathbf{v}_n and to the disturbance e_n respectively (Figure 2.2).

The choice of disturbance e and gait indicator g is vital to get a good estimation of the disturbance rejection behavior. It has been shown that floor height variations as

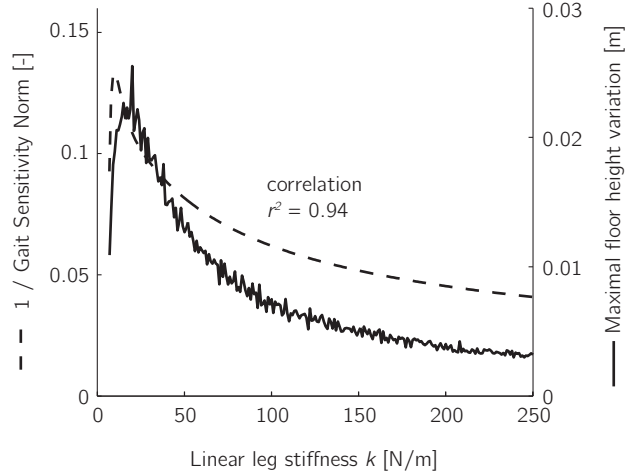


Figure 2.3: Comparison between the Gait Sensitivity Norm and the maximal floor height variation for increasing linear leg stiffness k . The model has no stable fixed points below a stiffness of 6.5 [N/m]. The used angle-of-attack α_0 is a function of the stiffness k , $\alpha_0 = \arcsin(1 - \frac{1.8}{k})$. The Gait Sensitivity Norm is highly correlated with a realistic disturbance measure, the maximal floor height variation ($r^2 = 0.94$), making it a good optimization criterion.

disturbance and step time as gait indicator work well for 2D walking models (Hobbelen and Wisse, 2007a). For our running model, we also use step time as gait indicator, but we do not use floor height variations as a disturbance, because the running model is an idealized, energy-conserving model. A floor height variation will result in a lasting change of the systems energy, as the system has no way of dissipating energy. The lasting energy change results in a lasting change of the step time and this results in an infinite Gait Sensitivity Norm. To prevent this, we implement the disturbance as a height variation e_{dis} where the horizontal velocity \dot{x}_0 is adjusted to keep the systems energy E constant:

$$y_0 = y_0^* + e_{dis}, \quad (2.14)$$

$$\dot{x}_0 = \sqrt{2(E - y_0^* - e_{dis})}. \quad (2.15)$$

We have to validate The Gait Sensitivity Norm for our running model, because it is only validated for walking models and prototypes. To validate it, we compare the Gait Sensitivity Norm with the maximal floor height variation, over a stiffness range. We do this for both the model with a linear and the model with a nonlinear leg spring. The angle-of-attack is varied with the leg stiffness, so that the comparison can be made over a large range of leg stiffness. For this, we use the relation between

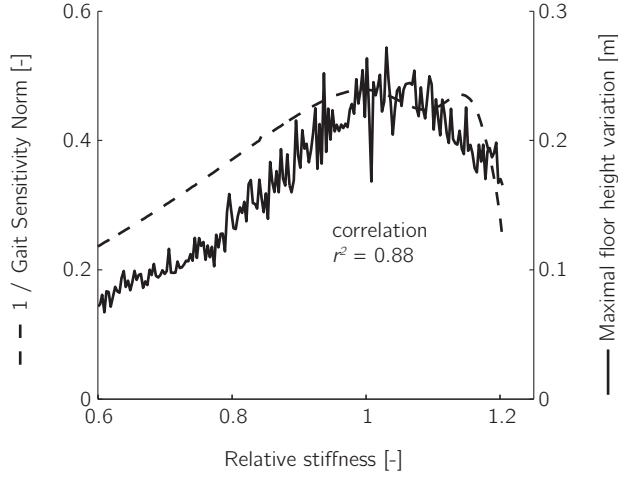


Figure 2.4: Comparison between the Gait Sensitivity Norm and the maximal floor height variation for increasing relative stiffness k_r of the optimal nonlinear stiffness profile (Figure 2.7b). The used angle-of-attack α_0 is a function of the relative stiffness k_r , $\alpha_0 = \arcsin\left(1 - \frac{0.0011}{k_r}\right)$. The Gait Sensitivity Norm is, also for the nonlinear spring, highly correlated with the maximal floor height variation.

the angle-of-attack and the leg stiffness as found by Seyfarth et al. (2002) and depicted in figure 2.13. Figures 2.3 and 2.4 show the comparison between the Gait Sensitivity Norm and floor height variation measure. Note that the reciprocal of the Gait Sensitivity Norm is plotted so that for both measures applies that the higher the value, the better the disturbance rejection. For the comparison, the absolute values are not important, as long as the two measures have a similar trend. The similarity of the trends is quantified with the correlation coefficient r^2 . There is a high correlation between the Gait Sensitivity Norm and maximal floor height variation, with $r^2 = 0.94$ for the linear spring and $r^2 = 0.88$ for the nonlinear spring. This shows that the Gait Sensitivity Norm is a good predictor of the disturbance rejection behavior for our model.

2.3.6 Selected measures

The maximal floor height variation is the most realistic of all the previously discussed disturbance rejection measures, as it takes into account the maximal disturbance and the convergence rate of the full nonlinear system. Unfortunately, the maximal floor height variation is unsuitable as optimization criterion as it is computationally too intensive for an optimization with many free parameters. However, the maximal

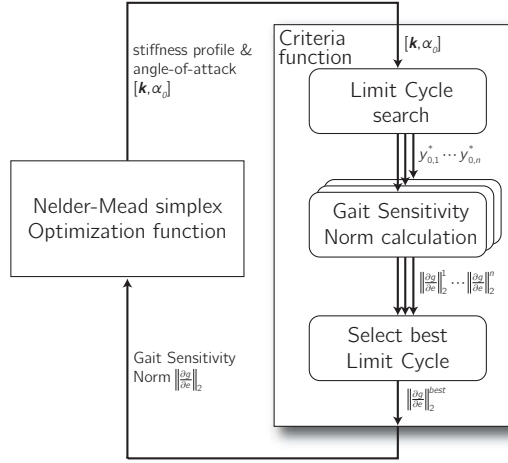


Figure 2.5: Diagram of the optimization procedure. The optimization function adjusts the parameter set (spring properties and angle-of-attack) to minimize the criteria function. This criteria function determines, for a given parameter set, all fixed points and corresponding Gait Sensitivity Norms and returns the lowest Gait Sensitivity Norm.

floor height variation can be approximated by the fast computable Gait Sensitivity Norm. In this study, we first optimize using the Gait Sensitivity Norm as optimization criterion, followed by a second optimization with a reduced number of free parameters with the maximal floor height variation as optimization criterion. The details of this optimization procedure are described in the next section.

2.4 Optimization

We optimize the disturbance rejection by adjusting the stiffness profile of the leg spring. In this section, we describe the optimization procedure (Section 2.4.1) and the results of two optimization studies. In the first study (Section 2.4.2), the disturbance rejection is optimized for a model with a nonlinear stiffness profile and in the second study (Section 2.4.3) for a model with a linear stiffness profile.

2.4.1 Optimization procedure

The optimization procedure, used in this study, is inspired by the optimization procedure used by Mombaur et al. (2005). Figure 2.5 schematically shows the optimization procedure. The optimization function optimizes the criteria function by adjusting the stiffness profile and the angle-of-attack. The criteria function searches, for a given

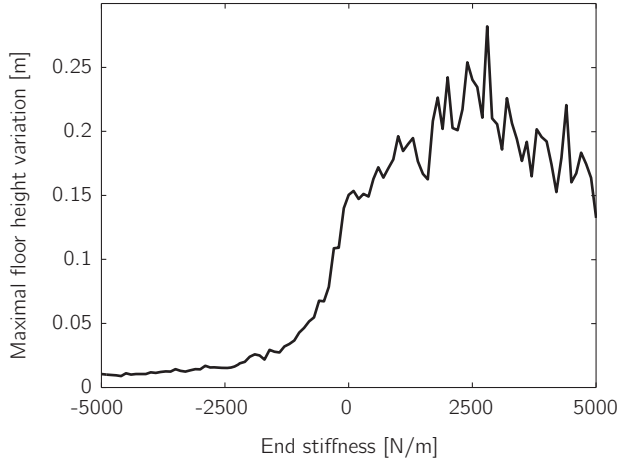


Figure 2.6: The maximal floor height variation as function of the end stiffness of the nonlinear profile. The end stiffness is the slope of the stiffness profile beyond the maximal compression during a nominal step (see Figure 2.7b).

stiffness profile and angle-of-attack, the limit cycles of the model. This search is done by Newton-Raphson searches starting from multiple starting points to find all the limit cycles. For most parameter combinations, the model has two limit cycles. Next, the criteria function determines for each of the limit cycles the Gait Sensitivity Norm and returns the lowest Gait Sensitivity Norm to the optimization function.

As optimization function, we use the Nelder-Mead simplex method. This direct search method does not use gradients. The method can handle discontinuities and not-a-number outputs of the criteria function. This makes the method suitable for our optimization problem, as the criteria function returns not-a-number for parameter sets that do not have limit cycles.

In the optimization, the system's energy is kept constant to prevent high-energy solutions, where gaits can have step lengths of many times the leg length. The constant energy level also makes the search for limit cycles easier as the number of initial condition variables is reduced to one. For this optimization study, we use an energy level of 2 J, which corresponds, when scaled to human proportions and the earth's gravitational field, to a human running at 4 m/s. In Section 2.6.4, we discuss the effect of the energy level on the optimization results.

The stiffness profile is parameterized with a cubic spline. The cubic spline gives a smooth profile that can be well integrated in the simulation. The cubic spline is built up using N knots. The knots are evenly distributed over the active region of the

stiffness profile, in which the active region starts at zero compression to the maximal compression that occurs during the limit cycle. The knots are redistributed after a number of optimization cycles, because the active region can change during the optimization. The stiffness profile beyond the maximal compression has no influence on the motion of the model during the limit cycle or on the Gait Sensitivity Norm and therefore this region does not need to be modeled. In Section 2.4.2 it is discussed how the stiffness profile beyond the maximal compression is defined. As the active region can change during the optimization, the knots have to be redistributed after a number of optimization cycles. Besides the N knot values, the slope of the start and end knot need to be specified. This results in a total of $(N+2)$ parameters to parameterize the stiffness profile. During the optimization, the number of knots is increased from 5 at the start to 10 at the end. This is done to have fast convergence in the beginning and enough freedom for the profile in the end. The optimization procedure is started at multiple starting points, in order to find the global minimum.

2.4.2 Optimal nonlinear stiffness

The Gait Sensitivity Norm is used as the optimization criterion to optimize the active part of the stiffness profile, from zero compression to the maximal compression during the limit cycle. Although the part of the stiffness profile beyond the maximal compression does not have any effect on the Gait Sensitivity Norm, and therefore has not been optimized, this part of the profile does have an effect on more realistic disturbance rejection measures, like the maximal floor height variation or the maximal step-down. To optimize the profile beyond the maximal compression, we extend the profile with a linear stiffness and optimize this stiffness using the maximal floor height variation as the criterion. We use a linear stiffness, because the computational intensity of the floor height variation measure does not allow for an optimization with more parameters. Figure 2.6 shows the maximal floor height variation as function of the stiffness of the nonlinear profile beyond the maximal compression. The maximal floor height variation is low for negative stiffness and high for positive stiffness. The optimal stiffness is about 2500 N/m and this is what we use for the remainder of the study.

Figure 2.7b shows the optimal nonlinear stiffness profile. The profile is highly nonlinear and it even has a part with a negative slope. The stiffness of the nonlinear profile is high and this results in a maximal leg compression of only 2.5% of the rest length. The angle-of-attack for this nonlinear profile is large; the leg is almost perpendicular to the floor at touchdown.

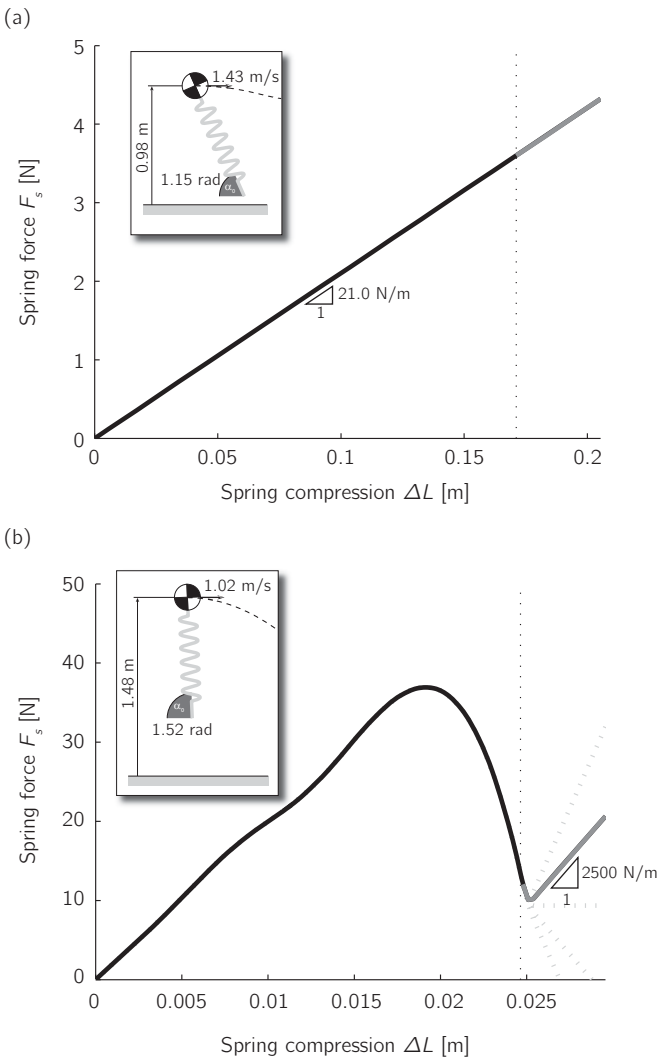


Figure 2.7: The linear (a) and nonlinear (b) stiffness profile for optimal disturbance rejection. The vertical dashed lines indicate the maximal compression during a nominal step. The inserted figures show the angle-of-attack and initial conditions of limit cycles for both the profiles. Note the difference in the overall stiffness between the optimal linear (a) and nonlinear (b) stiffness profile. The overall stiffness of optimal nonlinear is about two orders of magnitude higher than the optimal linear stiffness.

2.4.3 Optimal linear stiffness

For the linear stiffness profile, we first optimize using the Gait Sensitivity Norm as optimization criterion and after this optimization, we do a second optimization step using the floor height variation measure as optimization criterion. We do the second optimization step, because in spite of the high correlation between the two measures, they do not have the optimum at the same spot (see also Figure 2.3). In addition, the optimization of the linear spring can use the computable intensive floor height variation measure, because there are only two free parameters, stiffness and angle-of-attack.

Figure 2.7a shows the optimal linear profile and angle-of-attack and the corresponding initial conditions. The optimal linear stiffness of 21 N/m is very low compared to the optimal nonlinear profile. It is two orders of magnitude lower than the overall stiffness of the optimal nonlinear profile. This large difference in stiffness is related to the difference in angle-of-attack for the linear and nonlinear stiffness profiles, as there is a strong correlation between angle-of-attack and stiffness (Seyfarth et al., 2002). The cause of these differences between the optimal profiles is discussed in Section 2.6.1.

2.5 Disturbance rejection of optimal linear and nonlinear stiffness profiles

In Figure 2.8 the disturbance rejection behavior of the optimal linear spring is compared with the optimal nonlinear spring using five realistic disturbance measures: maximal floor height variation, step-down, step-up, push forward and push-backward. The measures are implemented as discussed in Section 2.3. All five measures show that the optimal nonlinear leg has a much better disturbance rejection behavior than the optimal linear leg. The model with the optimal nonlinear spring can handle floor height variations with a variance of 19% of the leg length, which is a factor 7 higher than the 2.7% with the optimal linear leg spring. Figure 2.9 shows the trajectories of the model running on a floor with height variations. The difference in disturbance rejection is even larger for the maximal step-up. The maximal step-up is 0.485 m for the optimal nonlinear spring versus 0.019 m for the optimal linear spring. This great difference is caused by the difference in apex height. At the apex point, the model with the linear spring is already close to the ground, making it sensitive for step-up disturbances. In Section 2.6.1, we discuss the cause of this difference in apex height.

The difference in disturbance rejection can also be seen in the basin of attraction (Figure 2.10). The basin of attraction for the nonlinear leg spring is much larger than

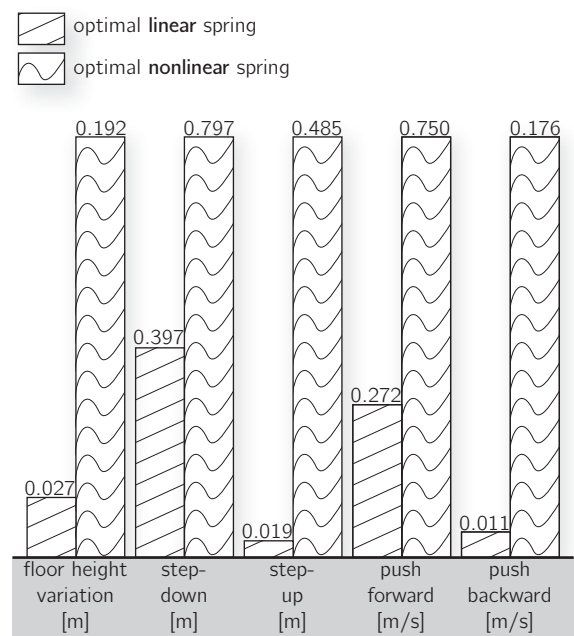


Figure 2.8: Comparison of the disturbance rejection behavior between the optimal linear and nonlinear leg spring. All measures show that the disturbances rejection with the nonlinear spring is much better than with the linear spring.

for the linear leg spring, indicating that the model with the nonlinear leg spring can handle larger initial condition variations. Both basins of attraction have an irregular fractal edge, which is common for simple legged systems (van der Linde, 2001; Sato and Buehler, 2004; Schwab and Wisse, 2001). Note that the maximal step and push disturbance are equal to the distance between the limit cycle and the edge of the basin of attraction in the vertical and horizontal direction respectively.

2.6 Discussion

2.6.1 Explanation of the improved disturbance rejection

We showed that the model with the optimal nonlinear leg spring has a much better disturbance rejection behavior compared to the optimal linear leg spring. To explain this difference in disturbance rejection behavior we have to look at what determines the disturbance rejection behavior. The disturbance rejection is determined by the combination of the following three things: (1) the disturbance sensitivity, which

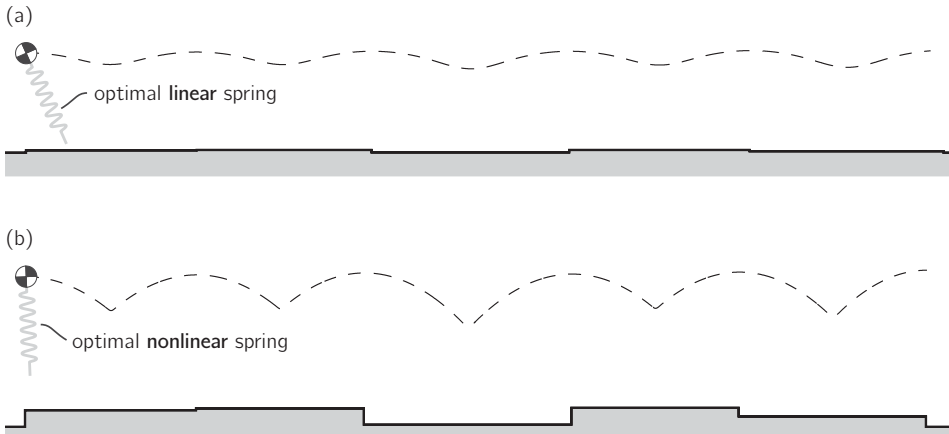


Figure 2.9: The running model with the optimal linear (a) and nonlinear (b) leg spring running on a floor with height variations. The dotted lines are the trajectories of the point mass. The shown floor height variations are about the maximum of what the model can handle without falling.

means how far the model deviates from its limit cycle as it is disturbed, (2) the rate at which the model converges back to its limit cycle after it is disturbed and (3) the maximal deviation from the limit cycle that the model can handle without falling.

The leg spring stiffness profile does not have any effect on the disturbance sensitivity (1), because the used floor height variation disturbance results in a change of the initial conditions that is independent of the limit cycle or the stiffness profile.

The convergence rate (2) can be expressed with the Floquet multipliers (Section 2.3.4). The model with a linear leg spring and a nonlinear leg spring can both have a Floquet multiplier that is very close to zero, meaning that the model almost converges back to the limit cycle within a single step.

Thus, the main difference is found in the maximal deviation (3). This maximal deviation depends on the fall modes of the model. The running model has two fall modes: falling backwards and tripping (see Section 2.2). Figure 2.11 shows fall modes as a function of the initial conditions and the angle-of-attack. Note that in the indicated fall areas, the model will fall, no matter what the leg stiffness profile is. Figure 2.11 also shows the initial conditions and angle-of-attack for both the optimal linear and nonlinear stiffness profiles. The initial condition of the nonlinear profile is as far away as possible from the two fall areas, whereas the initial condition of the linear profile is close to the tripping boundary. This explains why the model with the optimal linear leg spring is far more likely to trip.

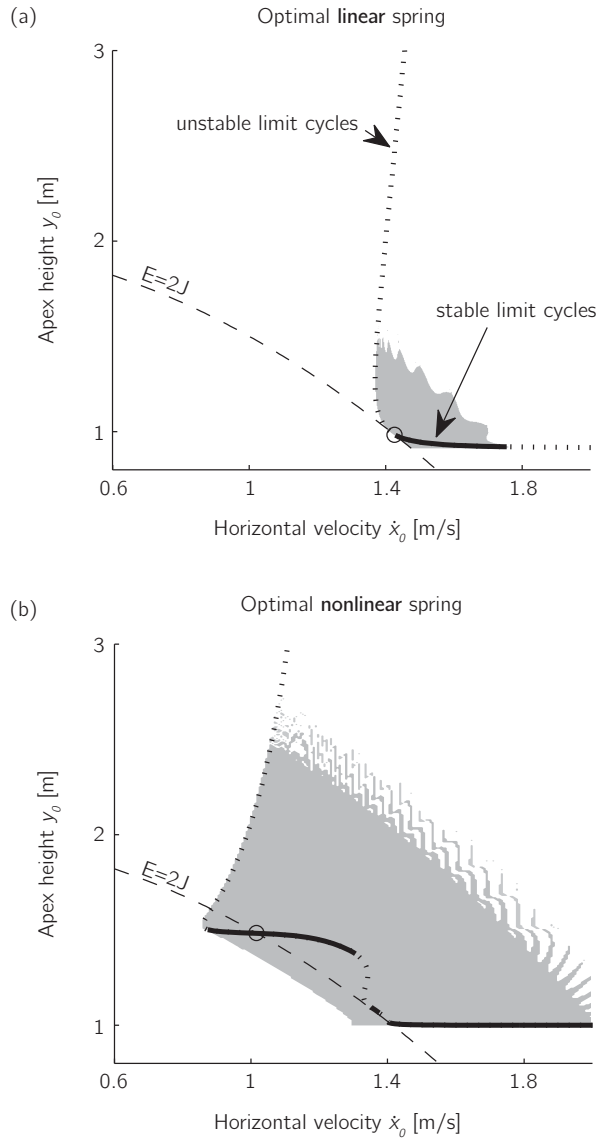


Figure 2.10: The basin of attraction for the running model with the optimal linear (a) and nonlinear (b) profile. The size of the basin of attraction of the optimal non-linear spring is much larger than of the linear spring, indicating that the optimal nonlinear spring can handle large variations in the initial conditions.

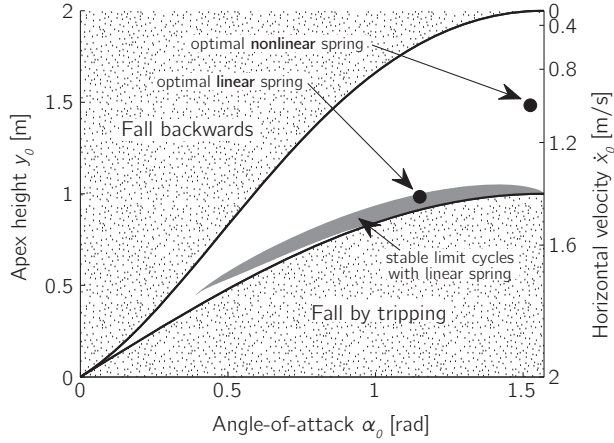


Figure 2.11: The limit cycles for initial conditions y_0 & \dot{x}_0 and angle-of-attack α_0 combinations. In two dotted areas, limit cycles are not possible as the model will fall backwards or trip, no matter what the leg stiffness profile is. The borders of these fall areas are given in equations 2.5 and 2.6. The gray area indicates the combinations of initial condition and angle-of-attack that have a stable limit cycle for a model with a linear leg stiffness.

We hypothesize that the optimal linear spring has such a low maximal deviation, because it has only one free parameter, its stiffness. With only one free parameter in the stiffness profile, the optimization can only vary two parameters, the stiffness and the angle-of-attack. However, at least three parameters are needed to get both an optimal convergence rate and an optimal maximal deviation. One parameter is needed for the optimal convergence rate, as the model has one controllable Floquet multiplier, and two parameters are needed for the optimal maximal deviation, one for each dimension in Figure 2.11. The linear spring is short one parameter, which means that there is a trade-off between the convergence rate and the maximal deviation. In this trade-off, the convergence rate should be at least such that the system is stable (magnitude of the Floquet multiplier lower than one). The grey area in Figure 2.11 indicates for which combinations of initial conditions and angle-of-attack this is the case. It shows that stable limit cycles are only possible close to the tripping boundary. This stable area also explains why the angle-of-attack for optimal linear spring is lower than for the optimal nonlinear spring. For high angle-of-attacks, like the angle-of-attack of the optimal nonlinear spring, the linear spring only has stable limit cycles very close to the tripping boundary.

To further test the hypothesis that the single free parameter of the linear profile is the cause for the difference in the disturbance rejection, we investigate the disturbance

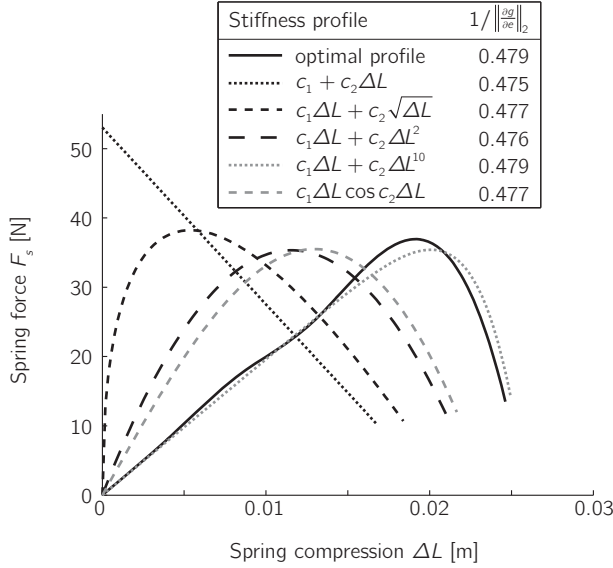


Figure 2.12: The optimal nonlinear stiffness profile and a set of two-parameter profiles that have almost the same disturbance rejection as the optimal nonlinear stiffness profile (less than 1% difference). All profiles are shown from zero compression up to the maximal compression during the limit cycle. The table shows the disturbance rejection of the profiles as the reciprocal of the Gait Sensitivity Norm $\|\frac{\partial g}{\partial e}\|_2$. Note that these profiles are examples, many more stiffness profiles exist that have a similar disturbance rejection.

rejection of stiffness profiles with two free parameters. For these two-parameter profiles, one parameter is used to optimize the convergence rate, while the other parameter is used to optimize the maximal deviation. Figure 2.12 shows examples of these optimized two-parameter profiles. We find that it is indeed possible to have an optimal convergence rate (Floquet multiplier of zero) and an optimal maximal deviation (same initial conditions and angle-of-attack as for the optimal nonlinear stiffness profile) with a two-parameter profile. Moreover, we found that the disturbance rejection, expressed in the Gait Sensitivity Norm, of all the optimized two-parameter profiles is almost equal to the disturbance rejection of the optimal nonlinear profile (see table in Figure 2.12). This means that there is not a single optimal stiffness profile, but a whole set of optimal stiffness profiles. Any nonlinear stiffness profile that has the optimal convergence rate and the optimal maximal deviation will have a disturbance rejection that is very close to the optimal disturbance rejection.

The stiffness profiles in the set of optimal stiffness profiles seem to have two common

characteristics, a high overall stiffness and a negative stiffness for part of the profile. The high overall stiffness is because the steep angle-of-attack requires a short contact time, which only happens with a high overall stiffness. The reason for the negative stiffness part of the optimal profiles is less clear. We believe that the negative stiffness part is because the optimal convergence rate requires that the spring force at maximal compression is low (about 10 N), while overall stiffness should be high. We do not have a mathematical proof for this requirement, despite an exhaustive search, but all the optimal stiffness profiles we found have this characteristic.

2.6.2 Applicability

We showed that a nonlinear stiffness profile can increase the disturbance rejection up to a factor of 7. However, we did not apply any practical constraints to the stiffness profile, as the goal of this study was to determine the upper bound on how much disturbance rejection can be improved by using nonlinear leg springs. The resulting optimal nonlinear stiffness profile has a gait that is almost like impulsive running (Srinivasan and Ruina, 2005), with a very high leg stiffness and an angle-of-attack of almost $\frac{\pi}{2}$. This gait might be hard to implement on a running robot, as it results in a very short contact time. However, the method presented in this chapter can also be used to determine nonlinear stiffness profiles that have a good disturbance rejection and that are more practically feasible. To do this, constraints should be added to the optimization. Reasonable constraints could be a maximal stiffness or a maximal angle-of-attack. We plan to conduct such a study in the near future. In addition, we are constructing a running robot, which can be outfitted with different leg stiffness profiles. We will use this robot to validate the results of this study.

2.6.3 Parameter Sensitivity

For implementation of the optimal nonlinear stiffness profile on a running robot it is important that the model is not extremely sensitive for parameter variations. Figure 2.13 shows how sensitive the model is for variations in the stiffness and angle-of-attack parameter for both the optimal linear and nonlinear springs. The relative stiffness in this figure is a scale factor of the stiffness profile. The parameter sensitivity is approximately equal for the optimal linear and nonlinear spring. With both springs, the model is sensitive for angle-of-attack variations and less so for changes in the relative stiffness. Based on these results, we can conclude that the nonlinear leg spring improves the disturbances rejection while keeping the same parameter sensitivity.

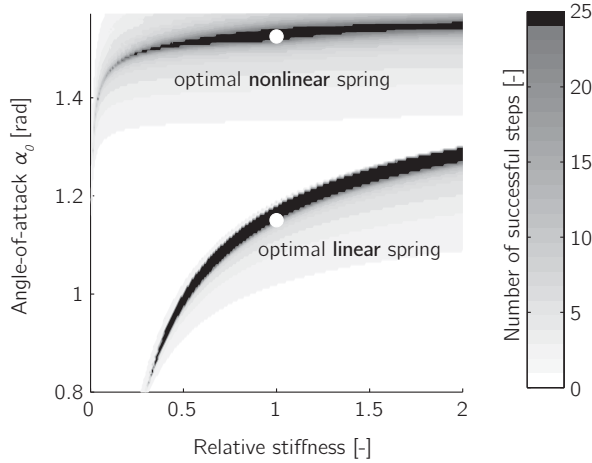


Figure 2.13: The number of steps the model runs after a parameter change. The trials were stopped after 25 steps. The white dots indicate the optimal parameter combinations.

2.6.4 Effect of the energy level

In the optimization there is only one parameter kept fixed, the energy level. To study the effect of this parameter on the results of the optimization, we conducted the same optimization with a higher energy level of 3 J. The optimal stiffness profile for this higher energy level has a similar shape as for the 2 J energy level. The maximal floor height variation, at this energy level, is 0.326 m for the optimal nonlinear spring and 0.073 m for the optimal linear spring. This shows that also for other energy levels there are large improvements possible by using nonlinear leg springs instead of linear springs.

2.6.5 Comparisons with related studies

The results of this study are in line with the results of Rummel and Seyfarth (2008). They found that softening stiffness profiles increases the disturbance rejection. Their nonlinear stiffness profiles did not have the possibility for a negative slope, which resulted in less improvement of the disturbance rejection than what we obtained in this study.

At first sight, the results might seem to be in contrast with the results of Owaki and Ishiguro (2007), as they showed improvement in stability with a stiffening profile. However, Owaki and Ishiguro (2007) looked at stability and not a disturbance rejection. This makes a large difference because it is possible to have an optimal stability

(Floquet multiplier of zero) but a very poor disturbance rejection because the limit cycle is very close to the edge of the basin of attraction.

2.7 Conclusion

In this chapter, we presented an optimization study, in which the disturbance rejection behavior of a running model was optimized by adjusting the leg spring stiffness profile. The goal of this study was to determine the optimal leg stiffness profile and to determine the upper bound on how much disturbance rejection can be improved by using nonlinear leg springs. Based on the results of this study we conclude that:

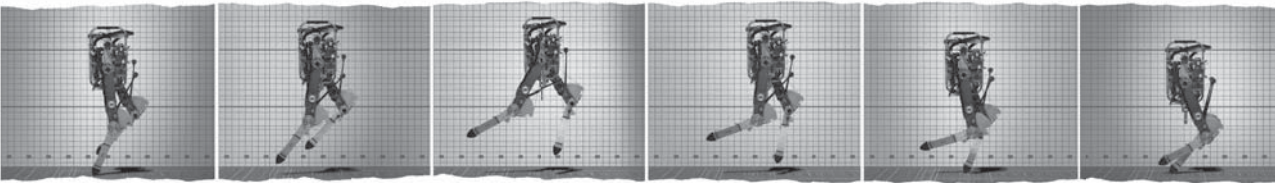
- Nonlinear leg springs can significantly improve the disturbance rejection of a running model. For an energy level of 2 J, the disturbance rejection can be improved up to a factor 7 compared to the optimal linear leg spring (Figure 2.8).
- The stiffness profile for the optimal disturbance rejection behavior is strongly nonlinear (Figure 2.7b).
- There is a whole set of nonlinear stiffness profiles that have a disturbance rejection behavior that is almost equal to the optimal disturbance rejection behavior (Figure 2.12).
- Nonlinear leg springs allow for stable limit cycles that are further away from the fall modes compared to linear leg springs (Figure 2.11).
- The Gait Sensitivity Norm is a good measure of the disturbance rejection of a running model (Figures 2.3 and 2.4).

Acknowledgements

This work was supported by the Dutch National Technology Foundation STW, applied science division of NWO. The authors would like to thank Frans van der Helm and Matt Haberland for proofreading.

The effect of center-of-mass offset on the disturbance rejection

Tim P. van Oijen, J.G.Daniël Karssen, and Martijn Wisse,
To be published in the *International Journal of Humanoid Robotics*.



Abstract

Running robots often have their center-of-mass (CoM) of the torso located on the hip, to allow for simple control schemes. However, an offset between the CoM and the hip might increase a robot's ability to recover from disturbances. In this simulation study, we investigated the effect of the CoM-location on the largest disturbance that can be corrected within one or two steps. We found that, for one-step recovery strategies, the optimal CoM-location is above the hip for a step-down disturbance and below the hip for a push disturbance. For two-step recovery strategies, we found that the performance increases for increasing offset of the CoM. An offset of the CoM-location can increase the disturbance rejection up to a factor of 10 compared to the CoM at the hip.

3.1 Introduction

Initiated by the pioneering work of Raibert (1986) during the 80's, several running and hopping robots have been built over the past years. Research into robotic running can be classified into two approaches: the control approach and the mechanical approach. Although supporters of both approaches share the same goal, which is to build dynamically stable and energy efficient running robots, their design focus is different. The control approach starts with a mechanical design and then tries to find control laws that give the system an optimal running performance. Examples of robots that have been built according to this principle are HRP (Kajita et al., 2005), Asimo (Hirose and Ogawa, 2007) and Toyota Partner Robot (Tajima et al., 2009). Although these robots look like humans, their way of locomotion is not very humanlike. As far as we can tell from the very few publications on these robots, the mechanical system and control are not designed so that the whole system benefits from natural dynamics, which is observed in human running (Cavagna et al., 1977). As a result, locomoting robots that are built following the control approach are usually characterized by a low energy efficiency (Collins et al., 2005). The mechanical approach, on the other hand, strives for an optimal mechanical system in combination with simple control rules. Examples of running robots that have been built according to this principle can be found in (Ahmadi and Buehler, 2006; Gregorio et al., 1997; Hodgins and Raibert, 1991; Hurst et al., 2007; Raibert and Brown Jr, 1984; Raibert et al., 1984; Zeglin and Brown, 1998). These robots somehow store and re-use energy throughout the running cycle, which results in a higher energy efficiency and a more natural motion.

Although they show a natural motion, the energy efficient running robots in general

do not look very humanlike. One of the reasons is that the CoM of the torso is usually placed on the hip (Ahmadi and Buehler, 2006; Gregorio et al., 1997; Hodgins and Raibert, 1991; Raibert and Brown Jr, 1984; Raibert et al., 1984; Zeglin and Brown, 1998). The reason for this choice is that it decouples the pitching dynamics and CoM-dynamics. Raibert successfully implemented three independent linear feedback controllers for the hopping height, the forward velocity, and the torso pitch (Raibert, 1986). The fact that the pitching and CoM-dynamics were decoupled in his prototypes made these simple control schemes possible. However, the question whether less intuitive control schemes and a CoM-offset may improve the performance, has not been addressed. We expect that the introduction of a coupling between the pitching and CoM-dynamics can significantly improve the running gait.

In this chapter, we present a simulation study into the effect of the CoM-location on the running performance. The performance criterion that this study focuses on is the ability to deal with external disturbances, as this is one of the most important criteria to make running robots capable to operate in the real world. The goal of the study is to find the optimal CoM-location of the torso of a running robot with hip actuation in terms of its disturbance rejection.

The remainder of the chapter is organized as follows. A general definition of disturbance rejection and a precise definition of the exploited measure for disturbance rejection are given in Section 3.2. The model is explained in detail in Section 3.3. In Section 3.4, periodic motions of the model are investigated. The method to calculate the disturbance rejection measure for each CoM-location is explained in Section 3.5 and the results of this calculation are given in Section 3.6. The chapter ends with a discussion in Section 3.7 and a conclusion in Section 3.8.

3.2 Disturbance rejection

Disturbance rejection can be regarded as the ability to deal with unexpected disturbances. Unexpected disturbances can be for example measurement errors, externally applied forces, and unexpected changes in floor height. In this study, we focus on two specific disturbances, namely a step-down and a push. These disturbances occur frequently in the real world, and are therefore useful to investigate. A step-down is defined as a negative change of the floor height and a push is defined as an instantaneous increase of the horizontal CoM-velocity. See Section 3.5 for a more detailed description of these disturbances.

In this study, we quantify the disturbance rejection with the largest n -step controllable disturbance, which is defined as the largest magnitude of a particular disturbance

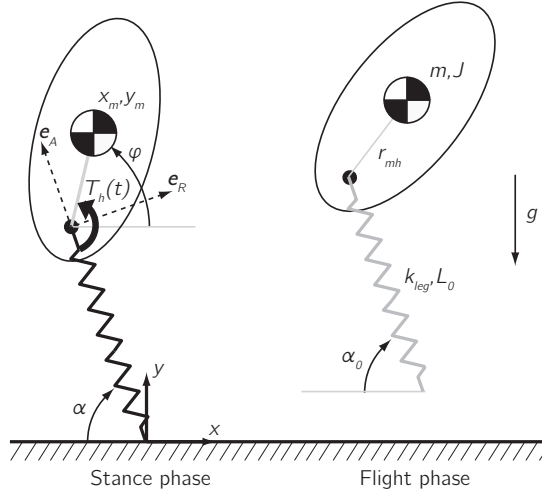


Figure 3.1: The spring-mass model with a torso and hip actuation. The running gait consists of two phases, the stance phase and the flight phase. During the stance phase, the leg behaves like a massless linear spring and a time-variant hip torque $T_h(t)$ is applied at the hip. During the flight phase, the leg is kept at a fixed angle α_0 with the ground, the torso rotates at a constant angular velocity and the CoM follows a ballistic trajectory.

from which the system can return to its nominal cycle in n steps. We selected this disturbance rejection measure as it takes into account both the maximal disturbance a system can handle and the convergence rate at which the system returns to the nominal cycle. The latter is important, because with a low convergence rate multiple small disturbances in succession can make a system fail.

In this study, the largest 1-step controllable step-down and the largest 1-step controllable push are used to evaluate different CoM-locations of a running robot. The main argument to choose for only a single recovery step is the reduced computational time that is needed to calculate the optimal actuation signals. To check whether optimal one-step recoveries are comparable to optimal multi-step recovery strategies, also the largest 2-step controllable disturbance has been calculated for a step-down and a push in Section 3.7.2.

3.3 Model

The relation between the CoM-location and the largest 1-step controllable step-down and push is investigated by means of a numerical simulation. For this, we use a modified version of the spring-mass model, also known as the SLIP model

(Blickhan, 1989; McMahon and Cheng, 1990). The spring-mass model is extended with a torso, which has an offset r_{mh} between the CoM and the hip and is actuated with a time-variant hip torque $T_h(t)$ (Figure 3.1). The model further consists of a massless spring with stiffness k_{leg} and nominal length L_0 and a rigid body with mass m and rotational inertia J . These parts are connected at the hip, which is modeled as an actuated joint. The model does not have impact losses, due to the massless leg.

3.3.1 Torque parameterization

The hip torque $T_h(t)$ is parameterized as a step function of which the torques are given by the actuation vector \mathbf{p} ,

$$T_h(t) = p_i, \text{ when } t_{i-1} < t < t_i. \quad (3.1)$$

The time instants t_0 to $t_{\#p}$ divide the stance phase in ($\#p$) parts of equal duration. We use a \mathbf{p} with 13 elements for the calculation of the largest 1-step controllable disturbance. With 13 elements, the simulation time is sufficiently low and the results do not change significantly when increasing the number of elements.

Although the hip actuation is assumed ideal, we cannot simply ignore motor limitations. Simulations show that extremely large disturbances can be corrected in a single step when torques with infinite magnitudes are allowed. In this case, results about the optimal CoM-location and actuation would not be relevant for practical applications. For this reason, we limit the absolute hip torque to T_{max} .

3.3.2 Equations of motion

The running gait of the model consists of a flight phase and a stance phase. To derive the equations of motion for the stance phase, we first define three vectors: \mathbf{r}_{CoM} , which connects the foot with the CoM, \mathbf{r}_{hCoM} , which connects the hip with the CoM and \mathbf{r}_h , which connects the foot with the hip,

$$\mathbf{r}_{CoM} = [x_m \ y_m]^T, \quad (3.2)$$

$$\mathbf{r}_{hCoM} = r_{mh}[\cos(\varphi) \ \sin(\varphi)]^T, \quad (3.3)$$

$$\mathbf{r}_h = \mathbf{r}_{CoM} - \mathbf{r}_{hCoM}, \quad (3.4)$$

in which x_m and y_m are the x and y position of the CoM with respect to the foot and φ is the absolute orientation of the torso. The angle between the leg and the horizontal is called α , which is equal to $\pi - \angle \mathbf{r}_h$ (see Figure 3.1). The hip forces \mathbf{F}_h are expressed in a coordinate system that rotates along with the stance leg. For that purpose, we define a coordinate system on the hip with the unit vectors parallel

and orthogonal to the leg, indicated by \mathbf{e}_A and \mathbf{e}_R respectively (see Figure 3.1). In the longitudinal direction (\mathbf{e}_A), the leg force $F_{h,A}$ equals the spring compression multiplied with the spring constant k_{leg} ,

$$F_{h,A} = k_{leg}(L_0 - \|\mathbf{r}_h\|). \quad (3.5)$$

In the orthogonal direction (\mathbf{e}_R), the leg force $F_{h,R}$ follows from a moment balance of the massless leg around the ground contact point,

$$F_{h,R} = T_h(t) / \|\mathbf{r}_h\|. \quad (3.6)$$

Expressing the hip forces \mathbf{F}_h in global (x, y) -coordinates requires a clockwise rotation of $\pi/2 - \alpha$ radians,

$$\begin{bmatrix} F_{h,x} \\ F_{h,y} \end{bmatrix} = \begin{bmatrix} \cos(-\pi/2 + \alpha) & -\sin(-\pi/2 + \alpha) \\ \sin(-\pi/2 + \alpha) & \cos(-\pi/2 + \alpha) \end{bmatrix} \begin{bmatrix} F_{h,R} \\ F_{h,A} \end{bmatrix}. \quad (3.7)$$

The resulting forces on the CoM of the torso \mathbf{F}_s are:

$$\mathbf{F}_s = \begin{bmatrix} F_{h,x} \\ F_{h,y} - mg \\ T_h(t) + F_{h,x} \cdot r_{hCoM,y} - F_{h,y} \cdot r_{hCoM,x} \end{bmatrix}. \quad (3.8)$$

The equations of motion for the stance phase can now be written as

$$M\ddot{\mathbf{u}} = \mathbf{F}_s, \quad (3.9)$$

where $M = \text{diag}(m, m, J)$ and $\mathbf{u} = [x_m \ y_m \ \varphi]^T$. The dynamics during the flight phase correspond to a point mass undergoing a ballistic motion and a constant angular velocity of the torso,

$$M\ddot{\mathbf{u}} = \mathbf{F}_f, \quad (3.10)$$

where $\mathbf{F}_f = [0 \ -mg \ 0]^T$. During the flight phase, the leg is kept at a constant angle α_0 . This control action does not affect the torso dynamics, due to the massless leg.

3.3.3 Events

The transition from the stance phase to the flight phase occurs when the ground reaction force becomes zero. This transition takes place when

$$T_h(t) / \|\mathbf{r}_h\| \cos(\alpha) + k_{leg}(L_0 - \|\mathbf{r}_h\|) \sin(\alpha) = 0. \quad (3.11)$$

The event that evokes the transition from the flight phase to the stance phase is a collision between the foot and the ground, which occurs when,

$$y_m - r_{mh} \sin(\phi) - L_0 \sin(\alpha_0) = 0. \quad (3.12)$$

Table 3.1: Parameter values

Parameter	Symbol	Value	Unit
Mass	m	80	[kg]
Gravitational constant	g	9.81	[m/s ²]
Nominal leg length	L_0	1.0	[m]
Leg stiffness	k_{leg}	20000	[N/m]
Angle-of-attack	α_0	68	[°]
Rotational inertia	J	6.67	[kgm ²]
CoM-offset	r_{mh}	variable	[m]
Torque limit	T_{max}	200	[Nm]
Horizontal velocity	$\dot{x}_{m,k}$	5	[m/s]

3.3.4 Parameter values

The model parameters are set to humanlike values and are given in Table 3.1. The mass m , leg length L_0 , leg stiffness k_{leg} , angle-of-attack α_0 and gravitational constant g are the same as used by Seyfarth et al. (2002, 2003). The maximum hip torque T_{max} is set to 200 Nm, which is approximately the maximal human hip torque (Anderson et al., 2007). The rotational inertia J has been set to the inertia of a homogeneous bar with mass m (80 kg) and a length of 1 meter, which is approximately the length of the human torso. The effect of the parameter values on the largest 1-step controllable disturbance is discussed in Section 3.7.1.

3.4 Limit cycle analysis

Before we can investigate the system's behavior after disturbances, we have to specify its nominal behavior. The nominal behavior can be regarded as the periodic equilibrium to which the system has to return after a disturbance. Although the equations of motion have been derived in continuous time, the system is evaluated by monitoring it only once per cycle. The subset of state space at the instant of monitoring is called the Poincaré section. For the model as described in Section 3.3, touchdown is defined as the initial state of step k . As the initial leg angle α_0 is a parameter with a fixed value, the Poincaré section that corresponds to touchdown can be fully described by only 4 variables: $\mathbf{q}_k = [\phi_k \dot{x}_{m,k} \dot{y}_{m,k} \phi_k]^T$. The step-to-step behavior of the model can be described by a mapping between \mathbf{q}_k , the initial state

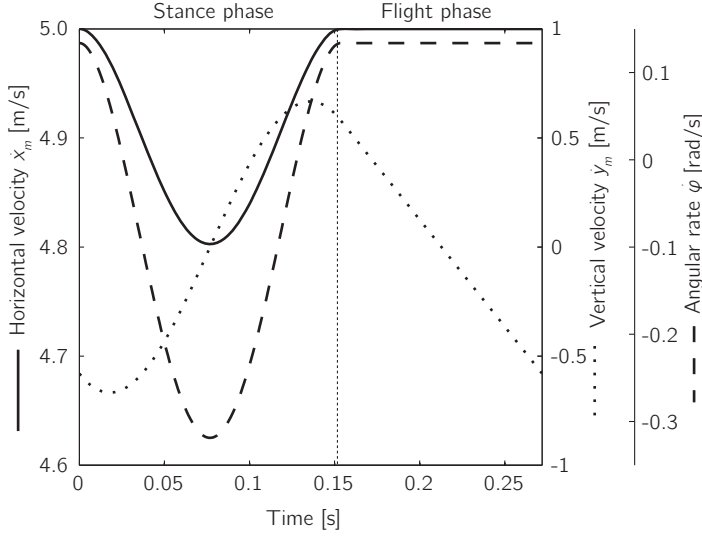


Figure 3.2: The horizontal velocity \dot{x}_m , vertical velocity \dot{y}_m and angular velocity $\dot{\phi}$ of a typical limit cycle. The CoM-offset r_{mh} is set to 0.20 m and the initial horizontal velocity $\dot{x}_{m,k}$ equals 5.0 m/s.

of step k , and \mathbf{q}_{k+1} , the initial state of step $k + 1$. This mapping is called the stride function S and is defined according to

$$\mathbf{q}_{k+1} = S(\mathbf{q}_k, \mathbf{p}). \quad (3.13)$$

An initial state \mathbf{q}_f that maps to the same state is called a fixed point: $\mathbf{q}_f = S(\mathbf{q}_f, \mathbf{p})$. The corresponding step cycle is called a limit cycle or a periodic motion.

An infinite number of limit cycles exists for the model as described in Section 3.3. In the first place, there are actuated and unactuated limit cycles. In this study, only unactuated limit cycles are investigated. This class of limit cycles comprises the most energy efficient ones, because no actuation is required (mechanical cost of transport (Hobbelen and Wisse, 2007b) equals zero). It also makes sense to analyze unactuated limit cycles for the disturbance rejection. The idea is that the less actuation is required to realize a periodic motion, the more actuation capacity is left to control the system, which is likely to increase the disturbance rejection. To further limit the number of limit cycles, we only investigate limit cycles with a horizontal velocity $\dot{x}_{m,k}$ of 5 m/s. In Section 3.7.1, we show the effect of horizontal velocity on the results. For the parameter values as listed in Table 3.1, unactuated limit cycles with the prescribed velocity exist for values of the CoM-offset r_{mh} between -0.58 m and 0.75 m. An example of such a limit cycle is given in Figure 3.2.

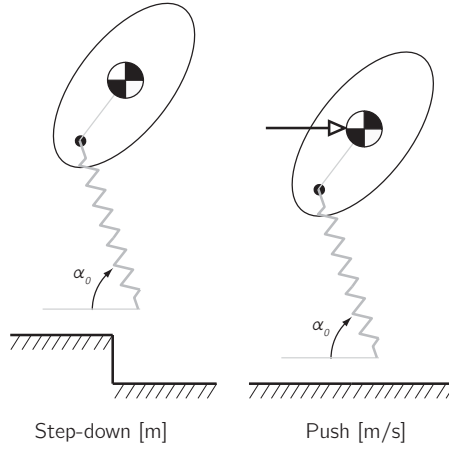


Figure 3.3: Two disturbances are investigated for the model, namely a step-down and a push on the CoM. A step-down results in an increased vertical velocity \dot{y}_k and a slightly changed torso angle φ_k at touchdown. A push results in an increased horizontal velocity \dot{x}_k at touchdown. The largest 1-step controllable step-down and push are defined as the largest magnitude from which the system can recover in a single step.

3.5 The largest 1-step controllable disturbance

In this study, the largest 1-step controllable step-down and the largest 1-step controllable push are used as a measure for the disturbance rejection. This section discusses how these largest 1-step controllable disturbances are calculated.

3.5.1 The general problem

A step-down is defined as a negative change of the floor height and a push is defined as an instantaneous increase of the horizontal CoM-velocity (see Figure 3.3). A step-down affects the vertical CoM-velocity \dot{y}_k and the torso angle φ_k at the beginning of the next step. A push only affects the initial horizontal velocity \dot{x}_k . After a disturbance, the model might be capable to return to the limit cycle in a single step by selecting appropriate values for the 13 torque parameters \mathbf{p} . The largest magnitudes of a step-down and a push for which this is possible are defined as the largest 1-step controllable step-down and the largest 1-step controllable push respectively.

Calculating the largest 1-step controllable disturbances is a difficult and computationally expensive task. In short, it comes to repeatedly increasing the magnitude of the disturbance d and searching for corrective torque parameters \mathbf{p} , until no valid corrective torque parameters can be found anymore. The task of finding torque pa-

rameters that bring the perturbed system back to its limit cycle is already a complex search task on its own. However, the hardest part is to decide whether a solution exists or not. The fundamental impossibility to distinguish between the hiddenness and the non-existence of solutions makes the process of finding the largest 1-step controllable disturbance very difficult. To reduce the complexity of calculating the largest 1-step controllable disturbance, we make two simplifications. A validation of both simplifications can be found in Section 3.7.3.

3.5.2 Simplification 1: Only torque limit

The first simplification concerns the existence of valid recovery motions. In general, an infinite number of strategies exist to recover from an infinitesimal disturbance. The fact that the actuation space (13-D) has a higher dimension than the Poincaré section (4-D) makes that there is generally a multidimensional family of actuation parameters that bring the system back to the limit cycle in a single step. This reasoning does not hold for larger disturbances. For non-infinitesimal disturbances, we can distinguish three cases.

1. A valid one-step recovery strategy exists. The required torque is less than or equal to the torque limit T_{max} .
2. Only invalid one-step recovery strategies exist. The required torque is larger than the torque limit T_{max} .
3. One-step recovery strategies do not exist.

For small disturbances, a valid one-step recovery strategy usually exists. Preliminary simulations showed that there is usually a range of larger disturbances for which invalid one-step recovery strategies exist. Only for very large disturbances, one-step recovery strategies seem to be lacking. In other words, the torque limit T_{max} has usually already been exceeded before recovery strategies start to disappear. Therefore, we simplify the problem by assuming that the torque limit T_{max} fully determines the largest 1-step controllable disturbance. Mechanisms that might be responsible for the non-existence of recovery strategies (e.g. the risk of stumbling) are not taken into account.

3.5.3 Simplification 2: Linearization

To further simplify the calculation of the largest 1-step controllable disturbance, we linearized the dynamics on the Poincaré section. In the first place, the linearization results in faster computing. Another benefit is that the largest 1-step controllable

disturbance can be calculated in a finite number of evaluations. Therefore, we do not have to worry about differences between optimization algorithms and termination criteria. Although linearization of the Poincaré dynamics may appear as an unfounded simplification, it turns out that the linearized model predicts the largest 1-step controllable disturbance remarkably accurate (see Section 3.7.3).

The linearization of the system's behavior after a disturbance d is found by differentiating the stride function (3.13) with respect to d and \mathbf{p} ,

$$\Delta \mathbf{q}_{k+1} = \frac{\partial S}{\partial \mathbf{q}_k} \frac{\partial \mathbf{q}_k}{\partial d} d + \frac{\partial S}{\partial \mathbf{p}} \mathbf{p}, \quad (3.14)$$

where $\partial S / \partial \mathbf{q}_k$ is the Jacobian of the stride function S with respect to the Poincaré variables \mathbf{q} , $\partial S / \partial \mathbf{p}$ is the Jacobian of S with respect to the actuation parameters \mathbf{p} , $\partial \mathbf{q}_k / \partial d$ is the change of the initial state with respect to the disturbance d .

The largest 1-step controllable disturbance for the linearized system is the largest disturbance d for which $\Delta \mathbf{q}_{k+1}$ can be set to zero while all the actuation parameters \mathbf{p} stay within the torque limit T_{max} . The largest disturbance d_{max} for which this holds can be determined by solving the following maximization problem,

$$\begin{aligned} d_{max} = & \\ \max_{\mathbf{p}, d} & \quad d \\ \text{s.t.} & \quad A d + B \mathbf{p} = \mathbf{0} \\ & \quad p_i \leq T_{max} \quad \text{for } i = 1 \dots N \\ & \quad p_i \geq -T_{max} \quad \text{for } i = 1 \dots N \end{aligned} \quad (3.15)$$

in which $A = \frac{\partial S}{\partial \mathbf{q}_k} \frac{\partial \mathbf{q}_k}{\partial d}$, $B = \frac{\partial S}{\partial \mathbf{p}}$ and N the number of elements in \mathbf{p} . This maximization problem is a linear programming problem, which can be solved with a simplex algorithm. The result of the maximization problem is the largest 1-step controllable disturbance d_{max} and its corresponding actuation signal \mathbf{p}_{opt} .

3.6 Results

The largest 1-step controllable step-down and the largest 1-step controllable push have been approximated for all values of the CoM-offset r_{mh} for which an unactuated limit cycle could be found. Figures 3.5 and 3.6 show the largest 1-step controllable step-down and push respectively.

The results show that the optimal CoM-offset depends on the type of disturbance. Step disturbances seem to be managed best when the CoM is about 0.3 m above the hip. The largest 1-step controllable step-down for this optimal CoM-offset is

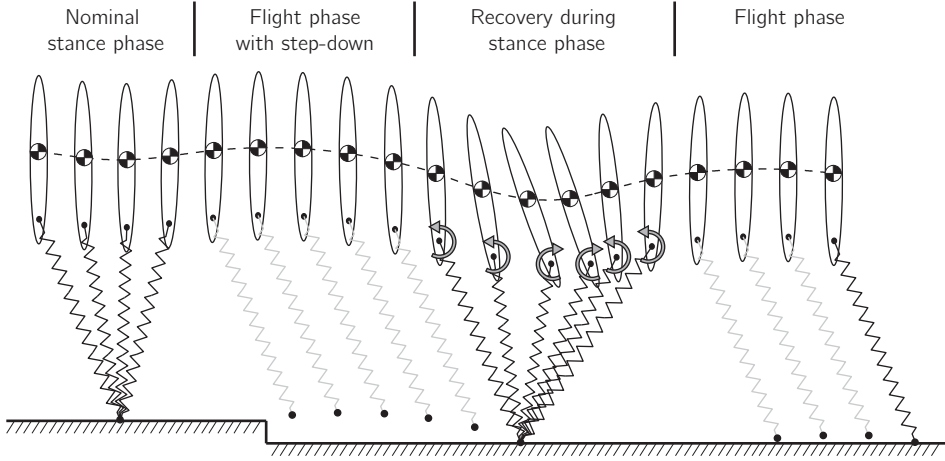


Figure 3.4: The recovery from the largest 1-step controllable step-down (0.015 m) for the optimal CoM-offset r_{mh} (0.31 m). To make the recovery motion more distinguishable from the nominal motion, the corrective motion has been scaled up as if it was a recovery from a step-down of 0.10 m. The arrow represents the torque that the hip motor applies on the body.

approximately 1.5 cm. A push on the CoM, on the other hand, can be managed best when we place the CoM about 0.5 m under the hip. The largest 1-step controllable push for this optimal CoM-offset is approximately 0.019 m/s.

Besides evaluating the optimal CoM-location, it is also interesting to investigate the worst CoM-location. In contrast with the optimal CoM-offsets, the worst CoM-offset does not depend on the type of disturbance. For a change in terrain height as well as for a push, a CoM-offset of about 0.2 m gives the system almost zero disturbance rejection.

A representation of the corresponding recovery motion is given in Figure 3.4. To recover from the step-down, the torso is successively accelerating backward, decelerating, accelerating forward, and decelerating, such that it approximately has a vertical position at the end of the stance phase. In Figures 3.5 and 3.6, the torque signals \mathbf{p}_{opt} that approximately correct the largest 1-step controllable step-down and push are given for three CoM-locations. When the CoM is located on the hip, the strategies to correct a step-down and a push are remarkably similar. This finds its origin in the decoupled pitching dynamics. In this case, all disturbances that change the energy level of the system and do not perturb the initial torso angle or angular velocity need a similar shaped control.

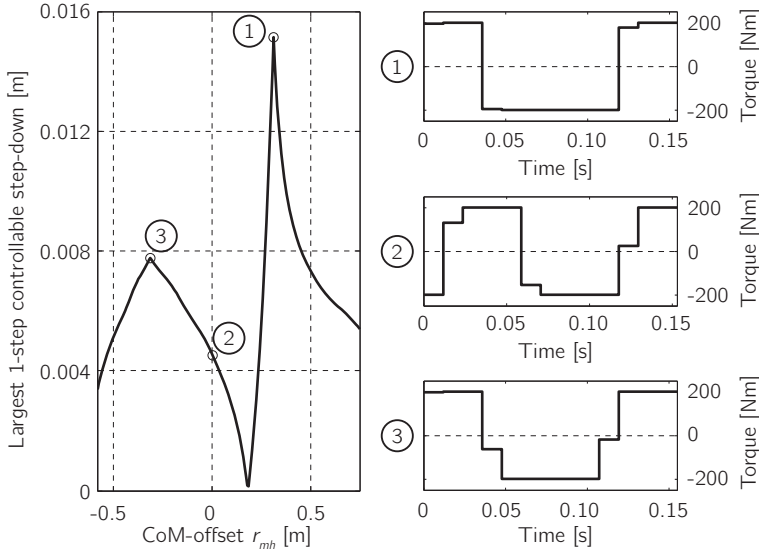


Figure 3.5: Approximation of the largest 1-step controllable step-down versus the CoM-offset r_{mh} . The recovery torque signal is shown for the optimal CoM-offset above the hip (1), the CoM on the hip (2) and the optimal CoM-offset under the hip (3).

3.7 Discussion

The figures of the largest 1-step controllable step-down and push (Figures 3.5 and 3.6) both show that a CoM-offset of 0.2 m has a disturbance rejection that approaches zero. Moreover, the largest 1-step controllable step-down shows a sharp peak at a CoM-offset of about 0.3 m. To find the origin of these characteristics, we perform a singular value decomposition (SVD) of the actuation Jacobian, $\partial S/\partial \mathbf{p} = \mathbf{U}\mathbf{Z}\mathbf{V}$. The matrix \mathbf{Z} is an empty matrix, except for the diagonal elements which are filled with the so-called singular values. The matrices \mathbf{U} and \mathbf{V} are respectively the orthonormal output basis and orthonormal input basis. The n th singular value indicates how much actuation is needed to move the system's Poincaré location in direction \mathbf{u}_n (n th column of \mathbf{U}). The smaller the singular value, the more actuation is required. Two quantities that are related to the SVD have been evaluated for every CoM-offset.

1. The smallest singular value σ_{min} .
2. The projection of the unactuated perturbed system $\mathbf{S}_d (= \frac{\partial S}{\partial \mathbf{q}} \frac{\partial \mathbf{q}_k}{\partial d})$ on the output direction \mathbf{u}_{min} (direction corresponding to σ_{min}). This projection indicates to which extent the least controllable direction is affected by the disturbance.

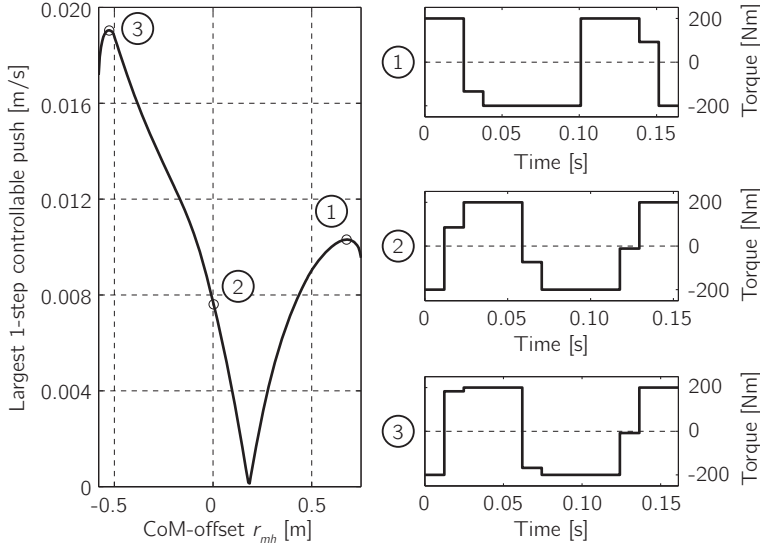


Figure 3.6: Approximation of the largest 1-step controllable push on the CoM versus the CoM-offset r_{mh} . The recovery torque signal is shown for the optimal CoM-offset above the hip (1), the CoM on the hip (2) and the optimal CoM-offset under the hip (3).

Figure 3.7 shows the two evaluated quantities for every CoM-offset. The dips in these two quantities can explain the dips and peaks in the largest controllable step-down and push. The singular value has a dip at the same CoM-offset as where the largest controllable disturbance approaches zero. This means that for this CoM-offset a large actuation torque is needed if the disturbance perturbs the state in the least controllable direction. The peak in the largest controllable step-down can be explained by the dip in the projection of the step-down disturbance on the least controllable direction. The dip indicates that for this CoM-offset a step-down disturbance hardly perturbs the state in the least controllable direction.

The singular value decomposition does not give a physical explanation for the dips and the peak. The least controllable direction does not seem to correspond to some well-defined physical quantity. To gain more insight in the physical cause of the dips and peaks, we investigate, in the next subsection, how the peaks and dips are affected by parameter variations.

3.7.1 Parameter variations

The model used in this study has 8 fixed parameters (see Table 3.1). Three of these parameters, mass, gravitational constant and leg length, can be used to nor-

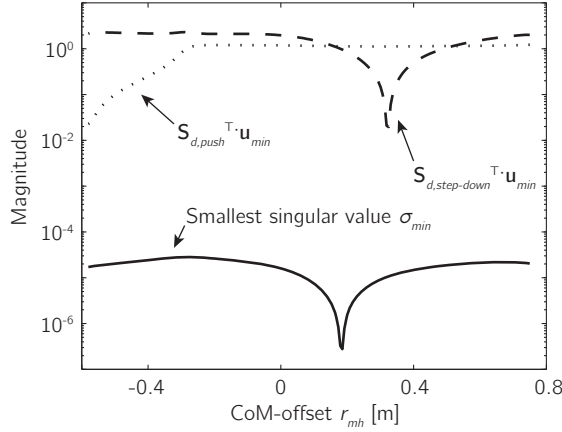


Figure 3.7: The smallest singular value of $\partial S/\partial \mathbf{p}$ (solid line) and the projection of the unactuated perturbed system \mathbf{S}_d on the least controllable output direction \mathbf{u}_{min} for a step-down disturbance (dashed line) and a push disturbance (dotted line).

malize the system and will therefore only have a trivial scaling effect on the largest controllable disturbance. In addition, the effect of the torque limit is trivial, as the largest controllable disturbance scales linear with the torque limit. This leaves four parameters to vary: rotational inertia J , leg stiffness k_{leg} , angle-of-attack α_0 and horizontal velocity $\dot{x}_{m,k}$. These parameters, besides the rotational inertia, cannot be varied independently, as only limit cycles exist for certain combinations of these parameters. We vary these parameters in pairs, setting one parameter to a desired value and adjusting the other parameter such that there is a limit cycle for the zero CoM-offset with the same initial conditions as for the default parameter settings.

Figure 3.8 shows the effect of parameter variations on the largest 1-step controllable step-down. Variations of the rotational inertia only have a small effect on the magnitude of the largest controllable step-down, but do change the location of the peak and dip in the largest controllable step-down. The horizontal velocity has a strong effect on the largest controllable step-down. A decrease of the horizontal velocity decreases the largest controllable step-down and also decreases the range of CoM-offsets for which limit cycles can be found. The effects of leg stiffness and angle-of-attack variations are less clear, because their effect seems highly dependant on the choice of the co-varying parameter.

The location of the peak in the largest controllable step-down is affected by all parameter variations. This indicates that the optimal CoM-offset is sensitive for all parameter changes. On the other hand, the location of the dip in the largest

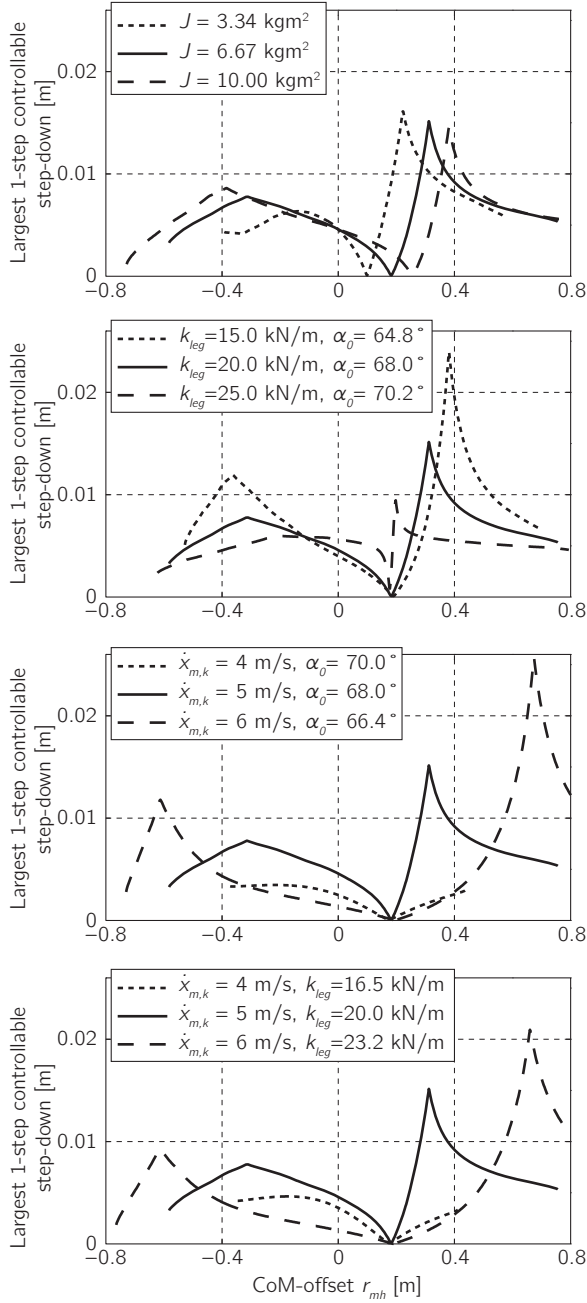


Figure 3.8: The effect of parameter variations on the relationship between the CoM-offset and largest 1-step controllable step-down.

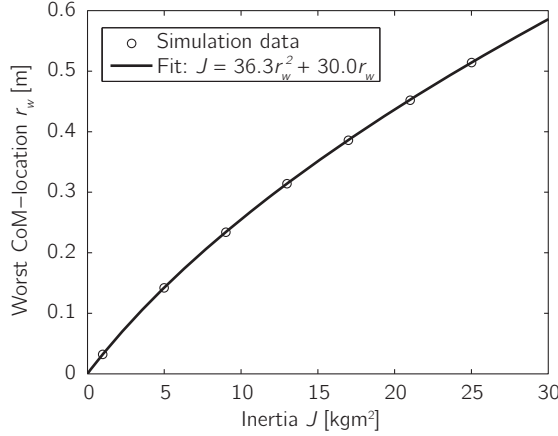


Figure 3.9: The worst CoM-location as function of the rotational inertia of the torso and a quadratic fit.

controllable disturbance is only affected by the rotational inertia of the torso. Figure 3.9 shows the CoM-offset of the dip for 7 settings of the rotational inertia. The relation between this worst CoM-offset and the rotational inertia can be approximated very well by a quadratic function,

$$J = 36.3r_w^2 + 30.0r_w, \quad (3.16)$$

in which r_w is the CoM-offset of the dip. This clear relation between the inertia and the worst CoM-offset suggests that there is a physical explanation for the dip in the largest controllable disturbance. However, we did not find a physical explanation. This is partly caused by the non-negligible coupling between the pitching dynamics and the CoM-dynamics that make the system much less intuitive than the spring-mass model.

3.7.2 Two-step strategies

So far, we focused on strategies to correct disturbances in only a single step. It turns out that a step-down smaller than 1.5 cm and a push smaller than 0.019 m/s can be corrected in this way, choosing the appropriate CoM-offset. Larger disturbances on the other hand cannot be managed in a single step. To get an idea about optimal strategies for coping with these larger disturbances, we performed a linear approximation of the largest step-down and push that can be corrected in two steps. Torque signals for two subsequent stance phases have been parameterized with 14 parameters. An adaptation of the angle-of-attack $\Delta\alpha_0$ between the first and second

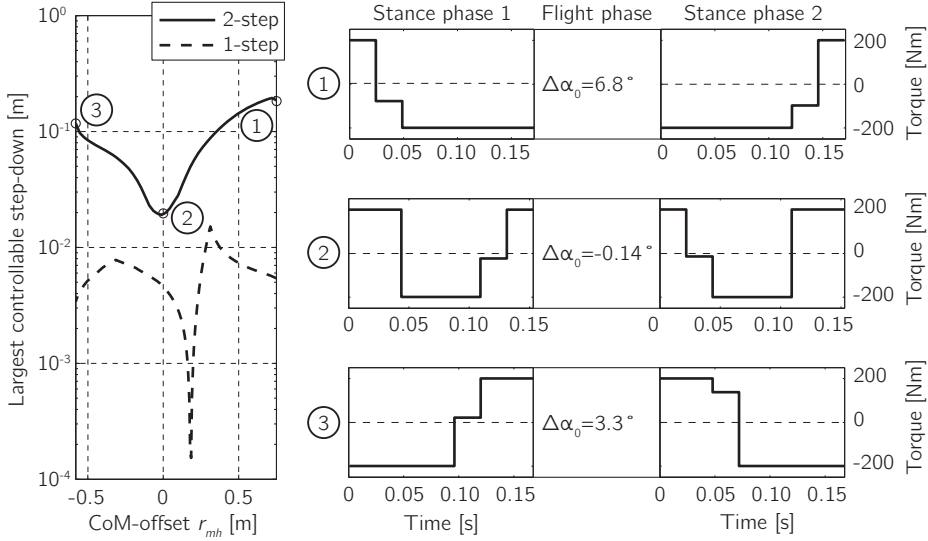


Figure 3.10: Approximation of the largest 2-step controllable step-down versus the CoM-offset r_{mh} . The largest 1-step controllable step-down is also shown for reference. The strategies to recover from the largest 2-step controllable step-down are shown for the optimal CoM-offset above the hip (1), the CoM on the hip (2) and the optimal CoM-offset under the hip (3). The recovery strategy consists of hip actuation during the first and second stance phase and a temporary adaptation of the angle-of-attack $\Delta\alpha_0$ between the first and second stance phase. Notice that placing the CoM exactly on the hip is the worst option for two-step recovering strategies.

stance phase has been included in the optimizing parameters. Then, following a slightly modified version of the approach to calculate the largest 1-step controllable step-down (Section 3.5), we calculated the largest 2-step controllable step-down and push for all CoM-offsets.

The results are shown in Figures 3.10 and 3.11. It shows that a significant increase of the largest controllable step-down and push can be realized by allowing hip actuation during two steps (note the logarithmic scale). An interesting observation is that placing the CoM on the hip is the worst option for two-step recoveries. In this case, the largest 2-step controllable step-down and push are approximately a factor 10 smaller than for the optimal CoM-location. A possible explanation is found by looking at the torque profiles used to recover from the disturbance, which are also shown in Figures 3.10 and 3.11. The average applied torque during the stance phases is clearly negative for the non-zero CoM-offsets. Negative torques indicate energy absorption, as the leg-torso angle increases during a stance phase. So, the increased energy

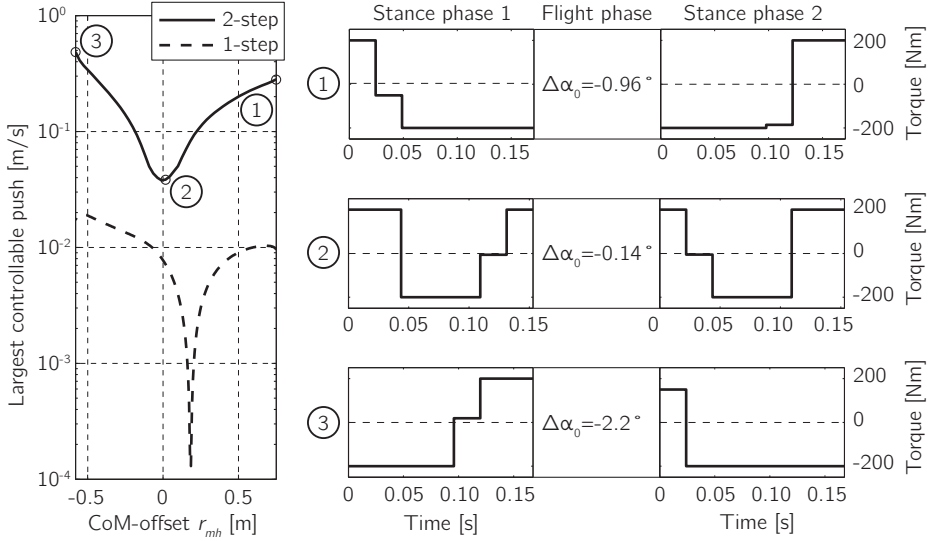


Figure 3.11: Approximation of the largest 2-step controllable push versus the CoM-offset r_{mh} . The largest 1-step controllable push is also shown for reference. The strategies to recover from the largest 2-step controllable push are shown for the optimal CoM-offset above the hip (1), the CoM on the hip (2) and the optimal CoM-offset under the hip (3). The recovery strategy consists of hip actuation during the first and second stance phase and a temporary adaptation of the angle-of-attack $\Delta\alpha_0$ between the first and second stance phase. Notice that placing the CoM exactly on the hip is the worst option for two-step recovering strategies.

level after a step-down or push is reduced to the regular energy level by applying negative torques on average. In contrast, when the CoM is located on the hip, the average applied torque equals exactly 0 to keep the pitching velocity undisturbed. The decoupled dynamics prevent the system from applying mainly negative torques, which makes it more difficult for a system with the CoM located on the hip to lose its energy. Summarizing, the coupling between pitching dynamics and the angle-of-attack allows the system to shift the average applied torque to a substantial negative value, which simplifies the required energy absorption after a step-down and herewith increases the largest 2-step controllable disturbance.

3.7.3 Validation of simplifications

Two simplifications were introduced to calculate the 1-step largest controllable disturbance. Linearity was assumed and only the torque limit T_{max} was considered in the calculation. In this section, we test to which extent these simplifications are

justified.

Linearization

To validate the linearization, we performed a very time-consuming optimization for non-infinitesimal disturbances. For a couple of CoM-offsets the system has been exposed to a range of step-downs. For each step-down, a non-gradient-based optimization method (Nelder-Mead method) has been used to find the corrective torque signal with the lowest torque demand. Once an optimal corrective signal was found, the magnitude of the step-down was increased and, again, the optimization method was used to find the optimal actuation. The initial guess of the new optimization was chosen as the optimal solution for the previous disturbance. This process has been repeated until the required torque for the optimal solution exceeded T_{max} . The magnitude of the corresponding step-down was designated as the largest 1-step controllable disturbance. For computational time and convergence issues, the torque signal was parameterized by 9 parameters instead of 13.

The results of the optimization are shown in Figure 3.12 together with the linear approximation. The figure shows that the linear approximation matches the real estimated largest 1-step controllable disturbance quite well, especially for a CoM-offset larger than -0.2 m. The actuation signals as approximated by the linear model evaluation and the actuation signals as calculated by the optimization also look similar (see Figure 3.12). Therefore, the linearity simplification seems to be justified.

Only torque limit

The other simplification concerned the existence of valid recovery strategies for non-infinitesimal disturbances. In Section 3.5.2, we assumed that exceeding the torque limit T_{max} is the major reason why valid recovery strategies do not exist. All other possible reasons for non-existence of recovery solutions were omitted. The large optimization has shown that this simplification is valid. The step-down did not become uncontrollable and the corresponding recovery motions did not come close to failure modes. The torque limit T_{max} is indeed the limiting factor for the correction after a disturbance.

Nevertheless, two important things have to be noticed. At first, the applied torque may not be negative at touchdown, otherwise the foot will immediately lose contact and the model will stumble. Although it looks as if the initial torque in Figure 3.12 (dashed line) starts negative, it actually starts at zero and then gradually takes the value of the first torque parameter p_1 , which is negative for the recovery in Figure 3.12. This is the result of the torque restriction rule that is implemented to secure that the foot never loses contact before mid-stance.

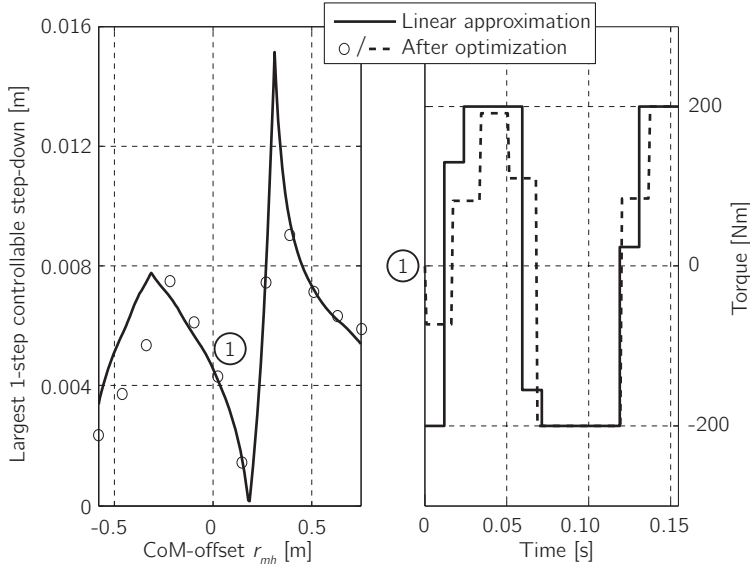


Figure 3.12: The approximation of the largest 1-step controllable step-down and the corresponding actuation signal show a good match with the optimization results. Therefore, the simplifications that were made to calculate the largest 1-step controllable disturbances can be justified.

Another thing to realize is that we assumed an infinite friction coefficient between the foot and the floor. A realistic friction coefficient could possibly introduce substantial sliding, which would make all results useless. Therefore, on every instant of the corrective motion, we calculated the lowest friction coefficient that would still prevent the foot from slipping. A typical profile for a step-down recovery is shown in Figure 3.13. It shows that for a friction coefficient of 1 (rubber on dry concrete), only at touchdown and just before liftoff a small sliding period can be expected. The major part of the corrective motion does not require a higher friction coefficient. Therefore, we expect that the optimal recovery strategies for a finite friction coefficient will look similar as the ones that we found for an infinite friction coefficient, except for some small differences at the beginning and end of the stance phase.

3.7.4 Limitations

The question that always arises for modeling studies is whether the exploited model is not too simple. We did not take into account motor limitations different from a maximal motor torque. Because we were interested in the mechanical optimum of the model, we also assumed the measurement system to be ideal, which is definitely not the case in real prototypes. Possibly the largest shortcoming of the model is

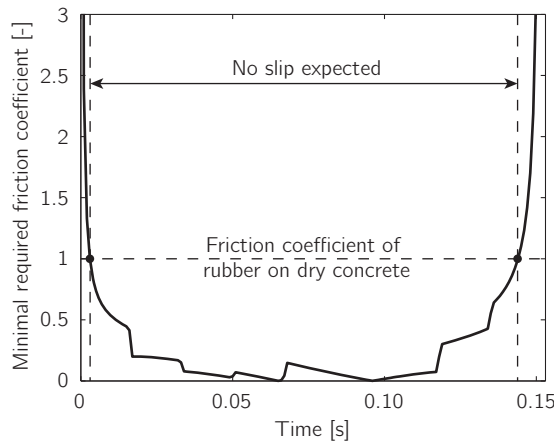


Figure 3.13: Lowest friction coefficient that prevents slip of the foot for the recovery motion of the largest 1-step controllable step-down when the CoM is located on the hip. It shows that no slip is expected during the major part of the motion. The applied torques to recover from the disturbance are shown in Figure 3.12 (dashed line).

the neglect of leg mass. Cherouvim and Papadopoulos (2005) designed a controller that stabilizes the spring-mass model. This controller was not able to stabilize a more complex model, including leg mass. They showed that controllers cannot be simply 'copied' to more complex models or prototypes. Our study should therefore not be interpreted as a proposal for a new controller for running robots. On the other hand, the spring-mass model has proven to be an effective model for describing and predicting human running (Blickhan, 1989; McMahon and Cheng, 1990). Despite of the substantial mass of human legs, many features can be described accurately with the model (He et al., 1991; Seyfarth et al., 2002). Therefore, it is likely that the main results that we found in this study also apply to models that are more complex. Future research will have to verify this.

Another limitation of the study is that we only investigated unactuated limit cycles. Allowing actuated limit cycles makes the problem of finding the largest controllable disturbance computationally too expensive. Actuated limit cycles with a proper controller might have a significantly better disturbance rejection. However, from all possible limit cycles, the unactuated ones are most conformable to the mechanical design approach, which generally strives for energy efficient running gaits.

3.8 Conclusion

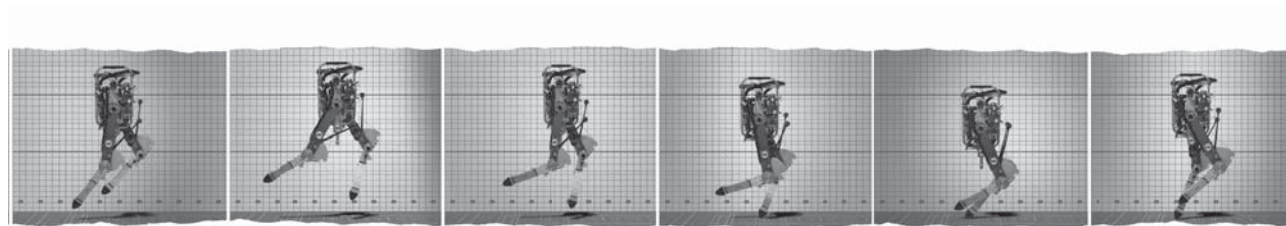
In this study, we investigated the optimal CoM-offset for running with limited hip actuation in terms of the disturbance rejection. Disturbance rejection was defined as the largest disturbance that could be corrected in one or two steps. We showed that:

- the optimal CoM-location depends on the type of the expected disturbance,
- for a step-down, the optimal CoM-location is above the hip,
- for a push on the CoM, the optimal CoM-location is under the hip,
- there exists a location of the CoM, slightly above the hip, for which the system becomes uncontrollable in one direction, which results in a very bad disturbance rejection,
- for two-step correcting strategies, placing the CoM on the hip is the worst option. An offset of the CoM-location can increase the disturbance rejection up to a factor of 10 compared to the CoM at the hip.

Therefore, we conclude that running with the CoM located on the hip, which is usually the case in running robots, is far from optimal.

Running Robot Phides

J.G.Daniël Karssen and Martijn Wisse,
Submitted to *IEEE RAS - Robotics & Automation Magazine*.



Abstract

The goal of this chapter is to introduce and describe the running robot Phides. Phides is the first running robot with knees that have a spring in parallel with the actuator for energy storage and release. The spring complicated the design of the actuation system, because the parallel spring must be decoupled during the swing phase of the leg. This chapter introduces a design with a latching mechanism, as well as with a series elastic spring implemented with a torsion bar in the knee joint. Due to the parallel spring, the required peak motor power is reduced by 26%, which allows the robot to achieve an unprecedented flight time of 54% of the stride.

4.1 Introduction

Running two-legged robots require very high peak power in the legs for push-off. Early two-legged running robots (Ahmadi and Buehler, 2006; Raibert, 1986; Zeglin and Brown, 1998) obtained the required power by using linear pneumatic drives in very lightweight legs. However, lightweight linear legs are not sufficiently realistic for future applications in exoskeletons and in humanoid robots (with more functionality than only running), and linear legs are neither a sufficient model for understanding human running. Therefore, at present most running robots have a more humanlike morphology, meaning that they have knees and significant leg mass.

The most well-known humanlike robots are Honda's Asimo (Honda, 2012) and similar full-body humanoid robots (Kajita et al., 2005; Nagasaka et al., 2004; Tajima et al., 2009). Their drive trains typically consist of electric motors with harmonic drives with high reduction ratios. Due to this design, it is difficult to generate high peak powers in the knees required for running, which becomes visible in the typically very short flight times of these robots. Better results have been obtained with the recent running robot Mabel by Grizzle et al. (2009), with flight times up to 40% of the stride. This success is largely due to the use of Series Elastic Actuation (Pratt and Williamson, 1995) where a spring is placed between the actuator and the driven limb. The spring can store and release energy, and therefor deliver peak power at the required instant, if controlled properly (Sreenath, 2011). However, since the spring is placed in series with the actuation, the spring force must also be provided by the actuator, so still very strong and heavy actuators are needed. A spring would truly be beneficial if it was mounted in parallel with the actuation. Although a patent by Honda (Takenaka et al., 2009) suggests that they apply this idea, we have not found

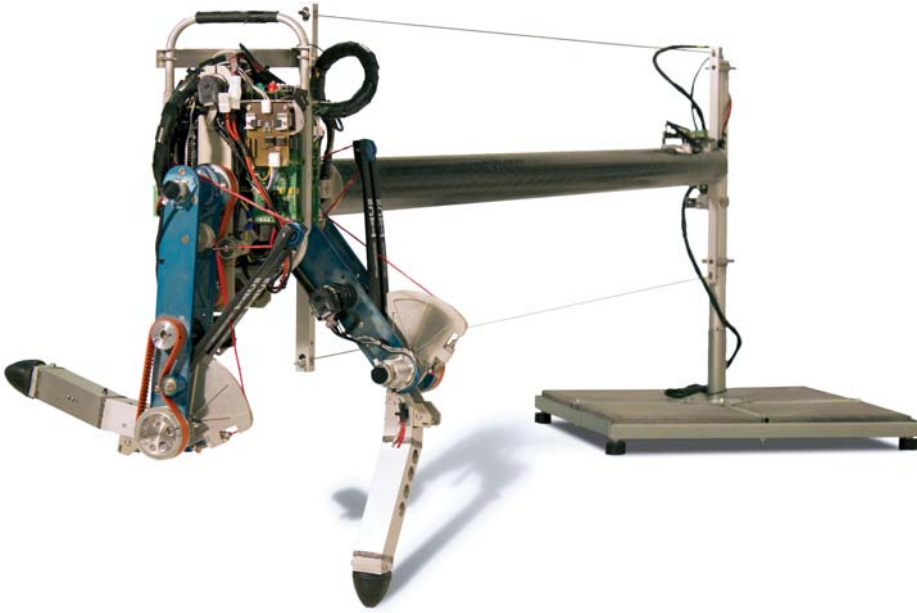


Figure 4.1: Running robot Phides with knees and significant leg mass. The special design feature of Phides is the use of parallel springs in the knees, which provide high peak powers during the stance phase, leading to humanlike gait with record flight times of 54% of the gait cycle.

any papers describing the design issues and the effects of applying parallel springs for running robots.

Therefore, we developed a running robot with parallel (and also serial) springs in the knee actuation. This chapter describes this new robot, named Phides¹, with a focus on the knee actuation system. The design and control are described in Sections 2 to 4, followed by a description of the running results in Section 5. The main conclusion in Section 6 is that Phides obtains a very humanlike running gait with a record flight time of 54% of the gait cycle.

4.2 Overall design layout

Phides, as shown in Figure 4.1, is a running robot, which is about 0.8 m tall and weighs 13.5 kg. The robot consists of a torso and two kneed legs with small, spherical feet. The robot is attached to a 2.2 m long boom construction to achieve planar

¹Phides (or Pheidippides) was the legendary messenger from Marathon to Athens.

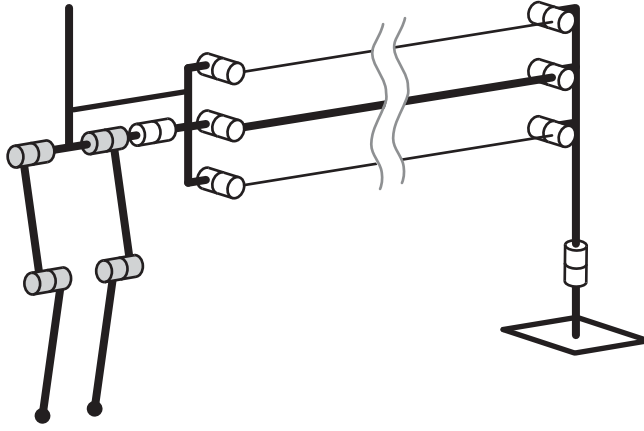


Figure 4.2: The degrees-of-freedom (DoF's) of running robot Phides. The grey joints are the actuated DoF's of the hip and knee joints. The white joints are the passive joints of the boom construction, which give the robot two external DoF's, x and y -position of the hip. Note that the rotation of the torso is not a DoF, as it is fixed to the boom construction.

behavior. The boom construction is implemented with a parallelogram mechanism that keeps the hip axis of the robot parallel with the ground, to reduce the sideways movement of the feet as the robot moves up and down. For all experiments in this chapter, the torso is rigidly fixed to the boom to eliminate the need to control the torso angle. This leaves 6 degrees-of-freedom (DoF's), namely two hip joints, two knee joints, and 2 external DoF's (x and y -position of the hip), see Figure 4.2.

The key design feature of this robot is the actuation mechanism for the knees. Phides' knees have a series elastic actuator as well as a parallel spring, as shown in Figure 4.3. The series elasticity is chosen mainly to protect the gearbox against large shocks at touchdown, and it also provides a way to implement torque control. The series elastic actuator only provides a small part of the total knee torque, as most of the torque is delivered by the parallel spring.

The parallel spring stores a large part of the kinetic energy of the robot during the first half of the stance phase and releases it during the second half of the stance phase. In this chapter, we keep the overall leg stiffness linear (i.e. an effective prismatic spring between the foot and the hip with constant stiffness) to be able to compare the results with the Spring-Loaded Inverted Pendulum (SLIP) model, the de facto standard model for running simulations (Blickhan, 1989; Blum et al., 2010; Ghigliazza

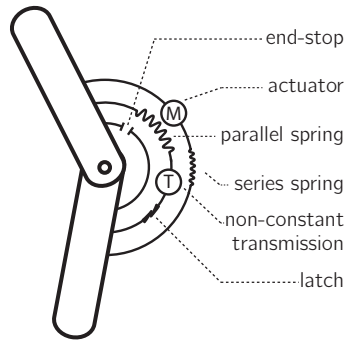


Figure 4.3: Schematic drawing of the knee actuation mechanism. The mechanism consists of a series elastic actuator as well as a parallel spring. The parallel spring is connected to the knee joint by a non-constant transmission and a latching mechanism. Next to the series elastic actuator and the parallel spring, there is an end-stop that prevents the knee from overstretching.

et al., 2005; Poulakakis and Grizzle, 2009b; Schwind and Koditschek, 1997; Seyfarth et al., 2002). The linear leg stiffness means that the actual rotational stiffness of the knee joint must be nonlinear, complicating the mechanical design as elaborated in the next section, especially since we want to test other (nonlinear) leg stiffness profiles in the future.

The main difficulty with the use of a parallel spring is its negative effect during the swing phase. When the leg is swinging forward, the knee should bend even more than the knee of the other leg, which is in stance phase. If the parallel spring would remain attached, then the actuator of the swing knee would need to provide a very high torque just to fight the parallel spring. Therefore, a latching mechanism is required that disconnects the parallel spring during the swing phase and reliably re-connects it for the stance phase. The next section elaborates the design of the required mechanisms.

4.3 Mechanical realization

The idea of using parallel and serial springs in the knees resulted in the design of the robot Phides as shown in Figure 4.1. An overview of the robot dimensions and mass properties is given in Figure 4.4 and Table 4.1. The joint specifications are given in Table 4.2.

The knee actuation system, which is shown in Figure 4.5, has a part in parallel and a part in series with the actuator. The parallel part consists of the parallel spring, a

Table 4.1: Dimensions and mass properties

	torso	upper leg	lower leg
Mass m [kg]	7.41	2.54	0.51
Moment of inertia J [kgm ²]	0.080	0.036	0.005
Length l [m]	0.3	0.3	0.3
Vertical offset CoM c [m]	0	0.183	0.139
Horizontal offset CoM w [m]	0	0	0

Table 4.2: Joint specifications

	Hip joints	Knee joints
Actuator	90W Maxon RE35 30V	90W Maxon RE35 30V
Gear ratio	1:55	1:55
Range of motion [rad]	-1.57 to 1.57	0.52 to 2.09
Series stiffness	-	215 Nm/rad
Parallel stiffness	-	Nonlinear ^a

^a The rotational spring is nonlinear in such a way that leg experiences a linear 5.06 kN/m spring between the foot and the hip.

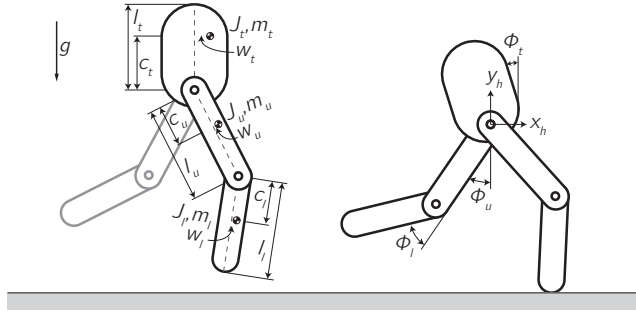


Figure 4.4: The definitions of the robot parameters and the robot state variables. Although the upper body is kept upright by mechanical fixation in the experiments in this chapter, for completeness we also provide the upper body parameters and variables. The actual values of the robot parameters are given in Table 4.1.

nonlinear transmission, a knee pulley, and a latching mechanism. The parallel spring is constructed of fiberglass leaf springs from a crossbow (PSE TAC15). These leaf springs were selected because of their high energy storage to weight ratio (640 J/kg). The leaf springs are connected with a bowstring to a set of non-circular pulleys, which act as a nonlinear transmission. The non-circular pulleys were selected such that the parallel spring creates an effective prismatic spring between the foot and the hip with a constant stiffness of 5.06 kN/m. The pulley transmission is designed to be changed easily, because we plan to test the effect of the leg stiffness profile in the future. The non-circular pulleys are connected with another bowstring to the knee pulley. The knee pulley is attached with a latching mechanism to the lower leg. The latching mechanism makes it possible to decouple the parallel spring during the flight phase. The latching mechanism is a rotating ratchet latch, which is actuated by a small solenoid (Keyswitch - SM0012VDC). The knee joints are equipped with an end stop that prevents the knees from extending further than the rest length of the parallel spring.

In parallel with the parallel spring is the actuation system that consists of motor, a transmission, and a series spring. The motor is a brushed DC-motor (Maxon RE35 30V) with a planetary gearbox with a gear ratio of 1:33. The motor is connected by a belt transmission, with a gear ratio of 3:5, to the series spring. The series spring is a torsion bar with a stiffness of 215 Nm/rad, which is located inside the hollow knee shaft. The stiffness of the series spring and the overall gear ratio were selected to maximize the amount of energy the actuator can put into the system while the robot is hopping. It is worth noting that the torsion bar in the knee was the part that required the most attention; it failed a number of times, first due to the heavy

load on the welds and (after a redesign) due to unexpected plastic deformation. The torsion-bar-in-hollow-shaft design is very elegant and compact but very tricky to produce.

4.4 Controller

Phides is controlled with a simple state machine running on an onboard computer, which is connected to five local motion control boards as slaves.

4.4.1 Electronics

The robot is equipped with digital incremental encoders on all the joints of the robot and the boom construction. The resolution of the encoders is $6 \cdot 10^{-5}$ rad for hip joints and $2 \cdot 10^{-4}$ rad for the knee joints and boom degrees-of-freedom. By using the measured angles and also using the calculated angular velocity of all joints, the robot effectively measures its full state. All encoders are directly mounted to the joints, except for the hip encoders. The hip encoders are mounted on the back of the DC-motors. Due to elasticity in the hip transmission, there can be a difference between the joint angle and the encoder reading. When post-processing the sensor data, we correct for this error by subtracting a term based on the estimated joint torque and transmission stiffness.

The knee joints are equipped with extra encoders on the back of the motors. These encoders combined with the joint encoders enable the robot to measure the deflection of the series spring. This deflection multiplied with the spring stiffness leads to the torque applied by the series spring on the joint. The resolution of this torque measurement is 0.043 Nm/rad.

In addition to the encoders, the robot has contact sensors in both feet to sense ground contact and push switches for commands from the operator.

The robot is controlled by an onboard central computer and five local control boards. The central computer is a PC104 computer stack (1 GHz Diamond Systems Poseidon board, 512 MB RAM) which communicates over a serial connection at 200 Hertz with local control boards. The local boards are developed within the Delft Biorobotics Lab and are used for a number of robots in the lab (Delft Biorobotics Lab, 2012). Each local board can process two encoders and control the voltage to two motors. The local boards run a local PD-controller at 1 KHz, for which the setpoints and control gains are provided by the central computer.

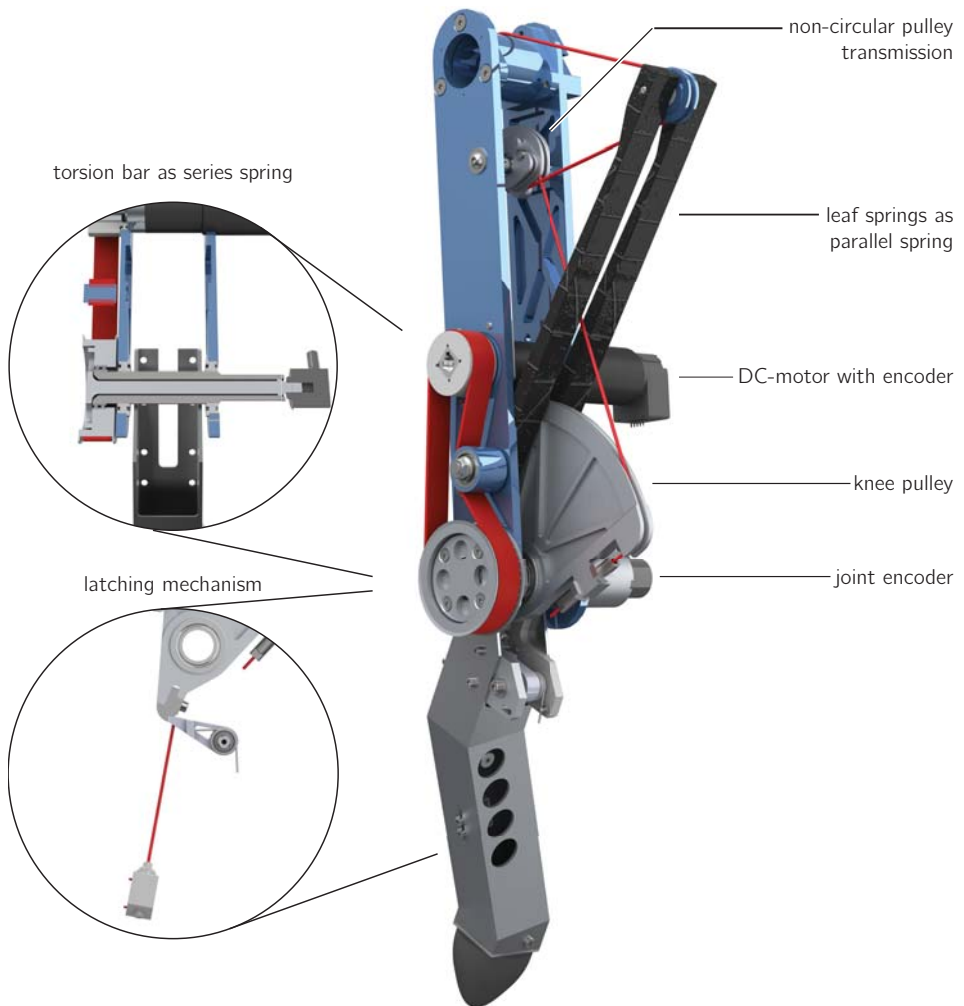


Figure 4.5: Render of the leg design. The parallel spring is constructed of leaf springs from a crossbow and is attached to the knee joint by a nonlinear transmission and a latching mechanism. The series spring is a torsion bar inside the hollow knee shaft.

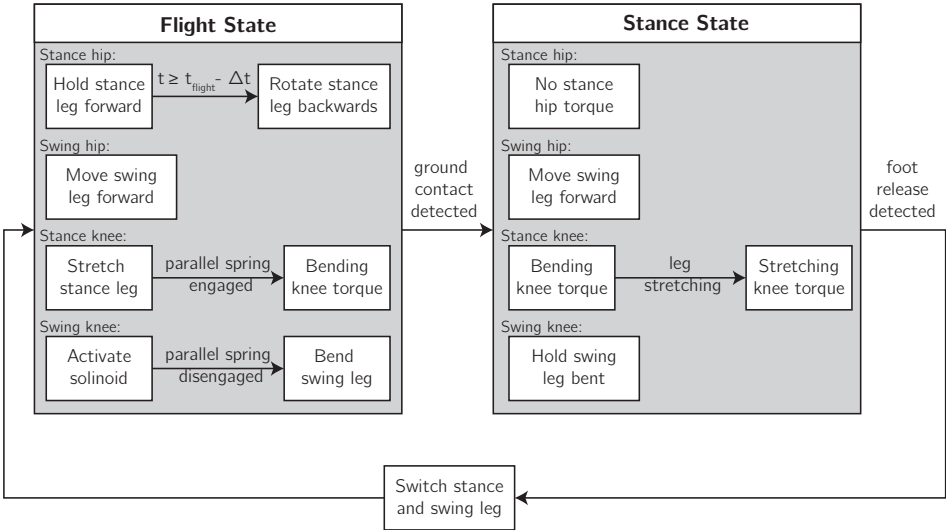


Figure 4.6: The state machine controller used on Phides. The main state machine has just two states, a flight state and a stance state. Within these two states, there is separate controller for each of the four joints.

4.4.2 Control architecture

The robot is controlled by a state-machine based controller, which is shown in Figure 4.6. The main state machine consists of two states, one for the flight phase and one for the stance phase. The switching between these states is based on the detection of ground contact or release by the contact sensors in the feet. Within these two main states, there is a separate controller for each of the four joints. In the **flight state**, these controllers take the following actions:

Stance hip joint The stance upper leg, which is the leg that is about to make ground contact, starts the flight phase in a forward position. The stance upper leg is kept in this position until 0.05s before the expected moment of touchdown. At that moment, the stance leg starts rotating backwards with a constant angular rate of 2 rad/s. This is done to make the leg angle at touchdown a function of the flight time, called swing-leg retraction, which is known to increase the disturbance rejection (see Chapters 5 and 6).

Swing hip joint The swing leg is just released from the ground at the start of the flight phase and starts with a large backwards velocity. This backwards velocity is stopped and the leg is moved forward, by tracking a quadratic spline trajectory

with a PD-controller. This trajectory consists of two quadratic polynomials, which are chosen such that maximal accelerations are minimal.

Stance knee joint The stance knee starts the flight phase bent with a decoupled parallel spring. The leg is extended up to the zero length of the parallel spring to engage the spring. Next, the leg is bent with a constant knee torque to pre-load the parallel spring before touchdown.

Swing knee joint The swing knee starts the flight phase stretched with the parallel spring engaged. First, the spring is decoupled by activating the latch actuator. Next, the leg is bent to get enough ground clearance to swing the leg forward.

And in the **stance state** the joint controllers take the following actions:

Stance hip joint The stance hip joint applies zero torque between the stance leg and the torso during the stance phase. This is done to prevent that unreasonably high torques are applied on the torso, which could not be applied if the torso was not fixed to the boom construction.

Swing hip joint During the stance phase, the swing leg is moved further forward using the same kind of controller as during the flight phase.

Stance knee joint The stance knee applies a bending torque during the first half of the stance phase. In the second half, when the leg is extending, an extending torque is applied. This way the knee actuator does only positive work.

Swing knee joint The swing knee stays bent during the whole stance phase.

4.5 Results

4.5.1 Gait characteristics

Using the controller described in the previous section, the robot is able to run with speeds up to 1 m/s, which is a normalized speed² of 0.42. The maximal flight time is achieved at a speed of 0.84 m/s, with an average step length of 0.32 m and an average step time of 0.39 s. At that speed, 54% (0.21 s) of the time the robot is not in contact with the ground. An overview of the gait characteristics with standard deviations is given in Table 4.3. With these characteristics, Phides has a higher flight time than comparable robots, see Table 4.4.

²Normalized speed is defined as $v/\sqrt{gL_0}$.

Table 4.3: Gait characteristics, obtained from 166 running steps (3.6 full circles of the boom)

Characteristic	Mean value	Standard Deviation
Speed	0.82 m/s	0.093 m/s
Step length	0.32 m	0.030 m
Step time	0.39 s	0.015 s
Flight time	0.21 s (54%)	0.018 s
Stance time	0.18 s (46%)	0.005 s

Table 4.4: Robot comparison. Phides has the longest flight time compared to all other robots with knees, only topped by robots with non-human pogo-stick-like legs.

	% flight time
Robots with springs and knees	
Phides	54%
Kenken (Hyon and Mita, 2002)	~53%
Mabel (Grizzle, 2012)	39%
Pneumatic muscles biped (Hosoda et al., 2006)	22%
Athlete robot (Niiyama et al., 2012)	~22%
Passive runner (Owaki et al., 2010)	16%
Robots with springs and telescopic legs	
2D biped (Hodgins and Raibert, 1991)	77%
ARL II monopod (Ahmadi and Buehler, 2006)	~53%
Robots with knees without springs	
Partner robot (Tajima et al., 2009)	29%
HRP-2LR (Kajita et al., 2005)	~28%
Rabbit (Morris et al., 2006)	25%
Asimo (Honda, 2012)	~25%
Hubo2 (Cho et al., 2011)	12%
Qrio (Nagasaka et al., 2004)	~4%

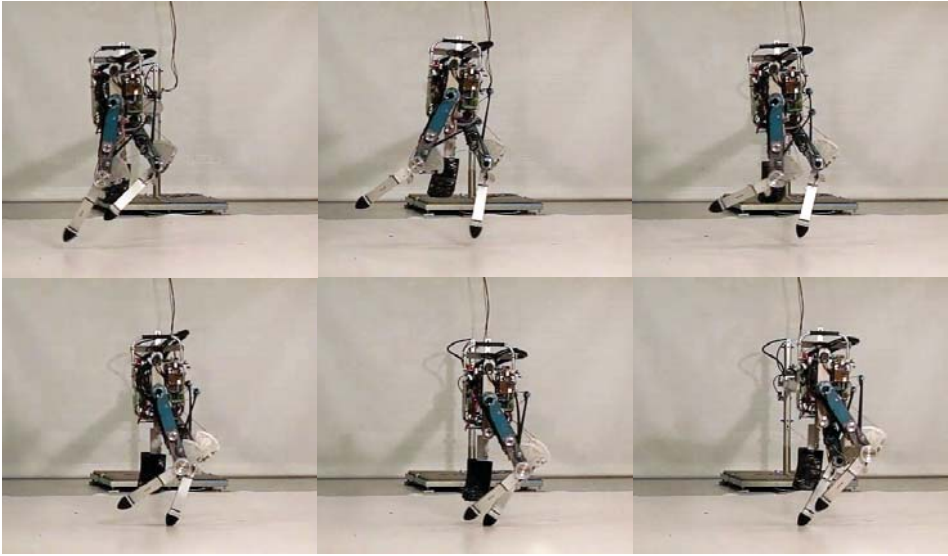


Figure 4.7: Stills from a video showing the robot motion during a single step. In the fourth still (bottom-left), the robot is in contact with the ground with its left leg and the leaf spring of this leg can be seen bending. This video and more videos are available as online supplementary content at <http://dbl.tudelft.nl>.

4.5.2 Motions

Figure 4.7 shows the robot during a running motion. It is clearly visible that the leaf springs are bending during the stance phase. In addition, it is visible that the torso, although it is fixed to the boom construction, is rotating a bit. This undesired motion is caused by compliance in the connection between the torso and the boom construction.

Figure 4.8 shows all joint angles and the hip position over 166 steps. The data of the steps is synchronized at the moment of liftoff. The horizontal hip position is defined to be zero at liftoff. The white areas indicate the average duration of the flight phase and the grey areas indicate the stance phase. The angles and hip positions are defined as in Figure 4.4. For the hip and knee angle, the grey lines are for (what will become) the stance leg and the black lines are for the swing leg.

Both the torso angle and the hip angle show a small spike at the time of touchdown. This spike is caused by the angle correction method, as discussed in Section 4.4.1, misestimating the hip torque, due to the sudden impact forces.

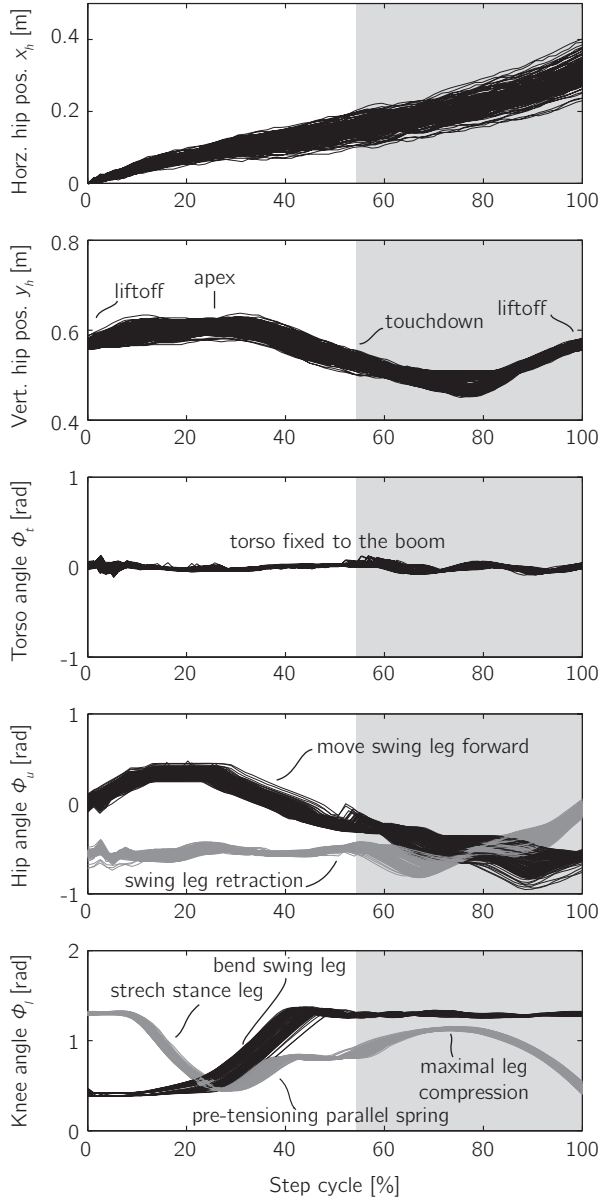


Figure 4.8: The hip position and joint angles for 166 steps at 0.82 m/s. For the hip and knee angle, the grey lines are for (what will become) the stance leg and the black lines are for the swing leg. The white areas indicate the average duration of the flight phase and the grey areas indicate the stance phase.

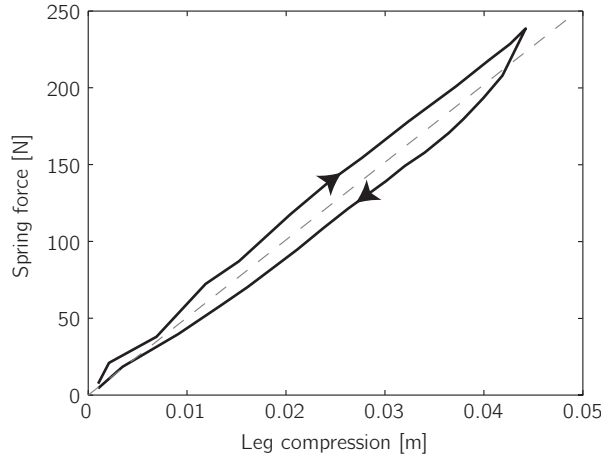


Figure 4.9: The force applied by the parallel knee spring in the direction of the line between the hip and the foot as a function of the leg compression. The dashed grey line is a linear fit of the measured force. The force profile is close to the intended linear stiffness and the spring system has a low hysteresis.

4.5.3 Knee actuation performance

The non-circular pulleys were designed such that the parallel spring creates an effective prismatic spring between the foot and the hip with constant stiffness. To test how well this was achieved, we did an experiment, in which a cable with a force sensor was connected between the hip joint and the foot. This cable was slowly shortened while the cable force and the leg length were recorded. The results of this experiment, as seen in Figure 4.9, show that the force profile is close to the intended linear stiffness and that the system has a low hysteresis.

To test how well the parallel spring can store and release energy, we performed a drop experiment. In this experiment, the robot is dropped from about 0.6 m on one leg, with the knee motor and series spring disconnected. Figure 4.10 shows the potential energy and the energy in the parallel spring during the drop test. The difference in potential energy between two succeeding apex points is a measure of the energy loss. This energy loss is caused by impact of the unsprung leg mass and inertia, the friction losses, and the spring hysteresis. This experiment suggests that the impact losses are the major cause of the energy loss, as there is almost no energy loss between the moment of maximal knee compression and apex.

Figure 4.11 shows the torque and power of the parallel spring and of the motor with the series spring of the stance leg while running at about 0.82 m/s. The parallel spring

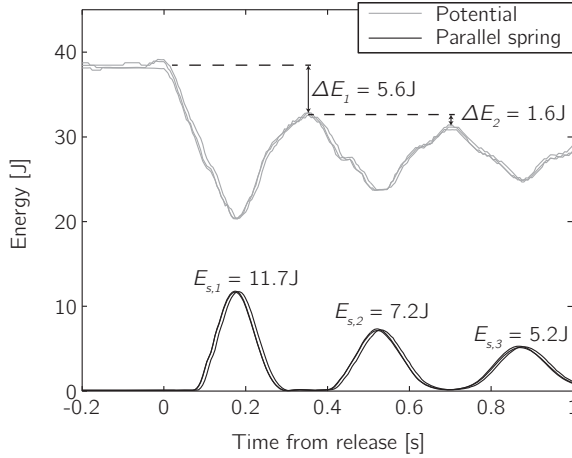


Figure 4.10: Results of 3 trials in the drop experiment. In this experiment, the robot is dropped from 0.6 m with the series spring and knee actuation decoupled. The lines show the potential energy and the energy in the parallel spring. The energy losses ΔE are caused by impact losses and internal losses, like spring hysteresis and friction.

generates no torque during the first part of the flight phase as it is disengaged. Just before touchdown, the parallel spring engages and it is pre-tensioned by the motor through the series spring. During the stance phase, the parallel spring compresses and exerts a stretching torque on the knee joint. The motor with the series spring exerts a compressing force for the first half of the stance phase and a stretching torque in the second half of the stance phase.

The total absolute torque on the knee joint is maximal during push off, as both the parallel spring and the motor apply a stretching torque and is on average 54 Nm. Of this torque, 43 Nm comes from the parallel spring and 11 Nm from the actuator through the series spring. The peak joint power is also reached during the push off and is on average 300 W. The peak positive motor power during a step is on average only 221 W, which indicates that the parallel spring reduces the required motor power by 79 W or 26%. In addition, the series spring seems to protect the motor, as Figure 4.11 shows that there are also no high torques on the motor at touchdown.

4.6 Conclusion

This chapter introduced and described the running robot Phides. Phides is the first running robot with knees with a parallel spring for energy storage and release. Due to the parallel spring, the robot achieves an unprecedented flight time of 54% of

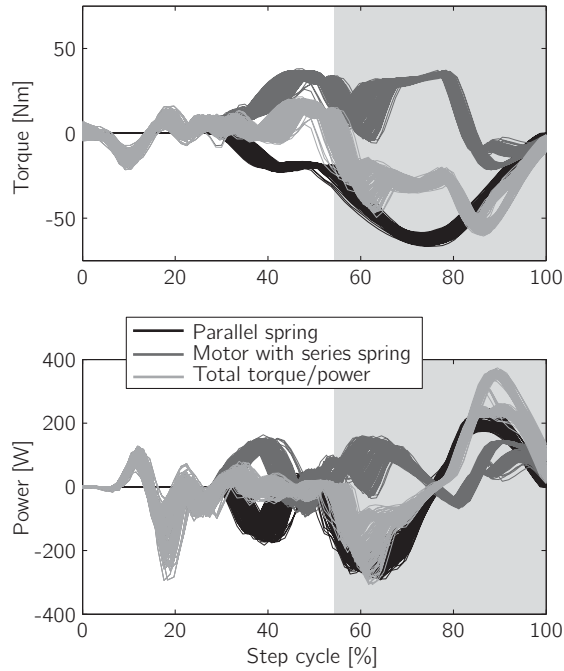


Figure 4.11: The knee torque and power of one knee joint during a running motion with a speed of 0.82 m/s. The white areas indicate the average duration of the flight phase and the grey areas indicate the stance phase.

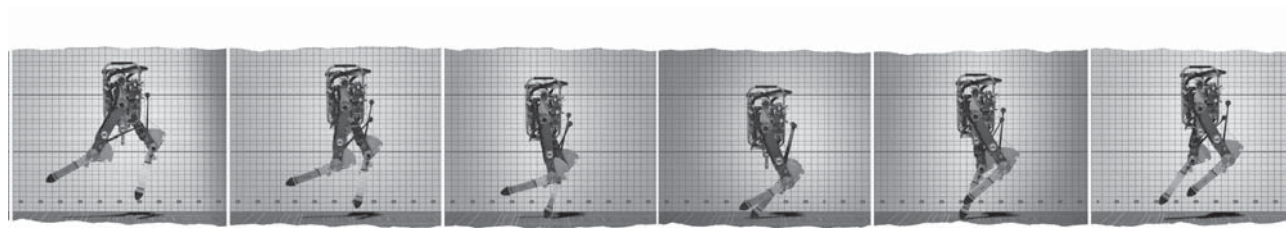
the stride. In addition, Phides does achieve a top speed of about 1m/s. In the future, Phides will be used to validate our simulation studies of the running gait. This will include studies into the effects of swing-leg retraction on energy efficiency and disturbance rejection (Chapters 5 and 6) and into the effect of nonlinear leg stiffness (Chapter 2).

Acknowledgement

This research is funded by the Dutch Technology Foundation STW, applied science division of NWO. Jan van Frankenhuyzen and Dennis Lakerveld have made a major contribution to the mechanical design of the robot, Guus Liqui Lung has developed the electronics, Eelko van Breda and Erik Schuitema have developed the onboard software, and Karin Griffioen and Leonard van Bommel have conducted the spring stiffness profile experiment.

The Optimal Swing-Leg Retraction Rate for Running

J.G.Daniël Karssen, Matt Haberland, Martijn Wisse, and Sangbae Kim,
IEEE International Conference Robotics and Automation,
2011, pp. 4000-4006.



Abstract

Swing-leg retraction was introduced as a way to improve the stability and disturbance rejection of running robots. It was also suggested that the reduced foot speed due to swing-leg retraction can help reduce impact energy losses, decrease peak forces, and minimize foot slipping. However, the extent to which the swing-leg retraction rate influences all these benefits was unknown. In this chapter, we present a study on the effect of the swing-leg retraction rate on these benefits. The results of this study show that swing-leg retraction can indeed improve the performance of running robots in all of the suggested areas. However, the results also show that, for moderate and high running speeds, the optimal retraction rate for maximal disturbance rejection and stability is different from the optimal retraction rate for minimal impact losses, peak forces, and foot slipping. This discrepancy indicates an inherent tradeoff to consider when selecting the retraction rate for a robot control system: in general, retraction rate can be optimized for better stability and disturbance rejection or for more favorable efficiency, impact forces, and footing stability, but not all simultaneously. Furthermore, this tradeoff becomes more severe as running speed increases.

5.1 Introduction

There has been great interest in developing dynamic legged robots for decades. Recently, legged robots began to demonstrate advantages over conventional wheeled and tracked vehicles over highly rough terrain (Playter et al., 2006).

One of the most effective ways used to control the motion of dynamic legged robots is to adjust the angle at which the legs make contact with the ground, the so-called angle-of-attack. This is implemented by controllers like Raibert's foot placement strategy (Raibert, 1986), constant angle-of-attack control (Blickhan, 1989; Kim et al., 2006), and passive foot placement (McGeer, 1990a). They show that angle-of-attack significantly affects the dynamics of running robots. However, leg speed with respect to the ground at the moment of foot contact may also be very important to running robot performance.

Animals and humans seem to use a leg speed control strategy called swing-leg retraction (Blum et al., 2010): they rotate the front leg backward toward the end of the flight phase. Seyfarth et al. (2003) showed that swing-leg retraction can increase the stability of the running motion. For walking, Wisse et al. (2005a) and Hobbelen

and Wisse (2008) showed that swing-leg retraction can also increase the disturbance rejection.

Swing-leg retraction is also believed to offer advantages other than improved stability and disturbance rejection. By reducing the relative speed between the foot and the ground at the moment of contact (Daley and Usherwood, 2010; Raibert, 1986), swing-leg retraction can reduce impact losses, the chance of slipping, and damaging impact forces.

The hypothesized benefits of swing-leg retraction are well known, however the optimal swing-leg retraction rate is unknown. Also, it is unknown how the optimal swing-leg retraction rate depends on system parameters, like leg stiffness and horizontal velocity. Knowledge of the optimal swing-leg retraction rate is crucial for implementing swing-leg retraction on a running robot, because an excessive retraction rate can adversely affect running performance. The goal of this chapter is to provide methods and simulation results that determine the retraction rates that result in the optimal running performance.

The remainder of this chapter is organized as follows. Section 5.2 describes the model used in this study. In Section 5.3 the effect of the swing-leg retraction rate on the disturbance rejection of this model is discussed. Next, the effect of the swing-leg retraction rate on the other advantages of swing-leg retraction, like the reduced impact losses, is discussed in Section 5.4. The chapter ends with a discussion in Section 5.5 and the conclusions in Section 5.6.

5.2 Simulation Model

For this study, we use the simple spring-mass model that Blickhan introduced for analyzing running motions (Blickhan, 1989). This model consists of a point mass on a massless spring (see Figure 5.1). Some refer to it as the spring loaded inverted pendulum (SLIP) model, because the spring behaves like an inverted pendulum during the stance phase (Schwind and Koditschek, 1997). The simplicity of this model makes it desirable for studying fundamental properties of running without interfering complexities. Note that this model does not include collision losses, impact forces, or the possibility of slipping due to the massless leg. However in Section 5.4, we introduce leg mass and inertia to investigate the effect of swing-leg retraction on the collision losses, impact forces, and the likelihood of slipping.

The running motion of this model has two distinct phases, a stance phase and a

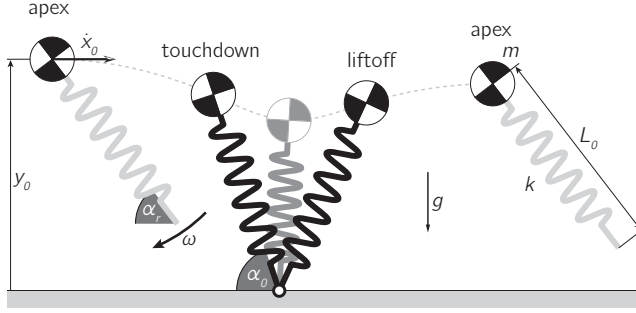


Figure 5.1: A simple running model with swing-leg retraction. The model consists of a point mass body and a massless spring leg. At the apex point, the leg is set at an angle α_r with respect to the ground and starts rotating with a rate ω . The leg angle at touchdown α_0 depends on the time between apex and touchdown.

flight phase. During the stance phase, the motion is given by:

$$m \begin{bmatrix} \ddot{x} \\ \ddot{y} \end{bmatrix} = \begin{bmatrix} -\cos \alpha \\ \sin \alpha \end{bmatrix} F_s + \begin{bmatrix} 0 \\ -mg \end{bmatrix}, \quad (5.1)$$

where α is the angle that the leg makes with the ground and F_s is the spring force. The leg spring is a linear spring, so the spring force is proportional to the leg compression ΔL ,

$$F_s = k\Delta L, \quad (5.2)$$

where k is the leg stiffness. The stance phase ends and the flight phase begins at liftoff, when the spring leg is at its rest length L_0 . During the flight phase, the point mass follows a ballistic trajectory, as the spring does not apply any force. The swing leg assumes an angle-of-attack α_r with respect to the ground at apex and begins rotating backward with swing leg retraction rate ω . The flight phase ends and the stance phase begins when the leg touches down. The leg angle at touchdown depends on the time between apex and touchdown.

For the purpose of analysis, the start of a step is defined as the apex of the flight phase. At apex, the vertical velocity is zero and the state of the model is described by two initial conditions, apex height y_0 and horizontal velocity \dot{x}_0 . The initial conditions of a step can be mapped on the initial conditions of the next step with the stride function S ,

$$\mathbf{v}_{n+1} = S(\mathbf{v}_n) \quad \text{with } \mathbf{v} = \begin{bmatrix} y_0 \\ \dot{x}_0 \end{bmatrix}. \quad (5.3)$$

Table 5.1: Model parameter values

Parameter	Symbol	Value	Unit
Mass	m	80	[kg]
Gravitational constant	g	9.81	[m/s ²]
Nominal leg length	l_0	1.0	[m]
Leg stiffness	k	20000	[N/m]
Angle-of-attack	α_0	66.44	[°]
Apex height	y_0	1.0	[m]
Horizontal velocity	\dot{x}_0	5.0	[m/s]

The stride function can have fixed points, where the initial conditions result in the same initial conditions after a single step,

$$\mathbf{v}^* = S(\mathbf{v}^*). \quad (5.4)$$

If the model is started in a fixed point, it will undergo a periodic motion. This repeated motion is called a limit cycle.

Throughout this study, we use humanlike values for the model parameters, unless otherwise noted. These humanlike values are taken from Seyfarth et al. (2002) and are shown in Table 5.1. The angle of the leg at apex α_r is set depending on the retraction rate ω such that the leg angle at touchdown α_0 is 66.44°, which is the value required for limit cycle running at the chosen apex height and apex horizontal velocity. However, even though the leg angle at apex α_r remains constant for a given ω , the leg angle at touchdown α_0 changes if the model is disturbed from its limit cycle.

5.3 Disturbance rejection

Swing-leg retraction is introduced as a simple control strategy to increase the disturbance rejection of running systems. In this section, we investigate how the disturbance rejection is influenced by the swing-leg retraction rate. First, we analyze how the retraction rate influences the model's response to very small disturbances. Next, we look at the largest single disturbance the model can handle without falling. At the end of this section, we investigate how well the model with swing-leg retraction can accommodate multiple disturbances in succession.

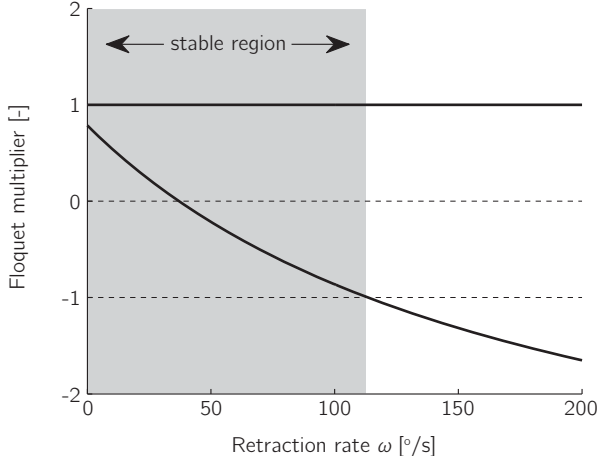


Figure 5.2: The two Floquet multipliers on the linearized step-to-step map as functions of the retraction rate. One of the Floquet multipliers is always one, due to the energy conservative nature of the model. The other Floquet multiplier decreases with an increasing retraction rate. At a retraction rate of 37 °/s the this Floquet multiplier is zero, indicating maximal stability. Beyond a retraction rate of 113 °/s the magnitude of one of Floquet multipliers is larger than one, indicating that the model is unstable at these retraction rates.

5.3.1 Stability

The stability of a running model can be assessed by looking at the stability of the linearized step-to-step behavior (Hobbelen and Wisse, 2007a; McGeer, 1990a; Seyfarth et al., 2003). This stability is expressed in terms of Floquet multipliers, which are the eigenvalues of the linearized step-to-step map A ,

$$\Delta \mathbf{v}_{n+1} = A \Delta \mathbf{v}_n \quad \text{with } \Delta \mathbf{v}_n = \mathbf{v}_n - \mathbf{v}^*. \quad (5.5)$$

The Floquet multipliers indicate how fast the model converges back to the limit cycle after a small deviation from the limit cycle. A system is stable if the magnitude of all Floquet multipliers is less than or equal to one. Our running model has two Floquet multipliers as it has two initial condition variables.

Figure 5.2 shows how the two Floquet multipliers vary across a range of swing-leg retraction rates. Due to the energy conservative nature of the model, one of the Floquet multipliers is always one: disturbances to energy level persist. Neither swing-leg retraction nor any other angle-of-attack controller can affect this. The other Floquet multiplier decreases with increasing retraction rate. At a retraction rate of 37 °/s this Floquet multiplier is zero, indicating that the stability of the model

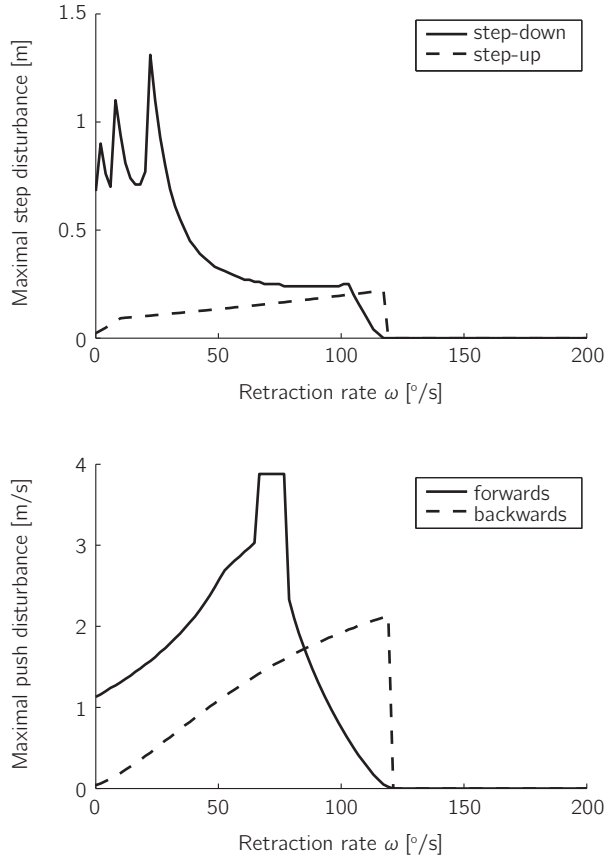


Figure 5.3: The maximal single disturbance after which the model can run a 100 steps without falling as function of the retraction rate for four kinds of disturbances.

is optimal at this rate. The zero Floquet multiplier causes the model to return to the original limit cycle within a single step of small, energy-neutral disturbances. For higher retraction rates the model becomes less stable and beyond a retraction rate of 113° /s the model is unstable. This indicates that retraction rates higher than 113° /s are not useful when swing-leg retraction is the complete control strategy, as even the smallest disturbance will cause the model to deviate from its limit cycle.

5.3.2 Single disturbance

The Floquet multipliers only indicate whether the model is stable with respect to small disturbances. They do not predict how the model will respond to large distur-

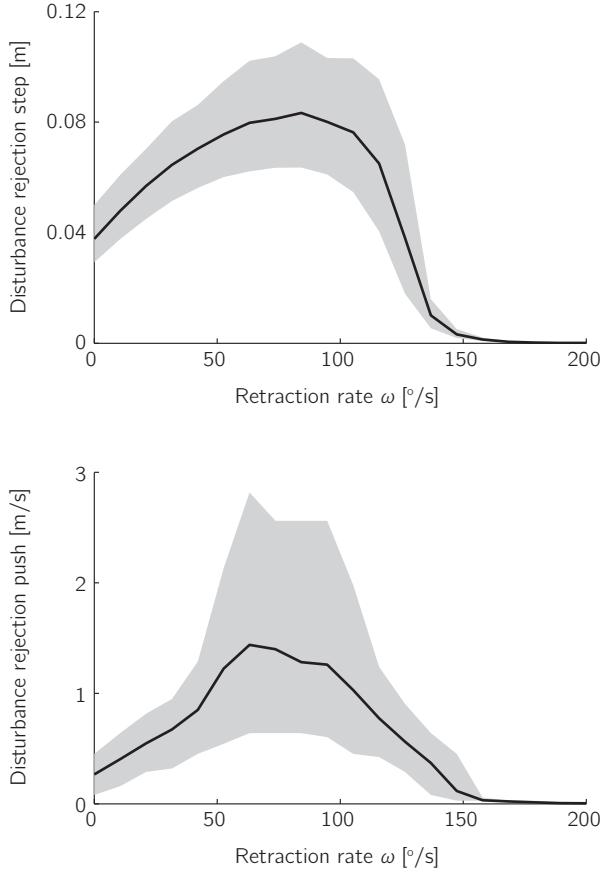


Figure 5.4: The maximal random disturbance as function of the retraction rate for step and push disturbances. The black line is the average of a 100 trials and the gray area indicates 95% confidence of the trials.

bances because they assume a linear disturbance response even though the model's disturbance response is actually nonlinear. To investigate the response to realistic disturbances, we determine the maximal disturbance from which the model can recover for a range of retraction rates. Two disturbance types are used, a terrain step and a push. Both disturbances are implemented as a change in the initial conditions. The step disturbance results in a change of the apex height,

$$y_0 = y_0^* + d_{step}, \quad (5.6)$$

$$\dot{x}_0 = \dot{x}_0^*, \quad (5.7)$$

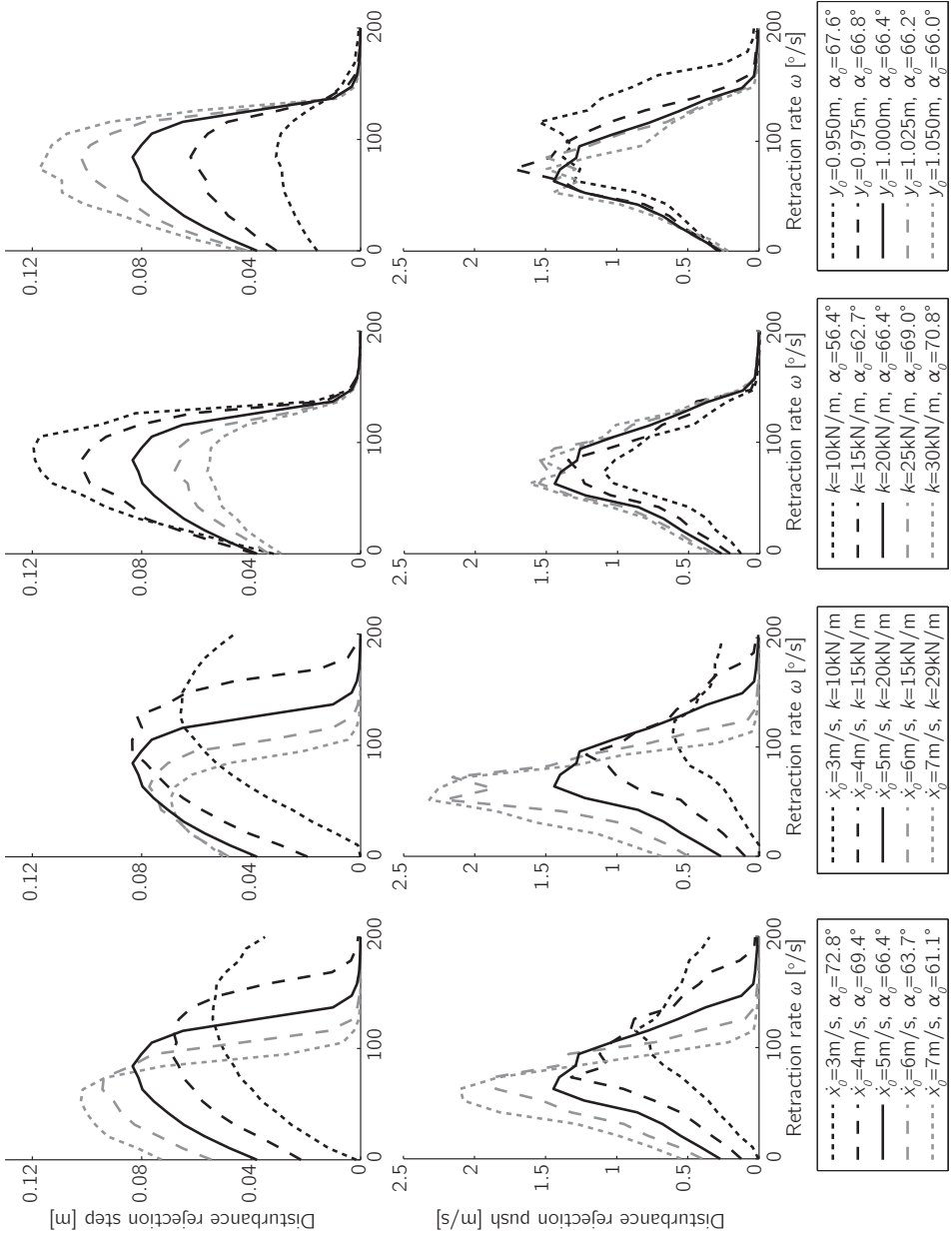


Figure 5.5: The effect of parameter variations on the relationship between disturbance rejection and retraction rate. The top row shows the disturbance rejection for a step disturbance and the bottom row for a push disturbance. Each column shows one parameter pair variation. Only parameter pair variations that include a change in the horizontal velocity (two left columns) affect the retraction rate for which the disturbance rejection is maximal.

and the push disturbance in a change of the horizontal velocity,

$$y_0 = y_0^*, \quad (5.8)$$

$$\dot{x}_0 = \dot{x}_0^* + d_{push}. \quad (5.9)$$

Figure 5.3 shows the maximal disturbance as a function of the retraction rate for both disturbances in the positive and negative directions. As predicted by the Floquet multipliers, all four graphs show that retraction rates above 113 °/s do not permit recovery from disturbances. However, there are no other shared trends among the graphs. The maximal disturbance does not clearly indicate a retraction rate for optimal disturbance rejection. This is partly due to the fact that the maximal disturbance is sometimes determined by artifacts of the model. For example, the maximal step-up disturbance is, for a large range of retraction rates, equal to the amount of ground clearance at the apex.

5.3.3 Multiple disturbances

The maximal disturbance tests did not give a clear indication on which retraction rate is optimal. To gain insight about the optimal retraction rate for disturbance rejection, we consider how the model reacts to multiple disturbances in succession. For this, we use the disturbance rejection measure as defined by Hobbelen and Wisse (2007a). They quantified the disturbance rejection as the maximal variance of a Gaussian white noise sequence that, when applied as successive step or push disturbances, causes the model to fall exactly four times in an 80 step trial. This disturbance rejection measure is noisy, due to the random disturbances it uses to test the disturbance rejection. To decrease the noise, the measure is calculated 100 times and averaged. Note that this measure is very computationally intensive; it takes about one hour to calculate the disturbance rejection for one parameter set. Therefore, the disturbance rejection is determined for a limited number of retraction rates in the range of interest.

Figure 5.4 gives the disturbance rejection for a range of retraction rates for step and push disturbances. For both types of disturbances, the disturbance rejection is improved by swing-leg retraction. The disturbance rejection is optimal at a retraction rate of about 85 °/s for the step disturbances and about 70 °/s for the push disturbances. Around these optimal retraction rates the disturbance rejection is relatively constant for a range of about 20 °/s, so it is possible to select a retraction rate such that the disturbance rejection is high for both step and push disturbances.

It should be noted that the retraction rates for the optimal disturbance rejection are not close to the retraction rate for the optimal stability determined in Section 5.3.1. This shows that stability and disturbance rejection are not interchangeable

quantities. This agrees with the results of Hobbelen and Wisse (2007a), who showed similar discrepancies between stability and disturbance rejection in walking models.

5.3.4 Parameter variations

We showed the relation between the retraction rate and the disturbance rejection for a single parameter set. In this section, we test the effect of parameter variations. There are 7 fixed parameters in the model used in this study (see Table 5.1). Three of these parameters, mass, gravitational constant and leg length, can be used to normalize the system and will therefore have only a trivial scaling effect on the relation between disturbance rejection and retraction rate. This leaves four parameters to vary: leg stiffness k , angle-of-attack α_0 , apex height y_0 and horizontal velocity \dot{x}_0 . It is not possible to vary these parameters independently, because the model only has limit cycles for certain combinations of parameter values. Therefore, we vary these parameters in pairs, setting one parameter to a desired value and adjusting the other parameter such that there is a limit cycle.

The results of the parameter variations are shown in Figure 5.5. All the parameter variations have an effect on the disturbance rejection. However, in the context of this chapter not all the changes in the disturbance rejection are interesting, because we are only interested in how optimal retraction rates, as measured by the maxima of the disturbance rejection curves, change due to parameter variations. Only parameter variations that include varying the horizontal velocity have an effect on the optimal retraction rate. Based on this we can conclude that the optimal retraction rate is only dependent on the horizontal velocity. The swing-leg retraction rate for maximal disturbance rejection decreases with increasing horizontal velocity. For a horizontal velocity of 3 m/s the optimal retraction is about 130 °/s and this decreases to 50 °/s for a horizontal velocity of 7 m/s.

5.4 Other Benefits

In the previous section, we showed how the disturbance rejection is affected by the retraction rate. In this section, we look how the other benefits of swing-leg retraction are affected by the retraction rate. There are three benefits of swing-leg retraction besides improved disturbance rejection: reduced impact losses, reduced chance of slipping, and a reduction of damaging impact forces. These three benefits are all due to the fact that swing-leg retraction reduces the relative speed of the foot with respect to the ground at the moment of touchdown. In this section, we first discuss the effect of the retraction rate on the relative foot speed. Next, we discuss how the relative foot speed relates to the three benefits.

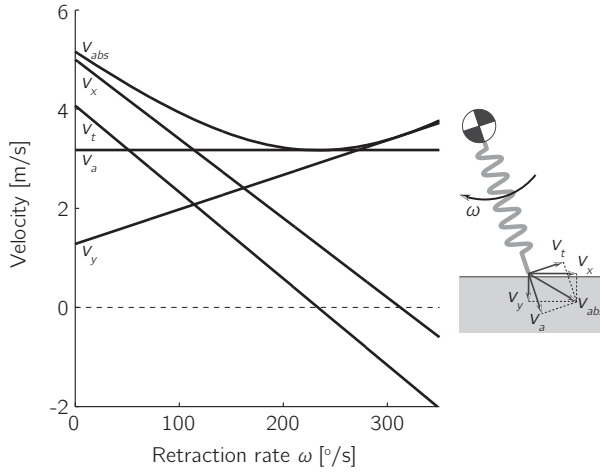


Figure 5.6: The effect of swing-leg retraction on the speed of the foot just before contact. The absolute, horizontal, vertical, tangential, and axial speeds are shown. The insert figure shows how these speeds are defined. The angle-of-attack, leg length, apex height, and horizontal apex velocity used this graph are given in Table 5.1.

5.4.1 Foot speed

The speed of the foot can be expressed in multiple ways. For the discussion in this section, the following speeds are important: the absolute v_{abs} , horizontal v_x , vertical v_y , tangential v_t , and axial v_a speed (see Figure 5.6 for definitions). Swing-leg retraction increases the vertical speed and decreases both the horizontal and tangential speed. The absolute speed decreases with swing-leg retraction for low retraction rates and increases again for higher retraction rates. The minimum absolute speed is found at the retraction rate for which the tangential speed is zero. At this retraction rate, the absolute speed equals the axial velocity, which is not affected by swing-leg retraction. Note that this retraction rate is lower than the retraction rate for which the horizontal speed is zero, which is known as ground speed matching.

5.4.2 Impact losses

The SLIP model used in this study does not have impact losses, because its leg has no inertia or unsprung foot mass. However, we can reason on how the impact losses of a model with leg inertia and foot mass would be affected by the speed of the foot at touchdown. For this we assume that the leg consists of a distributed mass m with inertia J_{leg} , which is connected to a foot with a point mass m_{foot} by a massless spring. We also assume that the impact is an instantaneous collision and that body

parts, other than the leg that touches down, have no effect on the impact losses. The energy loss due to the impact of the foot mass $E_{loss,foot}$ is a function of the absolute foot speed v_{abs} and the foot mass m_{foot} ,

$$E_{loss,foot} = 1/2 m_{foot} v_{abs}^2. \quad (5.10)$$

The energy loss due to the leg inertia $E_{loss,leg}$ depends on the tangential speed v_t and the mass properties of the leg,

$$E_{loss,leg} = \frac{J_{leg} m}{2(mL_0^2 + J_{leg})} v_t^2. \quad (5.11)$$

The total energy loss $E_{loss,foot} + E_{loss,leg}$ is minimal if both the tangential and the absolute speed are minimal in magnitude. In the previous section, we saw that the magnitude of both these velocities is minimal at the retraction rate at which the tangential foot speed is zero. Based on this we can conclude that swing-leg retraction can decrease impact losses and that the optimal retraction rate, for which the impact losses are minimal, is at 233 °/s at which the tangential foot speed is zero.

5.4.3 Slipping

Slipping of the foot at touchdown is a common problem for running and hopping robots (Raibert, 1986). Slipping occurs at impact when the horizontal impact impulse is too high compared to the vertical impact impulse. The horizontal impulse caused by the foot mass $I_{x,foot}$ is given by,

$$I_{x,foot} = m_{foot} v_x. \quad (5.12)$$

The horizontal impulse caused by the leg inertia $I_{x,leg}$ is function of the leg mass m and the leg inertia J_{leg} ,

$$I_{x,leg} = \frac{J_{leg} m}{mL_0^2 + J_{leg}} \sin(\alpha_0) v_t. \quad (5.13)$$

If the horizontal impulse is zero then the robot will not slip, no matter what the vertical impulse is. The horizontal impulse caused by the foot mass is zero if the horizontal foot speed v_x is zero, while the horizontal impulse caused by the leg inertia is zero for zero tangential foot speed v_t . The combined horizontal impulse $I_{x,foot} + I_{x,leg}$ is zero for a retraction rate between the retraction rate of zero tangential foot speed and the retraction rate of zero horizontal foot speed. The exact optimal retraction rate depends on the foot mass and leg inertia.

5.4.4 Impact forces

High impact forces can cause damage to a running robot. Swing-leg retraction might decrease these damaging impact forces. We assume that the impact is an instantaneous collision, which does not have finite impact forces. Therefore, we instead look at the impact impulses and assume that these are proportional to the impact forces if the collision were to take place over non-zero time. The impact impulse in the axial direction I_a is only caused by the unsprung foot mass and is given by,

$$I_a = m_{foot} v_a. \quad (5.14)$$

The impact impulse in the tangential direction I_t is more complex as it is caused by the combination of the impact of the foot and the impact of the leg,

$$I_t = \left[\frac{J_{leg} m}{m L_0^2 + J_{leg}} + m_{foot} \right] v_t. \quad (5.15)$$

Swing-leg retraction only affects the impact impulse in the tangential direction, as the leg retraction does not influence the axial foot speed. The absolute impulse $\sqrt{I_a^2 + I_t^2}$ is minimal as the impulse in the tangential direction is zero, which is at $233^\circ/\text{s}$ at which the tangential foot speed is zero. This optimal retraction for minimal impact impulse is the same as the optimal retraction rate for minimal impact losses.

5.5 Discussion

5.5.1 Optimal retraction rates

In the previous two sections, we have shown that swing-leg retraction can improve the disturbance rejection as well as decrease the impact losses, the likelihood of slipping, and impact forces. However, the optimal retraction rates for these benefits can be different. Figure 5.7 shows the optimal retraction rate as a function of horizontal velocity. For low horizontal velocities, around 3 m/s, the optimal retraction rates are almost equal. But at higher horizontal velocities, the optimal retraction rates diverge. The optimal retraction rate for the disturbance rejection decreases for increasing horizontal velocity, whereas the optimal retraction rate for impact losses, slipping, and impact forces increases with increasing horizontal velocity. At higher horizontal velocities, the optimal retraction rate for impact losses, slipping, and impact forces is so high that this retraction rate would destabilize the model.

5.5.2 Implications for running robots

The results of this chapter are applicable to running robots with a wide variety of control schemes. For running robots that use swing-leg retraction as a complete

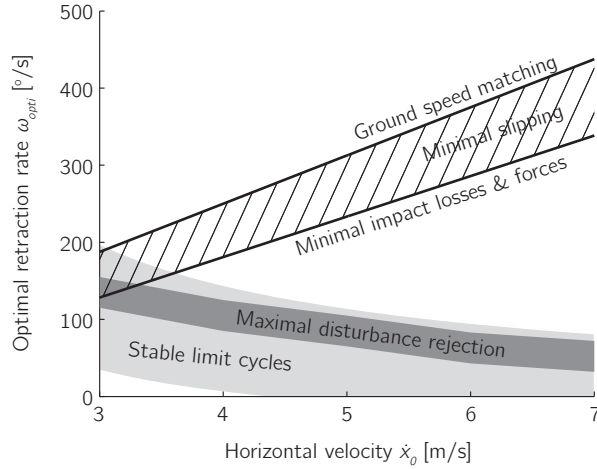


Figure 5.7: The optimal retraction rates for maximal disturbance rejection (dark gray area), for minimal impact losses and forces (solid line), and for minimal slipping (striped area). The light gray area indicates which retraction rates result in stable limit cycles.

angle-of-attack controller, the results indicate that only the range of stable retraction rates can be used. For retraction rates outside this range, the robot will fall in response to the smallest disturbance. Within the small range of retraction rates, the retraction rate is, in general, a tradeoff between maximal disturbance rejection and minimal impact losses, slipping likelihood and impact forces.

However, it is also possible to implement swing-leg retraction in conjunction with other angle-of-attack controllers. For example, Raibert's foot placement strategy could be used to determine the nominal angle-of-attack based on known disturbances, while swing-leg retraction can be used to rotate the leg backwards about this position to reduce the effect of small unknown disturbances and measurement errors. These combined controllers can be used to improve the disturbance rejection even more. The combined controllers can also be used in a different way, where swing-leg retraction is used to reduce the impact losses and forces and the likelihood of slipping, while the other controller provides the stability. For this last method, high retraction rates can be used that reduce impact losses and forces and likelihood of slipping to their minimum, because the other controller can compensate for the instability caused by these high retraction rates.

5.5.3 Implementation of swing-leg retraction on running robots

To implement swing-leg retraction on a running robot, the robot needs to be able to measure three quantities during the flight phase: the absolute angle, the angular rate of the leg, and the apex time. The apex time and the leg angle are needed to start the retraction at the correct moment with the desired leg angle. The angular rate is needed to control the leg to the desired retraction rate. The absolute angle and angular rate of the leg are often measured using a combination of accelerometers and gyroscopes. To determine the time of apex is more complicated. It can be done by integrating the vertical acceleration starting from liftoff or by using a contactless distances sensor, for example a laser rangefinder. Another option, for which the apex time is not needed, is to start the timer for the retraction on an easier to measure event, like the liftoff. However, starting the timer on a different event might have negative consequences on the stability and disturbance rejection. Preliminary results showed that starting the timer at liftoff significantly reduced stability, but more research is needed on this topic.

5.6 Conclusions

In this chapter, we presented a simulation study on swing-leg retraction. We showed how the benefits of swing-leg retraction depend on the retraction rate. Based on these results we conclude that:

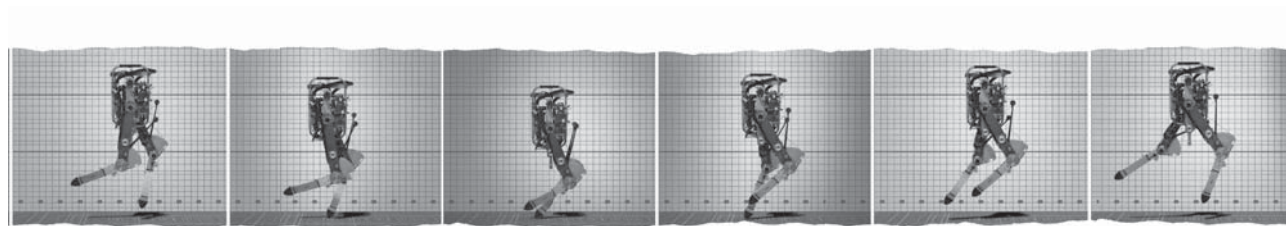
- Swing-leg retraction can improve the disturbance rejection and reduce impact energy loss, likelihood of slipping, and impact forces.
- The optimal swing-leg retraction rate for maximal disturbance rejection only depends on the horizontal velocity and does not depend on any other parameter, like leg stiffness, angle-of-attack and apex height.
- The swing-leg retraction rates for optimal stability and maximal disturbance rejection decrease with increasing horizontal velocity.
- The swing-leg retraction rates for minimal impact energy loss, slipping likelihood, and damaging forces increases with increasing horizontal velocity.
- For moderate and high running speeds, there is an inherent tradeoff between improving disturbance rejection and decreasing impact losses, impact forces, and slipping likelihood. This tradeoff becomes more severe as horizontal velocity increases.

Acknowledgements

J.G.D. Karssen and M. Wisse are funded by the Dutch Technology Foundation STW and are with the Delft Biorobotics Laboratory, Delft University of Technology. M. Haberland and S. Kim are funded by the Defense Advanced Research Project Agency and are with the Biomimetic Robotics Laboratory, Massachusetts Institute of Technology.

The effects of swing-leg retraction on running performance: analysis, simulation, and experiment

J.G.Daniël Karssen, Matt Haberland, Martijn Wisse, and Sangbae Kim,
Submitted to *The International Journal of Robotics Research*.



Abstract

Using simple running models, researchers have argued that swing-leg retraction can reduce energetic losses, impact forces, the risk of slipping, and the adverse effects of disturbances. In this chapter, we investigate whether these effects occur in more realistic running systems by comparing the trends for simple models with simulated results from a realistic model and validating the realistic model against a physical running robot. The results of this study show that swing-leg retraction can increase stability with respect to infinitesimal perturbations and large disturbance rejection measures such as settling time after a disturbance and mean steps to fall under random disturbances, and can improve these measures simultaneously to a limited extent. Alternatively, swing-leg retraction can be used to decrease touchdown forces, increase footing stability, and decrease impact energy losses simultaneously. Surprisingly, swing-leg retraction had a negligible effect on overall energetic efficiency. However, these trends appear to be strongly model dependent, suggesting that while simplified models may be useful to provide intuitive explanations for observed behavior, caution must be exercised when attempting to use simple models to predict complex phenomena.

6.1 Introduction

Legged locomotion is an important topic in robotics because legged robots promise improved mobility in unstructured environments (Kim et al., 2006; Raibert et al., 2008; Saranli et al., 2001). Intuition regarding the sensitivities of robot performance to hardware and controller parameters is essential for the design of effective legged mobility systems. In addition, knowledge of these sensitivities can give insight into human locomotion, which is useful for the design of better prostheses and orthoses. The goal of this chapter is to develop intuition about the inherent effects of a particular control parameter, swing-leg retraction rate, on several running performance metrics.

Swing-leg retraction (SLR) is a behavior exhibited by humans and animals in which the airborne front leg rotates rearward prior to touchdown (Müller and Blickhan, 2010). It is hypothesized that SLR enhances performance of biological systems (Blum et al., 2010), and that we might use SLR to improve the performance of legged robots, such as the Phides robot shown in Figure 6.1. Use of SLR to improve controller performance is attractive, because it is a conceptually simple extension to any foot

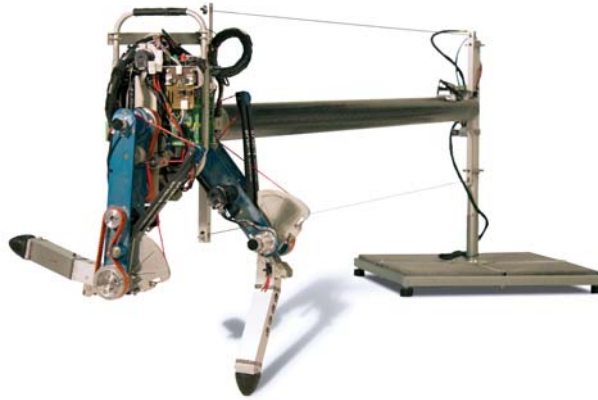


Figure 6.1: Running robot 'Phides'. This robot consists of a torso and two kneed legs with small, spherical feet. The robot is attached to a boom with a parallelogram mechanism to achieve planar behavior. The two hip joints are directly actuated by DC-motors in the torso. The two knee joints are actuated by DC-motors with a spring in series (torsion bar inside the knee shaft) as well as a spring in parallel (leaf spring with pulley mechanism).

placement controller, such as the constant angle-of-attack controller (Seyfarth and Geyer, 2002) and the neutral point controller (Raibert et al., 1989).

The effect of swing-leg retraction on limit cycle walking (Hobbelen and Wisse, 2007b) is relatively well studied and has been shown to improve energy efficiency, small disturbance stability, and large disturbance rejection (Asano, 2009; Hobbelen and Wisse, 2008; Wisse et al., 2006). These results are illuminating for walking systems, but fundamental differences between walking and running gaits preclude the direct application of these results to running systems. Certain aspects of swing-leg retraction have been studied for running systems. For instance, Blum et al. (2010); Ernst et al. (2009); Seyfarth and Geyer (2002); Seyfarth et al. (2003) all agree that swing-leg retraction can improve the stability of the frequently used Spring Loaded Inverted Pendulum (SLIP) model of running. Daley and Usherwood (2010) and Karssen et al. (2011) (Chapter 5) conclude that for simple models, low retraction rates yield better stability, but high retraction rates minimize peak forces. Raibert (1986) and Haberland et al. (2011) suggest that swing-leg retraction can improve energetic efficiency. However, the existing literature leaves two important open questions:

- Do simple models accurately predict the effects of SLR on a physical running robot?
- Given the effects of SLR on different performance metrics, how should a controller's retraction rate be chosen?

The present chapter provides answers to these questions through a comprehensive study of the effects of SLR on running performance using simple models, a realistic model, and physical hardware. The remainder of this chapter is organized as follows: Section 6.2 introduces the simulation models and experimental hardware used in this study. Section 6.3 and Section 6.4 present the effects of the retraction rate on the impact losses and energetic efficiency of the models, respectively. Section 6.5 discusses the effect of the retraction rate on the impact impulse and footing stability. Section 6.6 and Section 6.7 study the effect of the retraction rate on the stability and disturbance rejection. The chapter ends with a discussion, including model validation against the physical robot, in Section 6.8 and conclusions in Section 6.9.

6.2 Models and Experimental Platform

In this study, we investigate the effect of swing-leg retraction using a simple running simulation model (Figure 6.2), a realistic simulation model (Figure 6.4), and a running robot (Figure 6.1). The Spring Loaded Inverted Pendulum (SLIP) model is used as the simple simulation model. The low complexity of this model results in short computational times, which allows for extensive testing. However, the SLIP model does not capture all the relevant dynamics. Aspects related to energy loss and replacement are not captured because the model is energetically conservative. To capture more of the relevant dynamics we use a more realistic simulation model, which is a full rigid body model of a running robot. The validity of this model is checked by comparing its gait and disturbance response to those of a physical running robot. The next sections give a detailed description of the simulation models and the robot.

To fairly compare the results of the simulation models and the robot, we match model parameters to the extent permitted by their structures. We normalize all parameters and results with the total mass M , leg length L_0 and gravitational acceleration g to get dimensionless numbers. The swing-leg retraction rate ω (in rad/s) is normalized as:

$$\bar{\omega} = \omega \sqrt{\frac{L_0}{g}}. \quad (6.1)$$

Unless otherwise noted, the models and the robot run at normalized average speed \dot{x}_{avg} of 0.42 (Froude number of $0.18 = \dot{x}_{avg}^2$). This is a slow speed for a running gait, but it is near the maximal speed of the robot.

6.2.1 SLIP model

Simulation

The Spring Loaded Inverted Pendulum (SLIP) is a one-leg hopper model widely used for analyzing running dynamics (Blickhan, 1989; Ghigliazza et al., 2005; Poulakakis and Grizzle, 2009a; Schwind and Koditschek, 1997; Seyfarth and Geyer, 2002). This model consists of a point mass body on a massless spring leg (Figure 6.2). Despite its simplicity, it has been shown to be a reliable model for certain aspects of human and robot running, such as the center-of-mass trajectories (Blickhan and Full, 1993; Full and Koditschek, 1999).

The SLIP model has two distinct phases of motion: a flight phase in which the leg is not in contact with the ground, and a stance phase during which the leg is in contact with the ground. During the flight phase, the point mass follows a ballistic trajectory, as it is influenced by gravity alone. The resulting equation of motion is given by

$$\begin{bmatrix} \ddot{x} \\ \ddot{y} \end{bmatrix} = \begin{bmatrix} 0 \\ -g \end{bmatrix}, \quad (6.2)$$

where \ddot{x} and \ddot{y} are the horizontal and vertical accelerations of the point mass and g is the gravitational acceleration. The flight phase ends and the stance phase begins at touchdown, which occurs when the massless point foot at the end of the leg spring contacts the ground, that is, when the body height y , leg rest length L_0 , and angle of the leg α_0 , measured positive clockwise from horizontal, satisfy the condition

$$y - L_0 \sin(\alpha_0) = 0. \quad (6.3)$$

There are no impulsive dynamics at touchdown, as the foot and leg are massless and compliant. During stance, the point foot remains fixed on the ground, and thus the leg spring compresses and extends as the body mass moves, producing a force acting along the axis of the leg

$$F_s = k\Delta L, \quad (6.4)$$

where k is a constant leg stiffness and ΔL is the compression of the leg. The resulting equation of motion is given by

$$m \begin{bmatrix} \ddot{x} \\ \ddot{y} \end{bmatrix} = \begin{bmatrix} -\cos \alpha \\ \sin \alpha \end{bmatrix} F_s + \begin{bmatrix} 0 \\ -mg \end{bmatrix}, \quad (6.5)$$

where m is the mass of the point mass and α is the leg angle. The stance phase ends and the flight phase begins at liftoff, when the spring leg reaches its rest length L_0 .

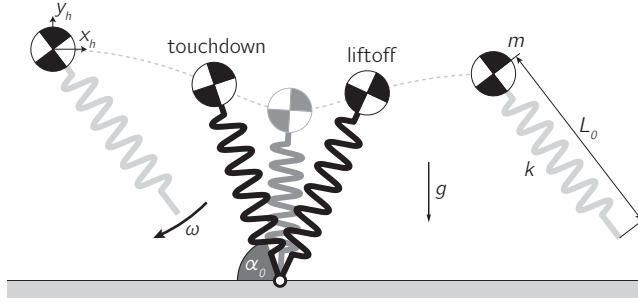


Figure 6.2: SLIP-model with swing-leg retraction. The model consists of a point mass body and a massless spring leg. At liftoff, the leg jumps instantaneously to angle α_r with respect to the ground and begins rotating at rate ω . The leg angle at touchdown α_0 depends on the time between liftoff and touchdown.

The parameters of the SLIP model are chosen to match the robot Phides, with $m = 13.11\text{kg}$, $L_0 = 0.58\text{m}$, $g = 9.81\text{m/s}^2$, and $k = 5.06\text{kN/m}$, which are normalized $\bar{m} = 1$, $\bar{L}_0 = 1$, $\bar{g} = 1$, and $\bar{k} = 22.8$.

Control of SLIP model

The SLIP model is controlled only by changing the angle of the spring leg during flight. Because the leg is massless, this requires no energy and does not affect the flight dynamics. However, this changes the angle α_0 , the time, and thus the velocity, at which the leg touches the ground, which strongly influences the behavior during the stance phase.

Seyfarth et al. (2003) proposed a simple swing-leg retraction controller to stabilize the SLIP model in response to disturbances: at the instant of apex, the leg is set to angle α_r , and is subsequently retracted at retraction rate ω until the foot touches the ground, resulting in touchdown angle-of-attack α_0 . This controller, with properly chosen α_r and positive ω , caused the trajectory of the SLIP model to approach a limit cycle, or periodic motion, from a much wider range of initial conditions than any fixed angle controller, in which $\omega = 0$. This makes intuitive sense: if the apex is lower than it must be for a particular limit cycle, then the foot will touch down early, the angle-of-attack will be shallower, and thus the robot will experience greater positive vertical impulse during stance, raising the height of the next apex. The opposite applies when the apex is higher than it must be for a particular limit cycle, and this automatic apex-height correction results in convergence to a limit cycle.

The swing-leg control strategy above may seem to be a feedforward strategy, but

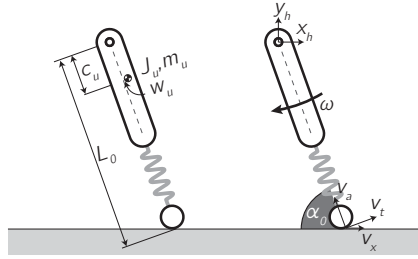


Figure 6.3: Prismatic Leg model, an extension of the SLIP model with distributed leg mass and a point mass foot.

in reality, the robot must sense the apex event to initiate swing-leg retraction. In practice with the Phides robot, we found that apex is actually quite difficult to sense reliably due to the limited resolution of the sensors. So in this chapter, we set the initial leg angle α_r and begin retraction at liftoff instead of at apex because liftoff can be measured with a simple contact switch. Section 6.8 discusses the effect of this change in greater detail.

The start leg angle α_r is chosen to produce the same limit cycle, with a normalized horizontal speed of 0.42 and a normalized apex height of 1.04, regardless of the retraction rate.

Prismatic Leg Impact Model

Because the SLIP model is energetically conservative, we use an extension of the SLIP model shown in Figure 6.3 to study the effects of swing-leg retraction on the impact event. In the simple prismatic leg model, the mass of the SLIP is distributed to form the upper segment of the leg, and a point mass is added to the foot. The impact equations are derived according to conservation of angular momentum assuming a perfectly inelastic collision, that is, the foot sticks upon landing. Note that these equations are not used in the dynamic simulation of the SLIP model; they are only used in postprocessing to study the impact dynamics of a SLIP-like model with leg mass.

6.2.2 Realistic model

Simulation

The realistic simulation model is designed to closely resemble the physical running robot used in this study (Section 6.2.3). The model, shown in Figure 6.4, is 2-dimensional (planar) and consists of five rigid bodies with distributed mass: a torso,

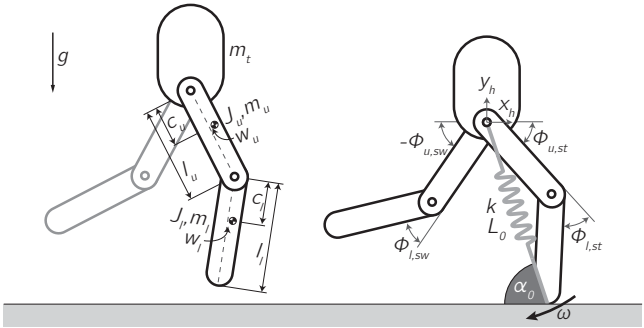


Figure 6.4: 2-dimensional realistic running model that consists of five rigid bodies. The left figure shows the robot during the flight phase and labels model parameters, the values of which are given in Table 6.1. The right figure shows the robot during the stance phase, during which the leg spring is active, and the 6 generalized coordinates used to describe the motion. Note that the torso orientation is not a degree-of-freedom as the rotation of the torso is fixed with respect to the world.

two upper legs, and two lower legs. The size and mass distribution of the rigid bodies are given in Table 6.1. The feet are simply points at the ends of the lower legs. For this study, we fix the rotation of the torso with respect to the world to eliminate the need to control the torso orientation. This leaves the model with 6 degrees-of-freedom: the x - and y -position of the hip, the rotations of two hip joints, and the rotations of two knee joints. Torques, limited to 21.4 Nm to represent the actuator limitations of the robot, act at all four joints.

The running motion of the realistic model has two distinct phases: a flight phase during which the robot is airborne, and a stance phase in which one foot acts as a pin joint fixed to the ground.

During the flight phase, the center-of-mass follows a ballistic trajectory, as the leg is not in contact with the ground, and the legs move under the influence of the joint torques. Note that the angular momentum of the robot is not fixed, as torques at the hip act against the torso, which is fixed against rotation.

When a foot touches the ground, the impact is modeled as an impulsive, perfectly-inelastic collision. The state after impact is calculated according to angular momentum conservation. Under certain conditions, the impulse of the ground acting on the robot is negative; that is, the floor pulls on the robot. This is common in such models (Haberland et al., 2011; McGeer, 1990a). While the negative impulse is physically unrealizable, it was found in McGeer (1990a) that this collision model predicts the state after touchdown reasonably well and is far less computationally

Table 6.1: Parameter values of the realistic model and robot. See Figure 6.4 for the parameter definitions, in which parameters are given by the property symbol with a subscript indicating the segment.

	<u>t</u> orso	<u>u</u> pper leg	<u>l</u> ower leg
Mass m [kg]	7.41	2.54	0.51
Moment of inertia J [kgm ²]	-	0.036	0.005
Length l [m]	-	0.3	0.3
Vertical offset CoM c [m]	-	0.183	0.139
Horizontal offset CoM w [m]	-	0	0

expensive compared to a finite friction model, which might represent the physics more faithfully.

During stance, a spring of constant stiffness 5.06 kN/m (dimensionless stiffness of 22.8) produces a force linearly proportional to the distance between the stance foot and the hip, storing and releasing energy exactly as in the SLIP model. The knee is equipped with an end stop at 0.52 rad that prevents the leg from extending further than the rest length of the leg spring of 0.58 m. This knee end stop is modeled as a unidirectional spring-damper, that is, a shock absorber. As in flight, joint torques control the robot during stance.

Liftoff occurs and flight resumes when the normal force between the foot and the ground falls to zero. There is no impulsive collision involved, so there is no instantaneous change in state at liftoff.

The equations of motion and impact equations were derived using the TMT method (van der Linde and Schwab, 2011) and independently verified using Lagrangian mechanics and conservation of angular momentum. The resulting equations are far too long to be included in this chapter. Integration is performed using MATLAB's `ode45()` function with absolute and relative tolerances of 10^{-5} .

Control of Realistic model

The swing-leg retraction rate is defined as the angular velocity of the “virtual leg”, that is, the line connecting the hip and the foot. This swing-leg retraction is not to be confused with swing-leg contraction, which is the time derivative of the length of

the virtual leg. Note that in this study, the swing-leg contraction rate at touchdown is set to zero for two reasons:

- Although both swing-leg retraction and swing-leg contraction is required for perfect ground speed matching (and zero impact loss), humans tend to exhibit much more swing-leg retraction than swing-leg contraction (Blum et al., 2010).
- The physical Phides robot does not permit swing-leg contraction when the leg spring is engaged shortly before touchdown because the motors cannot backdrive the stiff leg spring.

During the flight phase, all joints are PD-controlled to follow quadratic spline trajectories. These trajectories are chosen such that they start at the joint state at the moment of liftoff and go to a manually tuned desired state after a preset time, while minimizing the maximal acceleration magnitude. During the last part of the flight phase, the swing leg knee joint is locked and the hip joint rotates with a constant angular rate ω , resulting in overall swing-leg retraction rate ω .

During the stance phase, the hip and knee joint of the swing leg follow quadratic spline trajectories as during the flight phase. No torque is applied to the hip of the stance leg during the stance phase. Also, the stance knee actuator does not apply any torque during the first part of the stance phase from touchdown to maximal knee compression. However, the stance knee pushes off during the second half of the stance phase, from maximal knee compression to liftoff. This push off is used to control the energy level of the system. The push-off torque is chosen such that energy supplied by the push off is equal to the difference between the system energy at maximal knee compression and a desired energy level.

Simplified Impact Equations

In addition to the realistic model, we use a simplification of the realistic model to study the effects of swing-leg retraction on the impact event (Figure 6.5). In the simple kneed leg model, the touchdown leg is entirely preserved, but the other leg and the torso are lumped into a point mass at the hip. The impact equations are derived according to conservation of angular momentum, assuming the foot sticks upon landing. These equations are not used in the dynamic simulation of the realistic model; they are only used in postprocessing to illuminate whether the particular state of the second leg and torso have a significant effect on the impact dynamics. If not, the simplified equations may be used to simplify study of the impact dynamics.

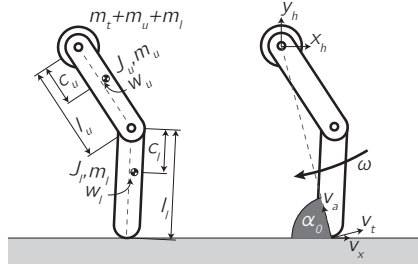


Figure 6.5: Kneaded leg model, a simplification of the realistic model in which the mass of the opposing leg and the torso are lumped into a point mass at the hip.

6.2.3 Physical Robot

Hardware

In this study, we use a running robot called 'Phides', shown in Figure 6.1. See Chapter 4 for a detailed description of this robot. Phides consists of a torso and two kneed legs with small, spherical feet. The robot is attached to a boom to achieve planar behavior. The boom has a parallelogram mechanism that keeps the hip axis of the robot parallel with the ground. For this study, the rotation of the torso is fixed with respect to the boom to eliminate the need to control the torso angle. An overview of the robot parameters is given in Table 6.1.

The two hip joints and two knee joints, are actuated with electric DC-motors (Maxon RE35 30V) with a gear ratio of 1:55. The hip joint actuators are rigidly connected to the joints, whereas the knee joint actuators are connected through a torsion bar spring in the knee joint (215 Nm/rad) to form a series elastic actuation (Pratt and Williamson, 1995). In parallel with the series elastic actuation, the knee joints use a leaf spring in series with a nonlinear transmission to store and release energy during the stance phase. The nonlinearity of the transmission creates an effective prismatic (i.e. telescoping, as opposed to rotary) spring of constant linear stiffness between the foot and the hip, as in the SLIP model. An actuated latching mechanism engages this effective parallel spring at touchdown for energy storage during stance and disconnects the spring at liftoff to permit free joint rotation during flight. The knee joints are equipped with an end stop that prevents the knees from extending beyond the rest length of the parallel spring.

The hardware is equipped with digital incremental encoders on all the joints of the robot and the boom. From the measured angle and angular velocity of all joints, the encoders effectively measure the full state of the robot. The resolution of the encoders is $6 \cdot 10^{-5}$ rad for the hip joints and $2 \cdot 10^{-4}$ rad for the knee joints and

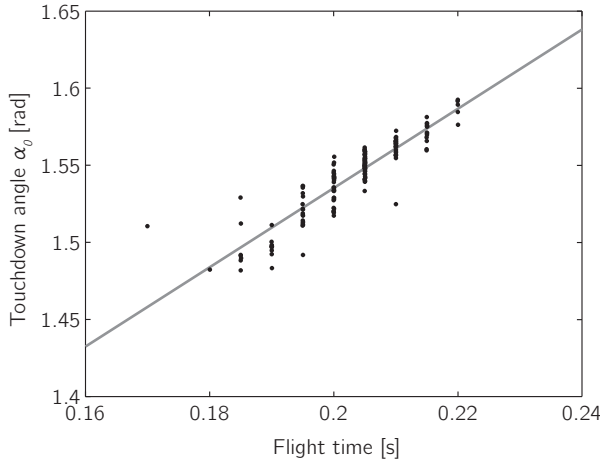


Figure 6.6: The touchdown angle α_0 versus the flight time. Points are measurements of 158 steps of the robot. The effective retraction rate is determined with a least-squares linear fit (solid line) through the measurement data.

boom degrees-of-freedom. The robot has contact sensors in each of the feet to sense ground contact.

Control of Robot

The controller of the robot is similar to the controller of the realistic model. However, communication delays and limited sensor accuracy on the robot limit the gains of the PD-controllers, limiting the accuracy to which the quadratic spline joint trajectories are tracked. This inaccuracy makes it difficult to set the swing-leg retraction rate to a desired level; instead we measure the touchdown angle and flight time over a large number of steps and consider the effective retraction rate to be the slope of a linear least-squares fit through the data, as illustrated in Figure 6.6.

The robot uses a different push-off strategy than the realistic simulation model because the knee actuators are not capable of injecting sufficient energy during the second half of the stance phase alone. To deliver more energy into the system, the knee actuator tensions the parallel spring before touchdown, and applies a constant, maximal torque on the knee in the same direction as the knee velocity during the first half of stance.

This finishes the description of the two models and robot that are used in this study. Next, we study the effect of the swing-leg retraction rate on the impact losses, energetic efficiency, impact impulse, footing stability, and disturbance rejection of

these models. We start with the effect of the swing-leg retraction rate on the impact losses in the next section.

6.3 Impact Losses

Swing-leg retraction rate affects the energy usage of running systems. The most obvious reason is that the speed of the foot, and thus the energy loss as the foot impacts the ground, is greatly influenced by the rate of swing-leg retraction. While there are other sources of losses in running, we will first investigate the effect of swing-leg retraction on the impact losses of the realistic model of Section 6.2.2 and the two simplified impacts models of Sections 6.2.1 and 6.2.2 to test our intuition regarding the most apparent link between swing-leg retraction and efficiency. We present the results from both simplified and realistic models to assess whether the trends of the simplified models are shared by the realistic model.

6.3.1 Methods

Impact losses are determined by taking the difference between the kinetic energy of the system immediately before and immediately after the instant of touchdown. The impact losses of the realistic model are determined while running under the hand-tuned controller of Section 6.2.3. All elements of the realistic model touchdown states except for retraction rate are mapped onto the prismatic and kneed leg models. To investigate the sensitivity of impact loss with respect to typical state variations, impact loss is calculated for the simplified models in all of these touchdown states for a variety of retraction rates. In order to investigate the sensitivity of the results for the prismatic and kneed leg models with respect to parameter variations, impact losses are calculated for the models with $\pm 50\%$ upper leg mass.

6.3.2 Results

Prismatic Leg

We showed in Chapter 5 that there is a simple analytical relationship between running velocity, leg length, leg touchdown angle, leg retraction rate, and energy loss of a prismatic leg. The energy loss of the prismatic leg model of Section 6.2.1 upon impulsive, perfectly-inelastic collision between the foot and the ground is

$$E_{loss} = \frac{1}{2} m_l v_a^2 + \frac{1}{2} \left(m_l + \frac{J_u m_u}{J_u + m_u (L_0 - c_u)^2} \right) v_t^2, \quad (6.6)$$

in which the meaning of all symbols is illustrated in Figure 6.3. The symbols v_a and v_t represent the axial and tangential foot speed, respectively, and are functions of the hip velocity and the retraction rate:

$$\begin{aligned} v_a &= -\dot{x}_h \cos \alpha_0 + \dot{y}_h \sin \alpha_0, \\ v_t &= \dot{x}_h \sin \alpha_0 + \dot{y}_h \cos \alpha_0 - L_0 \omega. \end{aligned} \quad (6.7)$$

Because there is control over swing-leg retraction ω , and thus the tangential foot speed v_t , but no control over swing-leg contraction, or axial foot speed v_a , the energy loss is minimized when $v_t = 0$. Note that this is not, in general, the same as zeroing the horizontal component of the relative velocity between the foot and the ground, v_x . Figure 6.7 shows the effect of the swing-leg retraction rate on impact loss of the prismatic leg for a range of typical touchdown states and varying upper leg mass. The curves agree very closely; all have a minimum at the retraction rate that zeros the foot tangential speed.

Kneed Leg

For a kneed leg, the impact equations are more complicated than for the prismatic leg. We omit the symbolic expression because of its length and difficulty of interpretation; we could not find a simple relationship to describe the location of the minimum as for the prismatic leg. The graphical representation of Figure 6.7 shows that the location of minimal impact loss for the kneed leg is very different from the normalized retraction rate for zero foot tangential speed. Also, the minimum impact loss is achieved at significantly different normalized retraction rates depending on the mass distribution of the leg.

Robot Simulation

The robot is simulated using the realistic model and controller described in Section 6.2.2 and the resulting energy losses for limit cycle running is measured for a range of retraction rates. The results are superposed on Figure 6.7 and show close agreement with the simplified kneed leg model.

6.3.3 Discussion

Figure 6.7 shows that variations within the characteristic range of touchdown horizontal speeds, touchdown vertical speeds, and angles-of-attack have little effect on the normalized energy loss, as indicated by the narrow bands. Also, for prismatic legs, mass distribution of the leg has little effect on the trend, as the minima of the lines for $\pm 50\%$ upper leg mass share a minimum with the band for normal robot mass parameters.

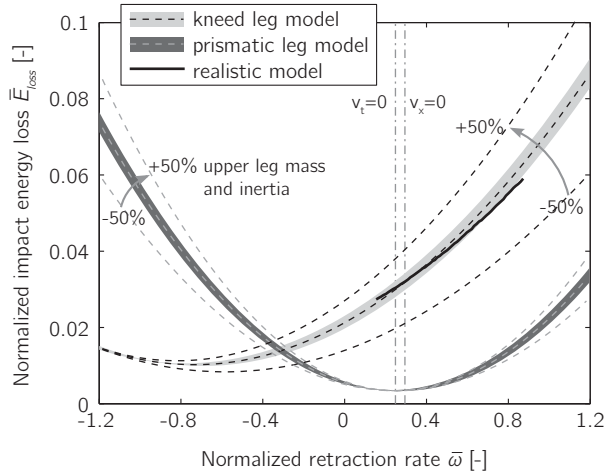


Figure 6.7: The effect of the normalized swing-leg retraction rate $\bar{\omega}$ on the normalized energy loss \bar{E}_{loss} for a prismatic leg model, knead leg model, and realistic model. For the simplified models, shaded regions indicate results for a range of touchdown conditions, including variations in instantaneous velocity and angle-of-attack, encountered at touchdown in limit cycles of the realistic model. Lines indicate the mean result for the range of touchdown conditions studied. Lines for simplified models with mass parameters of the Phides robot (+0% upper leg mass) and $\pm 50\%$ upper leg mass are also shown. Results for simulated limit cycle running of the realistic model with Phides-like parameters are represented with a thick black stroke. For reference, $\bar{E}_{loss} = 1$ would occur if the full mass of the robot translating at 3.37 m/s were to stop completely.

For knead legs, however, the minima of the curves lie at a much lower retraction rate than that of horizontal or tangential speed matching. That is, our intuition about lower impact loss stemming from reduced relative speed between the foot and the ground, or ground speed matching, does not hold for knead legs when there is no swing-leg contraction during flight. However, we can adjust our intuition by considering that the impact loss is not only due to abrupt changes in the translation of the foot or the leg segments, but also due to abrupt changes in the rotation of the leg segments. Note that immediately before touchdown, the rate of swing-leg contraction is very low (by constraint), but immediately after touchdown, there must be significant leg contraction as the knee bends. This sudden increase in leg contraction is manifested as a decrease in the angular velocity of the upper leg segment and an increase in the angular velocity of the lower leg segment. The impact losses due to these sudden jumps in angular velocity are lower if the more massive upper segment has a less positive, or even more negative, angular velocity prior to touchdown. Indeed, the minima of the impact loss curves for the knead leg models occur at much lower retraction rates than for prismatic leg models. Furthermore,

the more massive the upper leg segment the more pronounced this effect is; as upper leg mass is increased, the retraction rate at which the minimum occurs is decreased.

The curves for a kneed and prismatic leg are quite different, so we cannot consider the prismatic leg a representative simplification of a kneed leg when studying impact losses. This suggests that while the results of Haberland et al. (2011) may be valid for prismatic legged robots, they do not necessarily generalize to kneed legs as originally suspected. On the other hand, the kneed leg model agrees closely with the realistic model, indicating that the state of the second leg at impact does not significantly affect the energy loss.

6.4 Overall Energetic Efficiency

Impact loss is not the only factor in running energetic efficiency; another consideration is that the forward and rearward acceleration of the swing leg is accomplished, at least in part, by actuator work, and thus the swing-leg retraction rate is the result of a certain energy expenditure. Perhaps subtler still is that the state of the leg as it touches down sets the initial conditions for the stance phase, during which much of the work of running is done, and the ensuing dynamics are significantly affected by the initial conditions. Since impact losses are only a portion of the energy expenditure of the robot in running, it is unclear a priori whether the reduction in impact loss due to a given retraction rate leads to an overall efficiency improvement. Therefore, we consider the effect of the retraction rate on overall limit cycle energetic efficiency of the Phides robot in simulation.

6.4.1 Methods

We measure the overall energetic efficiency of the realistic model of Section 6.2.2 in limit cycle motion for a range of swing-leg retraction rates. We quantify the energy efficiency using mechanical cost of transport c_{mt} , which is the energy consumed by the actuators normalized by the robot's weight and distance travelled. The energy consumed is assumed to be the integral of the absolute mechanical power of the actuators. Thus,

$$c_{mt} = \frac{\int_0^{t_{step}} |\tau \cdot \dot{\phi}| dt}{M \cdot g \cdot x_{step}}, \quad (6.8)$$

in which t_{step} is the temporal duration of a step, x_{step} is the distance travelled in a step, τ is the vector of instantaneous joint torques, $\dot{\phi}$ is a vector of the angular velocities of the joints, M is the total robot mass, and g is gravitational acceleration.

Initially, we analyzed the effect of the retraction rate on efficiency under the particular, hand-tuned controller of Section 6.2.2. We found that swing-leg retraction

rate had only a small effect on cost of transport, which ranged from 0.64 - 0.7. To determine whether this limited effect of swing-leg retraction is particular to the hand-tuned controller or inherent to all controllers, we study the effect of the retraction rate on the maximum possible efficiency of limit cycle running. To do this, we seek the initial conditions of the robot state and control trajectories of the four actuators that yield minimal c_{mt} by means of optimization.

Optimization

General Pseudospectral Optimal Control Software (GPOPS) (Benson et al., 2006; Garg et al., 2010, 2011; Rao et al., 2010) is used to find the torque profiles and initial conditions for energetically-optimal limit cycle running under the constraints of

- limit cycle periodicity,
- specified touchdown swing-leg retraction rate,
- specified average speed of limit cycle running,
- $30^\circ(+0^\circ, -2.9^\circ)$ touchdown knee angle,
- $>30^\circ$ leg extension at all times,
- foot-ground clearance as appropriate,
- no swing-leg contraction (leg segment angular velocities match within 0.1 rad/s at touchdown),
- bounds on state and control variables to match physical robot where applicable (except a 50 Nm torque limit is used to enable higher speed running), and
- upper and lower bounds on all other state and control variables for better optimization performance.

Note that no path constraint was placed on the ground reaction forces. Thus, it is possible, indeed typical, for the foot to pull against its pivot at the ground for a short time after touchdown. While physically unrealizable, we neglect this as we neglect the pulling impulses at the touchdown collision event explained in Section 6.2.2.

For better numerical performance, the control variables in GPOPS are the time rate of change of the joint torques; GPOPS optimizes the initial joint torques along with these control profiles. For good convergence properties, the cost function must be

smooth, so the absolute value function $abs(x)$ of Equation 6.8 is approximated as $\sqrt{x^2 + \epsilon}$, where ϵ is a small positive real.

GPOPS implements a pseudospectral optimization method. Like other collocation methods, pseudospectral methods optimize state and control variables simultaneously to minimize the cost function and enforce constraints, including those imposed by the equations of motion. Accordingly, GPOPS requires an initial guess, or seed, for both control and state trajectories in each phase, i.e. stance and flight. A seed includes, for each phase, an array of time points and arrays of state and control values corresponding with each time point. Such a seed might be actual control and state trajectories from simulation, in which case the constraints imposed by the equations of motion are satisfied with the initial guess. However, we do not wish to constrain our search for energetically optimal running with any preconceived notions about running. To avoid this, we generate random state and control arrays using Matlab's `rand()` function and scale them according to the bounds placed on the state and control variables. The time arrays contain equally spaced points, but are of random duration within generous bounds. From these random seeds, GPOPS robustly converges to optimal state trajectories that satisfy the constraints and agree closely with 'propagated' state trajectories, that is, states integrated in simulation by Matlab's `ode45()` from the initial conditions and under the open loop controls provided by GPOPS. However, the problem is quite complicated and is plagued by local minima. To more closely approximate the globally optimal mechanical cost of transport for each swing-leg retraction rate, the optimization problem is repeated from many random seeds.

6.4.2 Results

Typical optimization results are presented in Figure 6.8. For each value of normalized retraction rate between -1 and +1 at 0.025 intervals, optimization is performed 10 times. That is, each point in Figure 6.8 represents a locally optimal limit cycle produced from a different random seed. While there are some scattered local optima that do not exhibit any discernible trend, most points tend to cluster densely around a lower bounding curve. From hundreds of random seeds, no limit cycles were produced with a cost of transport below this curve. Thus, we consider this curve to be a close approximation of the global minimal mechanical cost of transport as a function of swing-leg retraction rate. For limit cycle running at an average normalized speed of 1.36, the figure shows that optimal energetic efficiency is achieved with a relatively high, positive retraction rate.

However, the absolute effect of the retraction rate on the cost of transport is small, with a maximal difference of only 3% over the whole range of retraction rates. This

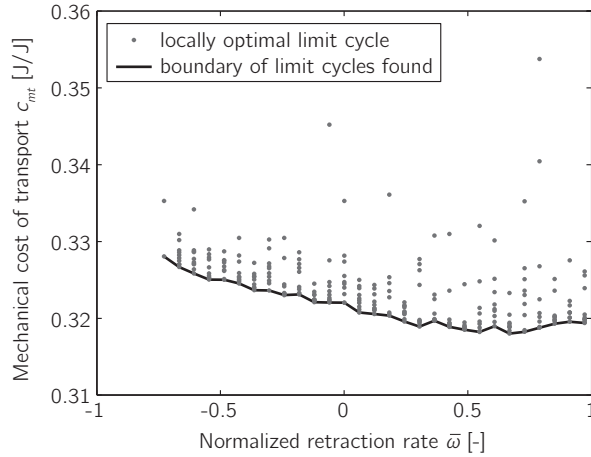


Figure 6.8: The effect of the normalized retraction rate \bar{w} on the minimal mechanical cost of transport of limit cycle running at an average normalized speed of 1.36. Each point represents a limit cycle with locally minimal mechanical cost of transport optimized from a different random initial seed. Though the initial seeds are entirely unrelated, the locally minimal mechanical cost of transport of the optimized limit cycles cluster densely about an apparent boundary believed to be representative of the globally minimal mechanical cost of transport.

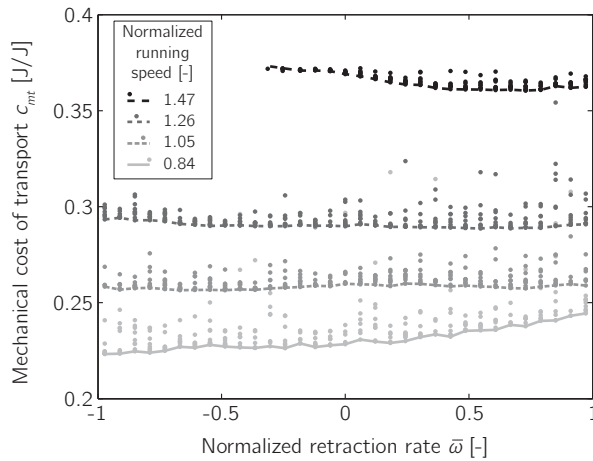


Figure 6.9: The effect of the normalized retraction rate \bar{w} on the minimal mechanical cost of transport of limit cycle running for each of several normalized running speeds 0.84–1.36. Using a wider range on the ordinate axis, the trend of Figure 6.8 is no longer obvious. In fact, swing-leg retraction rate appears to have very little inherent effect on mechanical cost of transport.

becomes particularly clear when the points for optimally efficient limit cycle running at several speeds are plotted against the same axes, as in Figure 6.9. Swing-leg retraction rate no longer appears to affect the optimal efficiency in any significant way. Running speed, for example, has a much more obvious effect on running efficiency than swing-leg retraction rate.

Though the energetic cost of the hand-tuned intuitive controller is much higher than that of the optimized trajectory, the result is qualitatively the same: there is no strong correlation between retraction rate and energetic efficiency.

6.4.3 Discussion

At first glance, Figure 6.9 shows that speed matters: as speed increases, retraction rate for minimal impact loss increases. More significantly, it shows that despite the effect of swing-leg retraction rate on impact losses, there is little inherent effect of swing-leg retraction rate on the overall efficiency of limit cycle running. This appears to be because impact losses are a small portion of the total energy budget. Other factors, such as the energy required to swing the legs and produce vertical impulse, level the curve.

6.5 Impact Forces and Footing Stability

When designing a robot controller, it may be necessary to minimize the magnitude of impact forces at touchdown to avoid damaging the robot, and it is often important to limit sliding between the foot and the ground to avoid slipping and falling. By changing the relative speed between the foot and the ground at touchdown, SLR can have a significant effect on the extent to which these risks are mitigated. In this section, we analyze the effect of SLR on impact forces and slippage.

6.5.1 Methods

The realistic model and the two simplified impact models are not appropriate for predicting the magnitude of touchdown forces, because touchdown is modeled as an instantaneous event with impulses rather than finite forces. However, we can assume that the risk of damage is roughly proportional to the magnitude of the total touchdown impulse. Likewise, the simulation does not predict how much slipping will occur at touchdown because the foot is assumed to stick to the point of ground contact. However, we can assume that slipping at touchdown will depend on the angle of the touchdown impulse: if the impulse angle is zero, the impulse is purely vertical, and slipping is impossible; if the impulse angle is $\pi/2$, the impulse is purely horizontal, and slipping is certain. At intermediate angles, slipping will occur if the

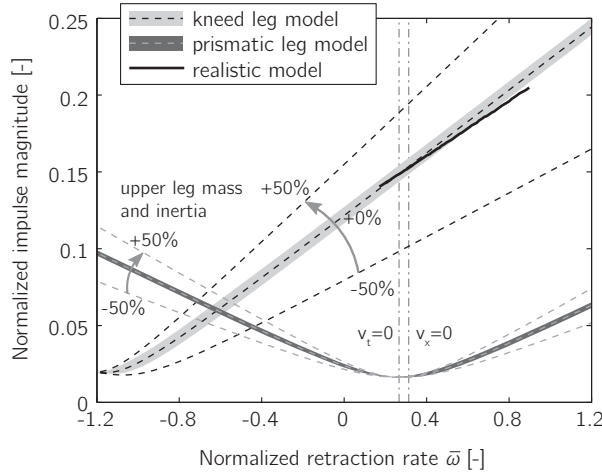


Figure 6.10: The effect of the normalized swing-leg retraction rate $\bar{\omega}$ on the normalized touchdown impulse for the prismatic leg model, kneed leg model, and realistic model. For the simplified models, shaded regions indicate results for a range of touchdown conditions, including variations in instantaneous velocity and angle-of-attack, encountered at touchdown in limit cycles of the realistic model. Lines indicate the mean result for the range of touchdown conditions studied. Lines for simplified models with mass parameters of the Phides robot (+0% upper leg mass) and $\pm 50\%$ upper leg mass are also shown. Results for simulated limit cycle running of the realistic model with Phides-like parameters are represented with a thick black stroke. For reference, a normalized impulse magnitude of 1 would be required if the full mass of the robot translating at 2.37 m/s were to stop completely.

impulse angle exceeds the effective friction angle, the arctangent of the effective friction coefficient.

The impulses are measured by taking the difference between the total linear momentum of the robot immediately after and immediately before the instant of touchdown. The magnitude and angle of the impulse vector are computed during simulation of the realistic model in limit cycle motion under the action of the hand-tuned controller. They are also calculated for the simple prismatic and kneed leg models for a range of retraction rates and for a variety of typical touchdown horizontal speeds, touchdown vertical speeds, angles-of-attack, and swing-leg retraction rates typical of limit cycle running.

6.5.2 Results

Figure 6.10 shows the magnitude of the touchdown impulse as a function of the retraction rate for the prismatic leg model, kneed leg model, and realistic model. For the prismatic leg, the magnitude of the touchdown impulse is minimal at the retraction rate for which foot tangential speed is zero, as anticipated by analysis

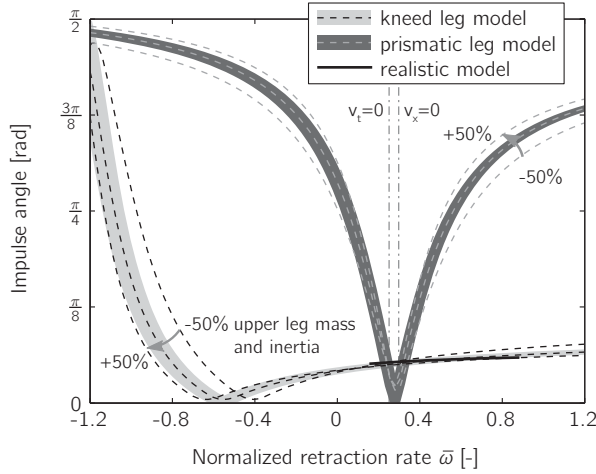


Figure 6.11: The effect of the normalized swing-leg retraction rate $\bar{\omega}$ on the impulse angle for a prismatic leg model, kneed leg model, and realistic model. Impulse angle, or the magnitude of the angle between the impulse and vertical, is defined as $|\text{atan}(l_x/l_y)|$, where l_x and l_y are the horizontal and vertical components of the impulse vector, respectively. A lower value corresponds with an impulse closer to vertical, which corresponds with less slipping at touchdown. See caption of Figure 6.10 for more information.

presented in Chapter 5. However, the minimal touchdown impulses for the kneed leg occur at negative retraction rates very different from the retraction rate of zero foot tangential speed. The realistic robot model shows close agreement with the simplified kneed leg model.

Figure 6.11 shows the angle of the touchdown impulse as a function of the retraction rate. The larger this angle is, the more likely it is that slipping will occur. For the prismatic leg, the retraction rate has a large influence on the impulse angle and the minimal angle occurs near the retraction rate for which the foot tangential speed is zero. For the kneed model, however, the retraction rate has a much smaller effect on the impulse angle. For all normalized retraction rates between -0.8 and 1.2, the impulse angle is below 0.2 rad. Also for the impulse, the realistic robot model shows close agreement with the simplified kneed leg model.

6.5.3 Discussion

Many of the same conclusions of Section 6.3.3 can be drawn from Figures 6.10 and 6.11. Variations within the characteristic range of touchdown horizontal speeds, touchdown vertical speeds, and angles-of-attack have little effect on the magnitude and angle of the touchdown impulse, as indicated by the narrow shaded regions. For

prismatic legs, mass distribution of the leg has little effect on the trend; for kneed legs, the greater the mass of the upper leg segment, the greater the disagreement with the prismatic leg results. In addition, the simplified kneed leg model is representative of the realistic robot model.

Also, it is interesting that the impulse angle observed for the prismatic leg rises sharply from the minimum in either direction, and thus the foot tangential speed must be matched relatively precise to avoid slipping. For example, with a coefficient of friction between a rubber robot foot and concrete of 1, slipping will occur at an impulse angle greater than $\arctan 1 = \pi/4$. For the prismatic leg model, the normalized retraction rate must be within ± 0.3 of that required for $v_t = 0$ to prevent slipping. For the kneed leg, on the other hand, slipping is unlikely for all but the most negative retraction rates. This may be an inherent advantage of a rotary knee over a telescoping joint.

6.6 Stability

In Seyfarth et al. (2003), swing-leg retraction is introduced as a simple control strategy to improve the stability, or small disturbance response, of the SLIP model. In this section, we assess how the retraction rate influences the stability of the SLIP and realistic model.

6.6.1 Method

The stability of a running model can be assessed by analyzing the Floquet multipliers of its step-to-step behavior (McGeer, 1990a; Seyfarth et al., 2003), that is, the eigenvalues of the linearized, discrete step-to-step map A . The map A governs the dynamics of perturbations from limit cycles $\Delta \mathbf{v}_i$ as

$$\Delta \mathbf{v}_{n+1} = A \Delta \mathbf{v}_n \quad \text{with } \Delta \mathbf{v}_n = \mathbf{v}_n - \mathbf{v}^*, \quad (6.9)$$

in which \mathbf{v}_i is the state of the system at a specific point in the gait cycle (e.g. state at liftoff) of the i^{th} step and \mathbf{v}^* is the state at this point in the limit cycle. The Floquet multipliers indicate the rate at which the model converges back to the limit cycle after a small deviation from the limit cycle. A system is stable if the magnitude of all Floquet multipliers is less than unity.

6.6.2 Results

Figure 6.12 shows how the magnitude of the Floquet multipliers varies across a range of retraction rates for the SLIP and the realistic model respectively. The Floquet multipliers for the realistic model are shown only for retraction rates for which the

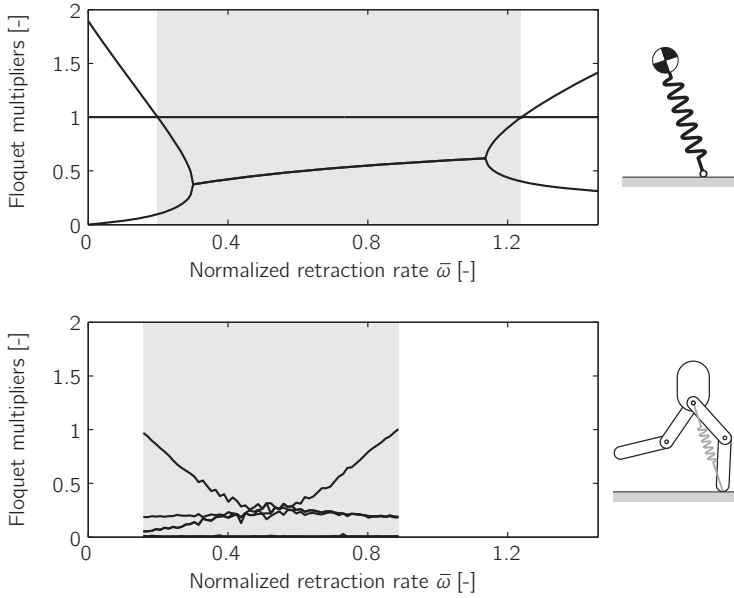


Figure 6.12: Floquet multipliers as functions of normalized retraction rate for both the SLIP model and the realistic model. The grey areas indicate the range of normalized retraction rates for which the models are stable. This figure shows that the retraction rate does affect the stability of both the SLIP and realistic model. However, the models do not agree on the range of retraction rates that result in stable gaits.

model has a stable limit cycle, as our method for finding limit cycles requires the model to be stable.

The SLIP model has three Floquet multipliers, as the state at apex can be described by the three state variables: apex height, horizontal speed, and leg angle. Due to the energy conservative nature of the SLIP model, one of the Floquet multipliers is always unity, signifying that disturbances to energy level persist. Neither swing-leg retraction nor any other angle-of-attack controller can affect this trivial eigenvalue. Formally, a limit cycle is marginally stable if the magnitude of at least one Floquet multiplier is equal to unity and the magnitude of all other Floquet multipliers is less than unity. Thus, the trivial eigenvalue prevents any SLIP limit cycle from being truly stable. However, we neglect this technicality and refer to any marginally stable limit cycles of the SLIP as “stable”.

The magnitude of the other two Floquet multipliers is less than unity for normalized reaction rates between 0.20 and 1.24. Outside this range, one of the Floquet multi-

pliers has a magnitude greater than unity, which means that the limit cycle running is unstable at these retraction rates. The convergence rate is maximal at a normalized retraction rate of 0.30, where the largest magnitude of the two nontrivial Floquet multipliers is minimal.

The realistic model has eight Floquet multipliers, as the state at touchdown can be described by eight state variables corresponding with the angle and angular rate of the upper and lower segments of both the stance and swing leg. Four of the Floquet multipliers are almost zero over the range of retraction rates, which is due to the stiff position control of the knees. The realistic model is stable if the magnitude of all Floquet multipliers is below unity, which is the case for normalized reaction rates between 0.15 and 0.89. Within this range of stable retraction rates, a normalized retraction rate of 0.46 results in the greatest convergence rate.

6.6.3 Discussion

Both models show that the retraction rate affects the stability. However, the models show different ranges of retraction rates for which the model is stable. The lowest retraction rate at which the model is stable is the same for both models at about 0.2. On the other hand, the highest retraction rate at which the model is stable is 1.24 for the SLIP model and only 0.89 for the realistic model. In addition, the trend of the largest non-trivial Floquet multiplier differs between the models. For the SLIP model, this Floquet multiplier is nearly constant over most of the range of stable retraction rates, while for the realistic model it varies from a maximum of unity at the boundaries of the range of stable retraction rates to 0.3 at the center of the interval. This suggests that the SLIP model is not very suitable for studying the effects of swing-leg retraction on stability, and it cannot be used to select the retraction rate for optimal stability of realistic models or physical robots.

6.7 Disturbance rejection

Besides affecting the stability with respect to infinitesimal disturbances, swing-leg retraction also affects the response to large disturbances. In this section, we quantify how the large disturbance rejection of the simple SLIP model and the realistic model are influenced by the swing-leg retraction rate.

6.7.1 Method

In the field of legged robots, many ways to quantify the rejection of large disturbances have been proposed, but there is little agreement on a standard. In this chapter, we show the effect of swing-leg retraction on three disturbance rejection measures:

settling time, *maximal single relative disturbance*, and *mean steps to fall*. These were selected because they are intuitive measures of how well a robot can handle real-world disturbances and because their computational costs are not excessive.

The *settling time* is the time that a system takes to return to a steady gait after a disturbance (Jindrich et al., 2002). For running systems, it is important to return to a steady gait quickly; the slower the convergence, the more likely for successive disturbances to move the system progressively further from the limit cycle to failure. The return to a limit cycle is measured using a gait indicator, a quantitative characteristic of the gait that, when outside a normal range, is observed to correlate with failure. We use the step time as gait indicator, because it is shown to correlate well with failure in Hobbelen and Wisse (2007a) and Chapter 2. We define the settling time as the number of steps after a disturbance before the step time is within 0.1% of its steady state value. As the disturbance, we use an energy-neutral step-down; in addition to a step in ground height, the forward speed is adjusted to keep the system energy constant. This disturbance is chosen because it allows the energy conservative SLIP-model to return to the original limit cycle. The step-down is chosen to be 3.5% of the leg length, as this disturbance did not cause either model to fall for a wide range of retraction rates.

The *maximal single relative disturbance* is the maximum change from a known limit cycle state from which the robot will not fall within a prescribed number of steps (McGeer, 1990b; Pratt et al., 2001; Wisse et al., 2005b). This measure gives an indication of the size of the basin of attraction, which is the collection of all initial states that do not lead to a fall. We consider two types of single relative disturbances:

- A push disturbance is an increase (push forward) or decrease (push backward) from a known limit cycle apex hip velocity. This is equivalent to the application of an impulse uniformly distributed over the mass of the robot.
- A step disturbance is an increase (step down) or decrease (step up) from a known limit cycle apex hip height. This is equivalent to a single step in the floor over which the robot is running.

The maximal single relative disturbance is determined by applying increasingly large disturbances until the model falls within 25 steps of the disturbance.

The *mean steps to fall* metric is inspired by a measure of manufacturing system reliability known as mean time to failure (Blanchard et al., 1995). Mean steps to fall is defined as the mean number of steps, starting from a known limit cycle state, before a robot falls under a sequence of finite random disturbances of a given distribution. We consider two types of random absolute disturbances applied at apex:

- Step disturbances are perturbations in the apex vertical height above mean ground level. These perturbations are sampled from a Gaussian distribution with zero mean and specified standard deviation; they are equivalent to random steps in the floor over which the robot is running.
- Push disturbances are perturbations in the apex horizontal speed. These perturbations are sampled from a Gaussian distribution with zero mean and specified standard deviation, and are equivalent to a random sequence of impulses, each uniformly distributed over the mass of the robot.

Mean steps to fall is estimated by measuring the number of steps to fall over 100 different sequences of disturbances taken from a Gaussian distribution, then averaging across all trials.

In order to test the disturbance rejection of the realistic model, we must define fall modes that constitute failure. The most obvious fall mode is when the hip touches the ground. Another fall mode is when the swing foot touches the ground (trip). The third fall mode is when the model touches down with the stance leg bent further than the rest length of the leg spring permits. It is necessary to enforce this condition as a fall to prevent the leg spring from engaging at a non-zero energy level. The robot Phides has a similar fall mode, because its leg spring only engages at the spring rest length; the leg will collapse if the rest length is not reached before touchdown.

6.7.2 Results

Figure 6.13 shows the settling time as a function of the retraction rate for the two models. In addition, it shows the response of the gait indicator for three retraction rates. For low retraction rates, the gait indicator slowly converges to its steady state value. With increasing retraction rates, the convergence rate increases and settling time decreases. If the retraction rate is increased too much, the gait indicator overshoots and oscillates about its steady state value. The two models both show this effect of the retraction rate on the settling behavior, but the ranges of retraction rates for which each behavior occurs differ between the models.

Figure 6.14 shows the maximal single step and the maximal push disturbance for a range of retraction rates for the two models. The effect of the retraction rate on the maximal single relative disturbance seems to differ between disturbances that add energy and those that remove energy. For disturbances that remove energy from the system, like the step-up and the backwards push, the maximal disturbance increases with increasing retraction rate until the retraction rate for which the system becomes unstable. On the other hand, for disturbances that add energy to the system, like the

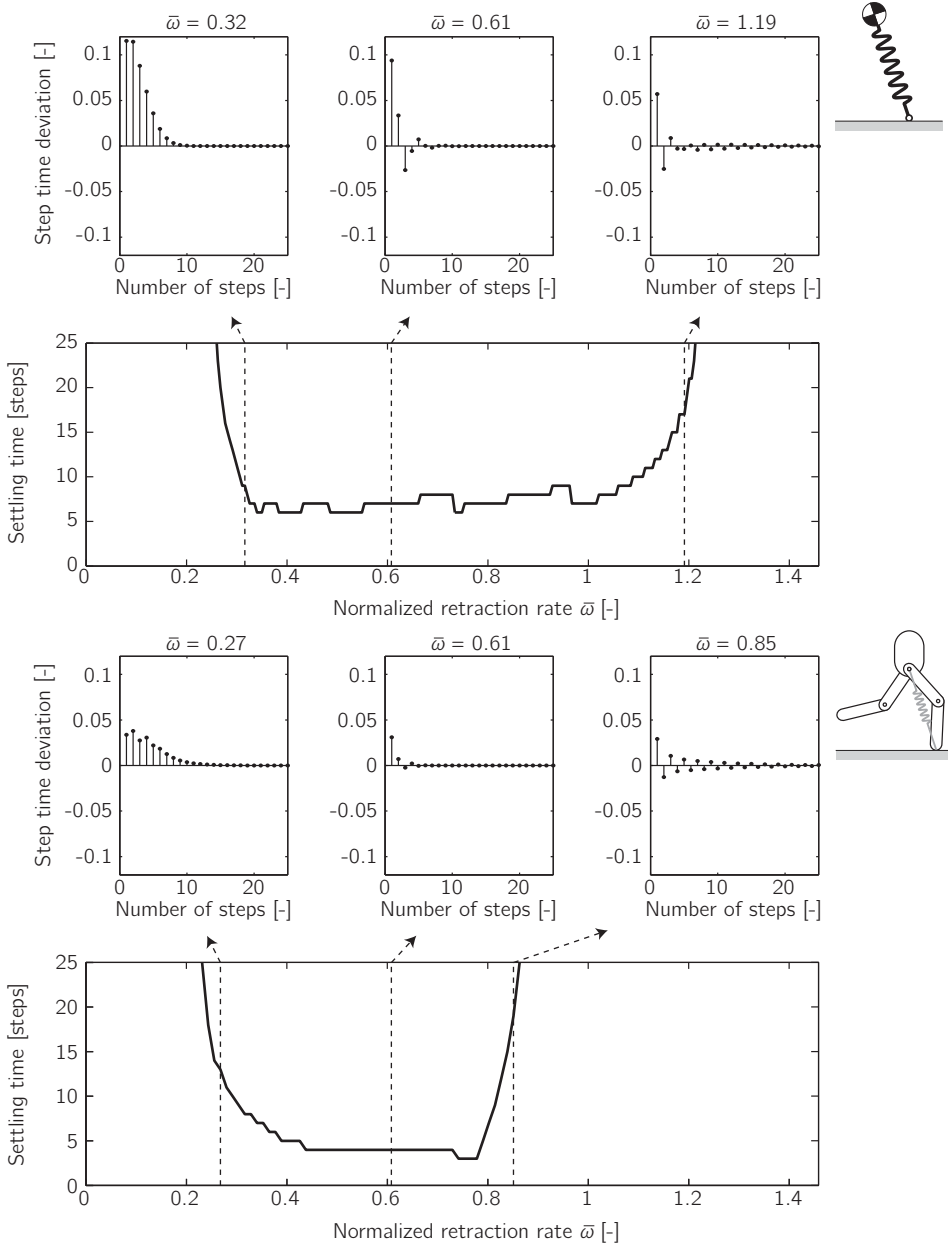


Figure 6.13: The settling time as function of the retraction rate for the two simulation models. The settling time indicates how quickly the system returns to a steady gait after a disturbance. An energy-neutral step-down 3.5% L_0 was used as disturbance. The inserts show the response of the gait indicator, step time, after a disturbance for three retraction rates. At low retraction rates there is slow convergence, at medium retraction rates there is quick convergence, and for high retraction rates there is an oscillating convergence.

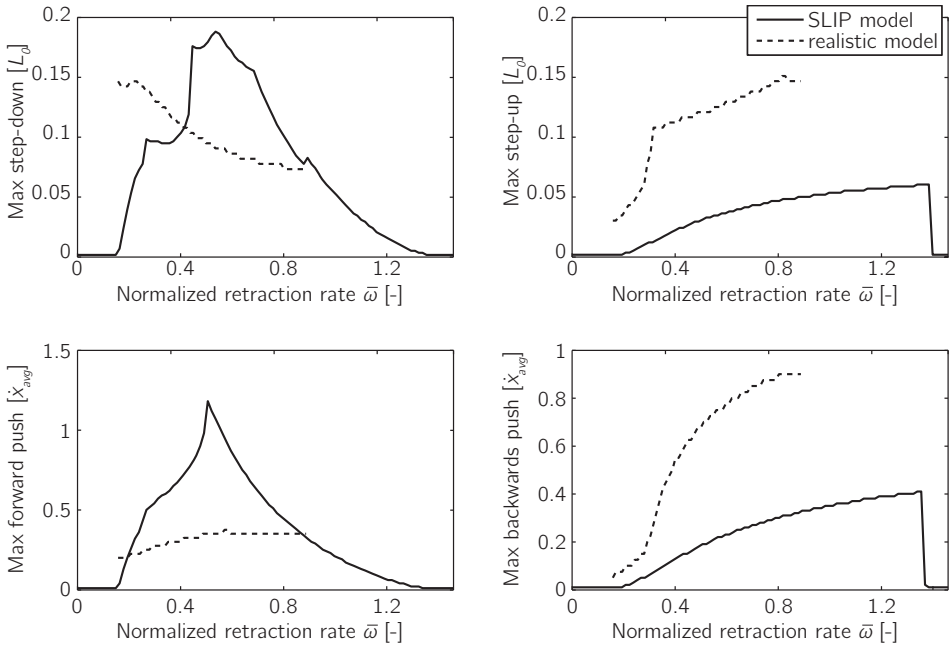


Figure 6.14: The maximal single relative disturbance as a function of the normalized retraction rate of the SLIP and realistic model. Four kinds of disturbances are used: step-down (top left), step-up (top right), forward push (bottom left), and backwards push (bottom right).

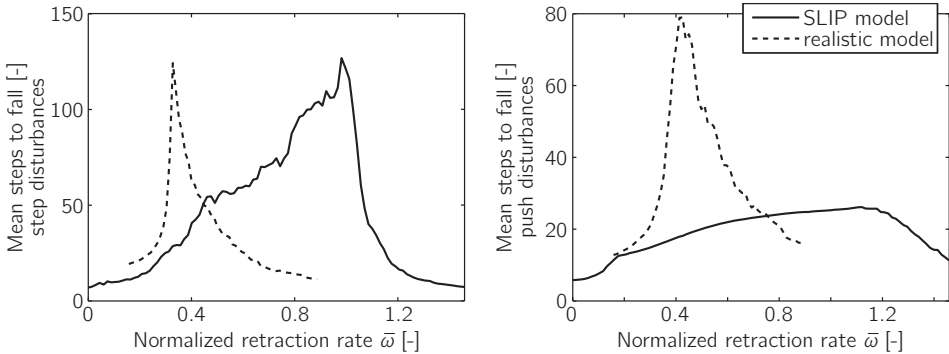


Figure 6.15: The effect of the retraction rate on the mean steps to fall for both simulation models. The mean steps to fall is shown for random step disturbances with a standard deviation of $2.6\% L_0$ (left) and push disturbances with a standard deviation of $15\% \dot{x}_{avg}$ (right).

step-down and the forward push, the maximal disturbance peaks at a lower retraction rate, especially for the SLIP model.

While both models reveal that retraction rate greatly affects the maximal single relative disturbance, there are large quantitative differences. For example, the maximal step-up the realistic model can handle is about two times as large as what the SLIP model can handle. In fact, the only quantitative agreement between the two models is that for maximal forward push, both models achieve maximal disturbance at a normalized retraction rate of about 0.55-0.6, but here the peak for the SLIP model is sharply defined whereas for the realistic model the curve is relatively flat.

Figure 6.15 reveals a substantial effect of the retraction rate on the mean steps to fall. With a normalized retraction rate of 0.33, the realistic model rejects step disturbances for an average of 124 steps, where with a retraction rate of 0.63 it only averages 21 steps. It is interesting that the maximal mean steps to fall for the step disturbances occurs at nearly the same retraction rate for maximal mean steps to fall with push disturbances. This holds for both the SLIP and the realistic model, but the optimal retraction rate for the SLIP model is at a much higher retraction rate than the optimal retraction rate of the realistic model. Also, the value of the maximum mean steps to fall with push disturbances is several times higher for the realistic model than for the SLIP model.

6.7.3 Discussion

There is an interesting correlation between settling time and stability. For instance, the SLIP model has a substantially wider range of retraction rates for which the settling time is very low, or less than 5 steps, than the realistic model. This reminds us of the SLIP's wide range of low, nearly-constant, maximal, non-trivial eigenvalue. Also, the range of retraction rates in which the settling time is reasonable, or less than 25 steps, corresponds with the ranges for which the models are stable.

All three measures show that swing-leg retraction has a large influence on the disturbance rejection behavior for the SLIP model as well as the realistic model. However, the trends are different for the three measures and are dependent on the kind of disturbance used. This indicates that if swing-leg retraction is implemented to increase disturbance rejection, the retraction rate should be chosen based on the expected disturbances; it cannot be chosen to maximize rejection of all disturbance types at once.

Comparing the result of the SLIP model and the realistic model, we can see that the models qualitatively agree on some of the disturbance rejection measures, such as settling time, maximal step-up, and backwards push. However, there is no agreement

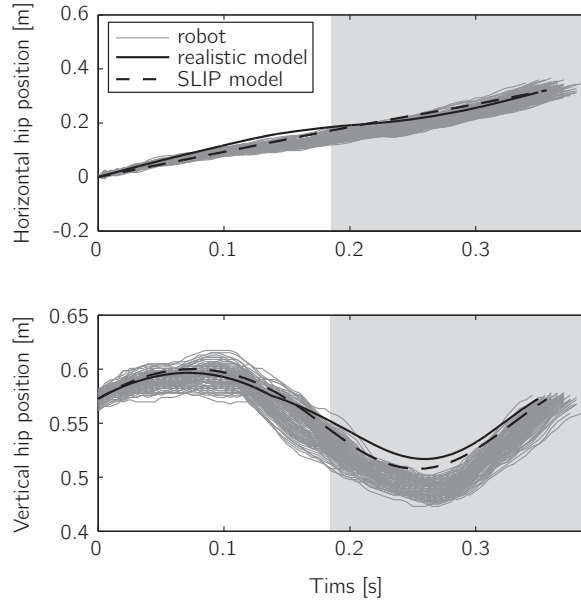


Figure 6.16: Comparison of the hip trajectory of the SLIP model, realistic model and robot, all with a normalized retraction rate of 0.62 and running at a normalized speed of 0.38. The robot's hip trajectory are of 108 consecutive steps, with the horizontal hip position defined to be zero at liftoff. The white areas indicate the average duration of the flight phase of the robot and the grey areas indicate the stance phase.

on other disturbance rejection measures like the mean steps to fall. In addition, there is no quantitative agreement for any of the measures, which means that the SLIP model cannot be used to select the optimal retraction rate for realistic robot models or robots.

6.8 Discussion

6.8.1 Realistic model validation

The realistic model used in this chapter is based on the running robot Phides. To test the validity of the realistic model, we compare its behavior with the robot's behavior at a normalized retraction rate of 0.62. For completeness, we also include the SLIP model in this comparison. First, we compare the hip trajectories as shown in Figure 6.16. There is a close agreement between the hip trajectory of the models and the robot, which suggests that they have similar limit cycles.

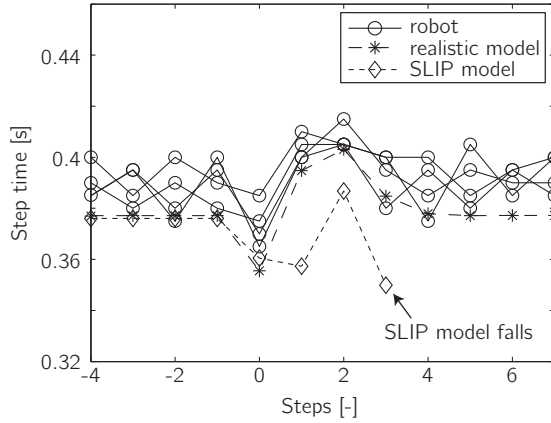


Figure 6.17: The response in step time, measured from liftoff to liftoff, of the SLIP model, realistic model and robot on a relative step-up disturbance of 5% L_0 while running at a normalized speed of 0.33. The robot response is shown for four separate trials. The step time of the robot is measured with a resolution of 5 ms. The robot and the realistic model show a decrease in step time at the step-up followed by an increased step time for the following steps. The SLIP model has a different response in step time and falls in the 4th step after the disturbance.

For the experiments in this chapter, it is important that, besides having similar limit cycles, the model and the robot respond similarly to disturbances. Figure 6.17 shows the response to a relative step-up disturbance of 5% L_0 of both models and the robot. The realistic model and the robot have a similar response, with a decrease in step time at the step-up followed by an increased step time for the next steps, then converges back to the nominal step time. The SLIP model, on the other hand, has a different response to the step-up disturbance. It responds with a sequence of two short steps, a long step, and a short step, after which the SLIP model falls. This shows that the SLIP model does not capture the disturbance response of the robot well.

Based on these two comparisons, we believe that the effects of swing-leg retraction on the realistic model transfers over to the robot. To further validate the results of this study, we plan to implement swing-leg retraction on the robot with a wide range of retraction rates and measure all the performance metrics addressed in this chapter.

6.8.2 Effect of starting point

In the literature, swing-leg retraction is usually initiated at apex (Blum et al., 2010; Ernst et al., 2009; Seyfarth and Geyer, 2002; Seyfarth et al., 2003). However, for

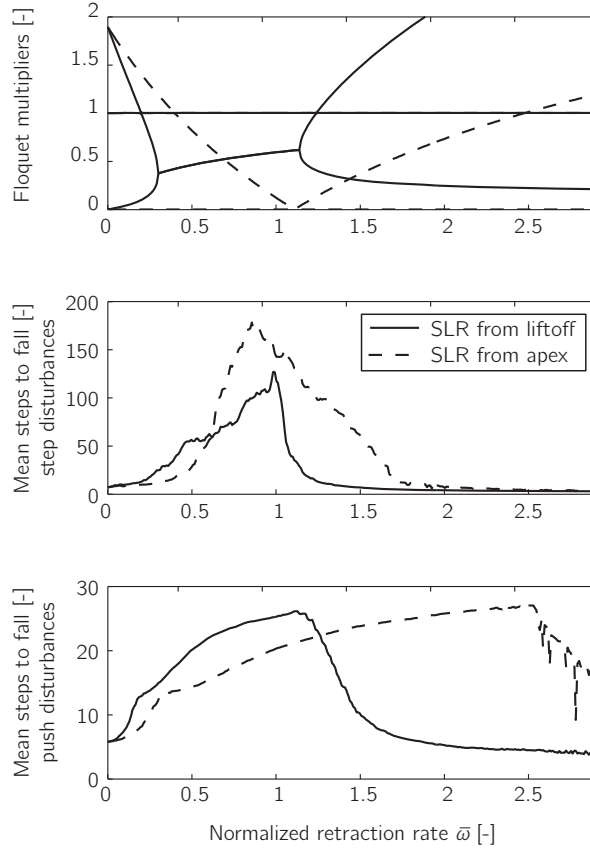


Figure 6.18: Effect of the starting point of the swing-leg retraction on the stability and the mean steps to fall for a range of retraction rates. The top figure shows the stability in terms of the Floquet multipliers. The middle and bottom figures show the mean steps to fall for step and push disturbances, respectively.

all experiments in this chapter, swing-leg retraction was initiated at liftoff. This was done because in practice liftoff is much easier to detect than apex. Of all the experiments in this chapter, the starting point of the leg retraction only affects the stability and disturbance rejection experiments. To determine the effect of the starting point on the results of these experiments, we compare the stability and the mean steps to fall of the SLIP model between SLR from apex and SLR from liftoff.

Figure 6.18 shows the results for both starting points, which shows that both the stability and disturbance rejection is affected by the starting point. Note that with the start point at apex, there are only two instead of three Floquet multipliers as

the model on apex is fully defined by two state variables. Interestingly, the range of retraction rates for which the model with SLR from apex is stable is at double the retraction rates for which the model with SLR from liftoff is stable. This can be explained by the fact that a change in initial conditions at liftoff that increases the flight time, e.g. an increase in the vertical speed, will increase the time from liftoff to touchdown twice as much as the time from apex to touchdown due to the symmetry of the takeoff and touchdown angles. Therefore, to have the same effect on the touchdown angle, the retraction rate for SLR from apex should be twice as high as for SLR from liftoff.

The disturbance rejection in terms of mean steps to fall with push disturbances also shows the doubling of the retraction rates. On the other hand, the disturbance rejection in terms of mean steps to fall with step disturbances does not show the doubling of the retraction rates, because a step disturbance affects the time from liftoff to touchdown and the time from apex to touchdown by the same amount.

Overall, we can conclude that both SLR from liftoff and from apex can increase the stability and disturbance rejection. The starting point affects which rejection rate results in the optimal stability or disturbance rejection behavior. It is impossible to say which starting point is better for disturbance rejection, because this is highly dependant on the kind of disturbances that are present and the selected retraction rate. For example, SLR starting at apex has a higher maximal mean step to fall for step disturbances, but at the optimal retraction rate for this metric the mean steps to fall for push disturbances is lower than for SLR starting at liftoff.

6.8.3 Are the trends of the models consistent?

This question is discussed separately for the different performance metrics in Sections 6.3.3, 6.5.3, 6.6.3, and 6.7.3. In summary:

- The SLIP model correctly predicts that a modest swing-leg retraction rate will improve both stability and disturbance rejection, and it correctly identifies the shape of many trends in a qualitative sense. However, because it does not make an accurate quantitative prediction of the location of extreme points for any curve, it cannot be used to predict whether increasing the retraction rate from a certain positive value will improve or degrade stability or disturbance rejection.
- The prismatic leg model does not predict the trends observed in the realistic model for impact loss, impulse magnitude, or impulse angle; in all of these cases, it even gets the direction of the optimal retraction rate wrong.

- The kneed leg model correctly predicts the trends observed in the realistic model for impact loss, impulse magnitude, and impulse angle.

One might argue that it is obvious that the results of the prismatic leg model would not agree with the realistic model due to fundamental differences in their morphology. But clearly, differences in morphology cannot always preclude agreement between simple models and realistic models or physical robots, or it is unlikely that the SLIP model would be such a popular model in the literature. Because it is difficult to assess a priori and on intuitive grounds whether a given model simplification will accurately predict trends of a more realistic model, we believe it is important to study realistic running models in conjunction with simple models. Simple models may be used to help identify new phenomena or explain known behaviors, but in either case the extent of agreement with more realistic models must be studied in order for the results to be most useful for application to running machines.

6.8.4 Optimal retraction rate

In this chapter, we investigated the effect of the swing-leg retraction rate on the following six performance metrics: impact losses, cost of transport, impact forces, the risk of slipping, stability, and disturbance rejection. The retraction rate has a substantial effect on all but one of these performance metrics, namely the cost of transport, for which the maximal effect is less than 3%. For all the other studied performance metrics, there is a substantial improvement by swinging the leg at a non-zero retraction rate compared to no retraction. However, the maximal improvement for each performance metric is found at a different retraction rate. For the realistic model, there are even performance metrics that require a negative retraction rate for the optimal performance. This presents a trade-off when selecting the retraction rate, which is in agreement with Chapter 5.

The results of this chapter also showed that the effect of swing-leg retraction is very dependant on leg morphology, especially for the performance metrics that are strongly affected by the touchdown dynamics. For a kneed leg morphology, the mass distribution also affects the effect of swing-leg retraction. As a result, we cannot recommend any simple formula for selecting an overall optimal retraction rate. If the control system is designed such that retraction rate is a relatively independent parameter, the “optimal” retraction rate will likely depend on the specific design of the robot, the particulars of the rest of the control system, and the relative importance of the different performance metrics. The retraction rate should be chosen accordingly, based on simulation and experiment.

For Phides, we are not interested in demonstrating energetic efficiency, we have not noticed severe problems with slipping at impact, and there are not particular concerns about impact forces damaging the robot. We believe Phides' greatest contribution would be in the area of robustness against typical real-world disturbances such as an uneven floor, so we would choose a moderate positive retraction rate near $\bar{\omega} = 0.4$, which is a compromise among low maximum eigenvalue magnitude, low settling time, and high mean steps to fall under random step disturbances. Under this controller, we believe the robot would exhibit quick recovery and few falls when subject to the perturbations of common outdoor terrain such as asphalt, sidewalks, and low grass.

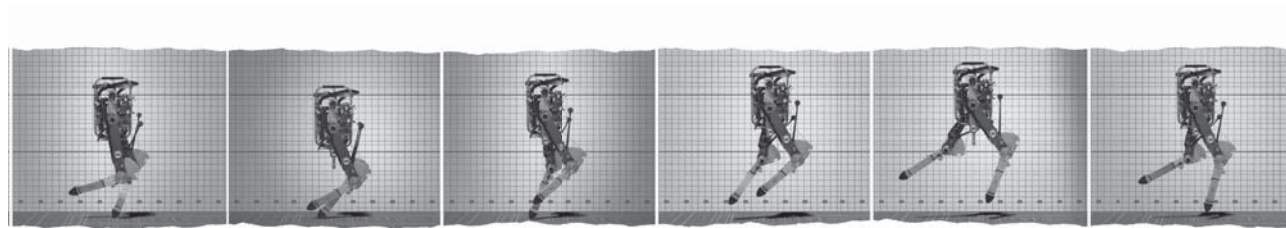
6.9 Conclusion

In this chapter, we showed how the benefits of swing-leg retraction depend on the retraction rate for simple and realistic mathematical models and for a physical robot. Based on these results we conclude that:

- Swing-leg retraction can be used to decrease the impact energy loss, but the overall effect on efficiency, as measured by mechanical cost of transport, is small.
- Swing-leg retraction can decrease touchdown forces and increase footing stability, as estimated by impact impulses.
- Swing-leg retraction can increase several measures of stability and disturbance rejection, and can, to a limited extent, increase all measures simultaneously.
- The optimal retraction rate depends heavily on which metrics of running performance are valued and the specifics of the systems; generalizations are difficult to generate.
- A prismatic leg is not a satisfactory simplification of a kneed leg when considering the touchdown impact event; the impact dynamics of the two models are fundamentally different.
- The SLIP model may be a useful template for prediction of running behaviors such as hip trajectories (Blickhan, 1989), but it is not a satisfactory simplification of a general running robot for the study of some complex behaviors like stability and disturbance rejection.

7

Discussion, conclusions and future directions



This is the final chapter of this thesis. This chapter starts with a recapitulation of the research goal and the results of this research in Section 7.1. Next, these results are discussed in Section 7.2, followed by the main conclusions of this thesis in Section 7.3. This chapter ends with the future directions in Section 7.4.

7.1 Recapitulation

As posed in the Section 1.5, the goal of this thesis is to increase the understanding of the human running gait by means of gait synthesis, with a focus on the disturbance rejection behavior. To achieve this research goal, three questions were addressed. The main results on these questions are:

- *How is the disturbance rejection behavior affected by the stiffness profile of the leg compliance?*

This question is addressed in Chapter 2, where a simulation study of the effect of nonlinear leg stiffness is presented. In this study, the leg stiffness profile of a simple running model is optimized to maximize the disturbance rejection. The results of this study show that the leg stiffness profile has a significant influence on the disturbance rejection behavior. For the simple running model, we show that nonlinear leg springs can improve the disturbance rejection up to a factor 7 compared to the optimal linear leg spring. The optimal leg stiffness profile for the maximal disturbance rejection behavior is strongly nonlinear. With this optimal stiffness profile, the leg force rises as the leg is compressing, until a maximum force is reached. After the maximal force is reached, the leg force decreases when the leg is further compressed. We did not find a mechanical explanation on why this stiffness profile results in a high disturbance rejection. However, we found that all stiffness profiles that result in high disturbance rejection have a high overall stiffness in combination with a low spring force at maximal compression.

- *How is the disturbance rejection behavior affected by the center-of-mass location of the torso?*

Commonly, the center-of-mass (CoM) of the torso is located on the hip, reportedly to allow for simple control schemes. However, this location of the CoM does limit the disturbance rejection, as the rotation of the torso cannot be used to influence the CoM position of the whole robot. In Chapter 3 the influence of the CoM location of the torso on the disturbance rejection behavior is investigated with a simulation study. In this study, the disturbance rejection is quantified as the largest disturbance that can be corrected within a

single step. The results of this study show that the CoM location has a large influence on the disturbance rejection. The optimal CoM location depends on the type of the expected disturbance, which is above the hip for floor height disturbances and below the hip for push disturbances on the center-of-mass. The commonly used center-of-mass location at the hip is never optimal. An offset of the CoM-location can increase the disturbance rejection up to a factor of 10 compared to the CoM at the hip.

- *How is the disturbance rejection behavior affected by the swing-leg retraction rate?*

Swing-leg retraction is the backwards rotation of the front leg prior to touch-down. The backwards rotation speed of the leg, called the retraction rate, has two effects on the running motion. Firstly, the retraction rate influences the impact dynamics by changing the relative speed of the leg with the ground, which can reduce impact energy loss, likelihood of slipping, and impact forces. Secondly, swing-leg retraction can cause a stabilizing effect by making the angle-of-attack a function of the flight time. In Chapters 5 & 6, we show that swing-leg retraction does indeed improve the disturbance rejection and reduces impact energy loss, likelihood of slipping, and impact forces. However, the optimal retraction rate for maximal disturbance rejection and stability is different from the optimal retraction rate for minimal impact losses, peak forces, and foot slipping. This discrepancy indicates an inherent tradeoff to consider when selecting the retraction rate for a robot control system: in general, retraction rate can be optimized for better stability and disturbance rejection or for more favorable efficiency, impact forces, and footing stability, but not all simultaneously.

7.2 Discussion

7.2.1 Transfer of results from simple models to realistic models and robots

Most of the research in this thesis was conducted on simple simulation models, because they allow to study the running gait fundamentals due to their simple dynamics. However, the question is: how well do the results of the simple models transfer to more realistic models and to robots? To answer this question we can look at the results of the study into the effect of swing-leg retraction (Chapter 6), because this study is conducted on a simple model, a realistic model, and a robot.

The effect of the swing-leg retraction on the impact dynamics was studied on a simple model with a telescopic leg and on a realistic model with a kneed leg. The results of this study show that for both models there is a significant effect of the retraction rate on the impact dynamics. However, the retraction rates at which these effects occur differs between the models. The minimal impact losses, for example, occur for the telescopic leg model at a positive retraction rate (leg swings backwards) at which the foot speed tangential to the leg is zero, where the minimal impact losses for the kneed leg model occurs at a negative retraction rate (leg swings forward). This difference in optimal retraction rates is caused by the fact that rotation of the upper leg of the kneed leg is the result of the leg compressing and of the rotation of the whole leg. The leg compression results in the upper leg rotating forward just after touchdown, which makes that swinging the leg forward just before touchdown reduces the impact losses. For a telescopic leg, the leg compression does not effect the rotation of the leg and therefore the whole leg will rotate backwards after touchdown, which makes that swinging the telescopic leg backwards just before touchdown reduces the impact losses.

The effect of the swing-leg retraction on the stability and the disturbance rejection was studied on the simple SLIP model, on a realistic model and on the robot Phides. The results of this study show more similarity between the two models than was the case for the impact dynamics. Both the simple and realistic model have stable gaits at low positive swing-leg retraction rates, but the range of retraction rates is smaller for the realistic model.

Based on these results, we can conclude that not all the results of the simple models transfer to more realistic models and robots, especially for effects that involve the impact dynamics. The most important impact-related effect that will need to be reconsidered, is the idea of "ground speed matching". Based on simple models, it is generally accepted that the lowest impact losses will occur when the swing leg retracts during heel strike, but this research shows that this result does not hold for more realistic models. This shows that it is always necessary to validate the results of simple running models on more realistic models or robots. Therefore, we would also recommend that the two studies in this thesis that were only conducted on a simple model (Chapters 2 & 3) should be validated on a realistic model or robot.

7.2.2 Understanding of the human running gait to improve orthoses and prostheses

The goal of this thesis was to increase the understanding of the human running gait so that better prostheses and orthoses for running can be developed. This section discusses how the results of this research apply to the human running gait and how

they can be used to improve running prostheses and orthoses. The three properties that were studied in this thesis are addressed one by one.

Leg stiffness profile

The optimization study in Chapter 2 showed that the leg stiffness profile has a large influence on the disturbance rejection and that the stiffness profile for the optimal disturbance rejection behavior is strongly nonlinear with a local negative stiffness. These results show that it would be useful to study the effect of nonlinear springs in running prostheses and exoskeletons. The implementation of nonlinear springs in exoskeletons could be done in a similar way as was done in the running robot Phides, with a spring attached to a rotational joint by a nonlinear transmission. For lower leg running prostheses, it might be harder to implement nonlinear leg springs with local negative stiffness, as these prostheses often consist of just one large leaf spring.

Center-of-mass location

In Chapter 3, it is shown that a torso center-of-mass (CoM) with a offset from the hip improves the disturbance rejection. This result does not imply that humans have an offset of the CoM position to have improved disturbance rejection, as the CoM position of humans is affected by many things, e.g. the need to have eyes high up in the body. However, the CoM position of the human torso (including arms and head) has an offset of about 39% of the leg length (de Leva, 1996), which results in good disturbance rejection.

Swing-leg retraction

In Chapters 5 & 6, it is shown that swing-leg retraction can improve the disturbance rejection and can reduce the impact losses and forces, but that this does not occur at the same retraction rate. This result can give insight into the reasons why humans use swing-leg retraction. This can be done by comparing the optimal retraction rates found in this study to the retraction rate humans use during running. This should be done over a range of running speeds, as the running speed has a large influence on the optimal retraction rates. As far as we know, there is no data published on the human retraction rate other than the data by Seyfarth et al. (2003) and Blum et al. (2010) on a single running speed. Therefore, we suggest that this data would be gathered and be compared with the optimal retraction rates.

In Chapter 6, it is also shown that leg morphology has a great influence on the impact dynamics. This is a relevant result for the development of running orthoses and prostheses, because it shows that the morphology of orthoses and prostheses is important. For these devices, impact dynamics are important, as an unfavorable

impact can result in high impact losses and can cause slipping. The results also show that there is not a single optimal morphology, as there is a trade-off between impact effects, like impact losses and the chance of slipping on impact.

7.2.3 Addition of feet

The robot and all the simulation models in this thesis do not have feet with ankle joints. This was done to reduce the complexity of the robot and models and because the extra mass of feet would increase the leg inertia with respect to the hip substantial, which would increase the swing time. However, feet may improve the disturbance rejection behavior, as they allow the center of pressure to be moved within the foot contact area.

Recently, we studied the influence of passive feet on the disturbance rejection during running (Reuijl, 2012). Although this study is not part of this thesis, the preliminary results are nevertheless presented here, because the results are relevant for this thesis.

This study focuses on passive feet, which are feet where only springs, and not actuators, apply forces on. We focus on passive feet, because in general they have the advantage of a lower mass than actuated feet, which reduces the leg inertia and therefore the required hip torque.

The effect of passive feet is studied with a 2D simulation model, which consists of a point mass with a massless leg and foot. The leg has an arbitrary compliance between the point mass and the foot. This leg compliance is implemented as a potential field, which is active during the stance phase. The potential field creates a force on the center-of-mass as a function of the horizontal and vertical position of the center-of-mass relative to the foot. This implementation of the leg compliance allows to mimic many different leg configurations, e.g. a leg configuration with a knee and ankle joint where a biarticular spring connects the foot with the upper leg. Note that with a foot size of zero, this model is the same as the model used for the study of the nonlinear leg spring in Chapter 2.

The role of the feet on the disturbance rejection is investigated by optimizing the shape of the potential field to maximize the disturbance rejection. The shape of the potential field is constrained such that center of pressure stays within the foot and that ground reaction force is only pushing against the ground. The disturbance rejection is quantified with the return rate, which measures how close the model gets to the nominal gait within a single step after being disturbed for a range of disturbances.

Figure 7.1 shows the main result of this study, the effect of the foot size on the return rate. It can be seen that, as would be expected, the disturbance rejection

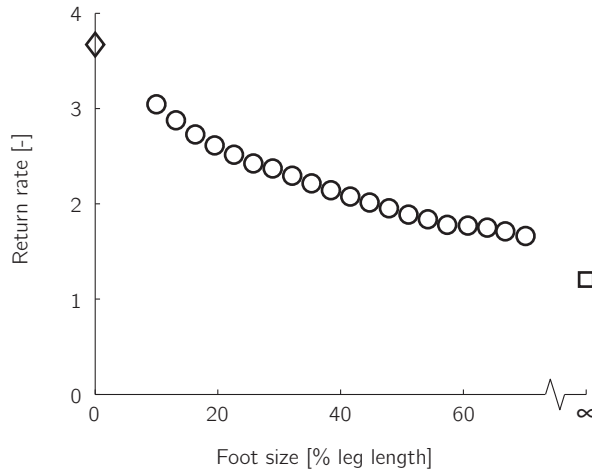


Figure 7.1: The return rate as a function of foot size. The return rate is a measure for the disturbance rejection. A lower return rate indicates a better disturbance rejection. The models with the finite foot size (circles) show that the return rate decreases with increasing foot size. The point foot model (diamond) has a higher return rate than all models with a non-zero foot size. The model with infinite foot size (square) has a lower return rate than all other models, but is not zero, which indicates that even with an infinity foot size not all disturbances are completely rejected within a single step.

improves with increasing foot size. This improvement is however limited as even with infinite foot size the return rate does not reach zero. These results indicate that passive feet can increase the disturbance rejection. However, the improvement is not as large as might be expected. For a realistic foot size of 30% of the leg length, the improvement is only 38% over a point foot.

7.3 Conclusions

The main conclusions of this research are:

- The leg stiffness profile has a significant influence on the disturbance rejection behavior. The stiffness profile for the optimal disturbance rejection behavior is strongly nonlinear.
- The center-of-mass location of the torso does influence the disturbance rejection. The commonly used center-of-mass location at the hip is never optimal and is for two-step correcting strategies the worst option.

- Swing-leg retraction can improve the disturbance rejection and reduce impact energy loss, likelihood of slipping, and impact forces. The optimal retraction rate for disturbance rejection is at a moderate rate and decreases with increasing running speed. The optimal retraction rate for all the other benefits of swing-leg retraction depends on the leg morphology and mass distribution.
- Not all results from simple running model studies transfer well to more realistic models and robots. This is especially the case for studies on effects that involve impact dynamics, as impact dynamics depend greatly on the leg morphology.

7.4 Future directions

To further increase the understanding of the human gait, research should be done in three directions: (1) combining the property variations, (2) extending this research to even more humanlike systems, and (3) applying the results to improve the design of running devices.

7.4.1 Combining

In this thesis, the effect of three important property variations on the disturbance rejection behavior was investigated. The effect of these three property variations was studied separately, to single out the effect of each property variation. The next step is to select the most effective property variations and combining these in one system. This can be, for example, implementing swing-leg retraction on a system with nonlinear leg springs. For these combined implementations, it is important to take the interactions between the property variations into account. In case of the nonlinear leg springs and swing-leg retraction, it could happen that both react to a disturbance, which results in overcompensation.

7.4.2 Extending

In this research, the results of the spring leg runners were extended to a more humanlike system with kneed legs and substantial leg mass. The next step is to extend the results to even more humanlike systems. The most important extension would be to go from 2D to 3D. From the research of the walking gait, it is known that this extension to 3D is difficult. One thing that makes this difficult is that in 3D compared to 2D many more states need to be controlled while the number of control outputs is not much larger. For example, to control the forward speed of a robot with foot placement in 2D, there are two control outputs available (step location and step time) to control a single quantity (forward speed). Where in 3D there are three control outputs (forward and sideways step location and step time) to control

two quantities (forward and sideways speed). A solution for this problem in walking is given in Appendix A.

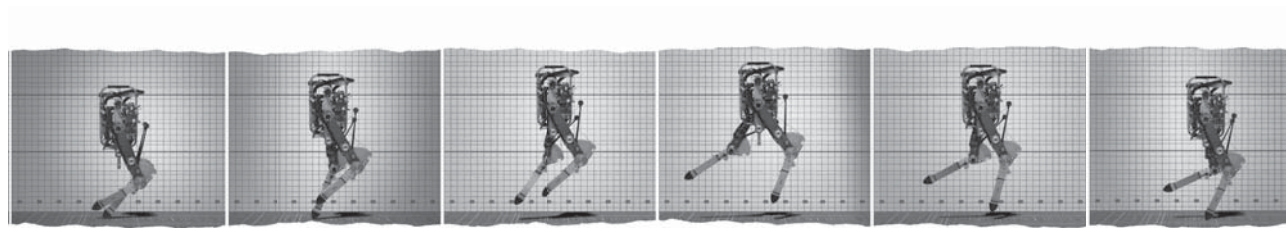
7.4.3 Applying

As discussed in Section 7.2.2, the results of this research can be useful for the development of orthoses and prostheses for running. Most promising is the implementation of nonlinear springs in exoskeletons, because the results show a large improvement in disturbance rejection and because nonlinear springs are relatively easy to implement in exoskeletons. In this case, the effect of nonlinear springs on the metabolic cost of running should be studied, as decreasing the metabolic cost is the goal of most exoskeletons.

A

Foot Placement control: Step Location and Step Time as a Function of the Desired Walking Gait

Tomas de Boer, J.G.Daniël Karssen, and Martijn Wisse,
Submitted to *Robotica*.



Abstract

We present a foot placement controller for walking bipedal robots, which outputs the appropriate step location and step time to obtain a desired walking gait from every feasible system state. The step location and step time are determined by approximating the robot dynamics with the 3D Linear Inverted Pendulum Model and analytically solving the constraint equations. The performance of the controller is tested in a simulation study. The results of this study show that the controller can get the system to a desired gait cycle from every feasible state within a finite number of steps.

A.1 Introduction

Generating a robust bipedal gait causes a difficult control problem. The center-of-mass velocity can be controlled by the center of pressure location, but the support polygon imposes a constraint on this location. Especially during single support, the support polygon is small, which results in a system that resembles a highly unstable inverted pendulum. For the system to remain stable, an appropriate new step has to be selected. This step determines possible future center of pressure locations. Consequently, deciding when and where to place a step is essential to control the center-of-mass and thereby obtain a robust walking gait.

Biomechanical studies found that stable step locations can be predicted based on simple inverted pendulum dynamics, and center-of-mass position and velocity information (Hof et al., 2005; Millard et al., 2009; Townsend, 1985). Pratt et al. (2006) expanded this finding to robotic control and introduced the *capture point*. The essence of this step indicator (or very similar ones (Hof et al., 2005; Wight et al., 2008)) is that stepping on the indicated point will allow the robot to come to a stop. The concept of the capture point is powerful and can be used to readily predict step regions for which the system has the ability to come to a stop or will inevitably fall (Koolen et al., 2012).

Using the capture point to generate walking gait is less straightforward, since this obviously requires a non-zero forward speed. Walking controllers that step a constant offset away from the capture point have been suggested (Hof, 2008; Kajita et al., 2001; Pratt et al., 2012; Wight, 2008). This “constant offset control” approach seems logical since stepping ahead or behind the indicated point will in general cause the legged system to decelerate or accelerate respectively. Several implementations

of this control approach were demonstrated (Coros et al., 2010; Kajita et al., 2001; Pratt et al., 2012; Wight et al., 2008).

However, the constant offset control approach has three significant shortcomings, which we will demonstrate in this chapter. These are: (1) The desired gait will only be reached in infinite time. This can be problematic because the system may not have recovered from a perturbation before a new perturbation occurs. (2) The controller will only work for a limited set of all feasible system states. This limits the ability to maintain stable in the presence of large perturbations. (3) The controller assumes a constant step time. This reduces the possible step strategies and therefore limits the control performance.

In this chapter, we will present a novel method that overcomes these shortcomings. We introduce a controller, which we will refer to as *Dynamic Foot Placement* controller, which gives a direct relation between the desired system state and the required step time and step location to reach that state within a finite number of steps. The controller is derived using the linear inverted pendulum model. The simple nature of this model results in simple control rules which allow for real-time implementation on a real robot. We will demonstrate the effectiveness of our proposed foot placement controller and show that the controller can be used to obtain a desired cyclic walking gait from any feasible system state.

To illustrate the performance of the Dynamic Foot Placement controller, a Matlab graphical user interface (GUI) was created. It allows the user to manipulate the state of the linear inverted pendulum model and the desired walking gait that should be obtained by the foot placement controller. The GUI can be downloaded on <http://dbl.tudelft.nl>.

This chapter is organized as follows. Section A.2 presents the model, followed by a description of the walking gait in Section A.3. A formal description of the intended control problem is given in Section A.4. Section A.5 describes the principle of operation of the Dynamic Foot Placement controller, followed by a comparison between the constant offset control approach and our proposed controller in Section A.6.

A.2 Model description

To obtain simple control strategies, we use a simple model to approximate the dynamics of a bipedal robot: the 3D Linear Inverted Pendulum Model as depicted in Figure A.1 (Kajita and Tani, 1991). This model is widely used to synthesize control strategies for bipedal robots (Kajita et al., 2001; Kajita and Tani, 1991) and to analyze human locomotion (Hof, 2008; Hof et al., 2005).

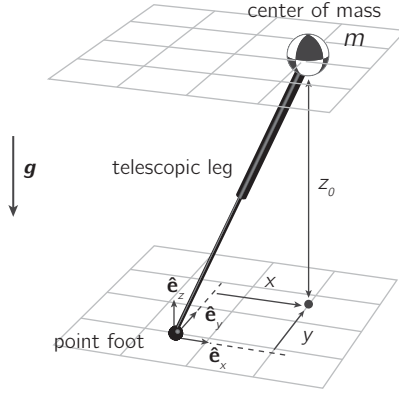


Figure A.1: Schematic representation of the 3D-LIPM (Kajita and Tani, 1991). The model comprises a point foot, a point mass with mass m at position (x, y, z) with respect to a local reference frame located at the point foot and a massless telescoping leg that keeps the point mass at the constant height $z = z_0$. The gravitational acceleration vector is $\mathbf{g} = (0, 0, -g)^T$. The state of the model is uniquely described by the set of state variables $\mathbf{q} = (x, y, \dot{x}, \dot{y})^T$.

The model comprises a point mass and a telescoping massless leg that is in contact with the ground. The extensible leg applies an appropriate force at the point mass to keep it at a constant height from the ground. The leg has a point foot, which can not apply torques on the ground.

A.2.1 Equations of motion

The state of the model is uniquely described by the set of state variables

$$\mathbf{q} = \begin{pmatrix} \mathbf{p} \\ \dot{\mathbf{p}} \end{pmatrix} \quad \text{with} \quad \mathbf{p} = \begin{pmatrix} x \\ y \end{pmatrix}, \quad (\text{A.1})$$

with x and y representing the position of the point mass with respect to a local reference frame located at the point foot. The dynamics of the model consist of one part that describes the stance phase and one part that describes the transition from one stance phase to the next. Figure A.2 shows the dynamics of the model in x -direction for an example walking motion that consists of two stance phases and two steps.

The stance phase dynamics are continuous and described by:

$$\ddot{\mathbf{p}} = \omega_0^2 \mathbf{p}, \quad (\text{A.2})$$

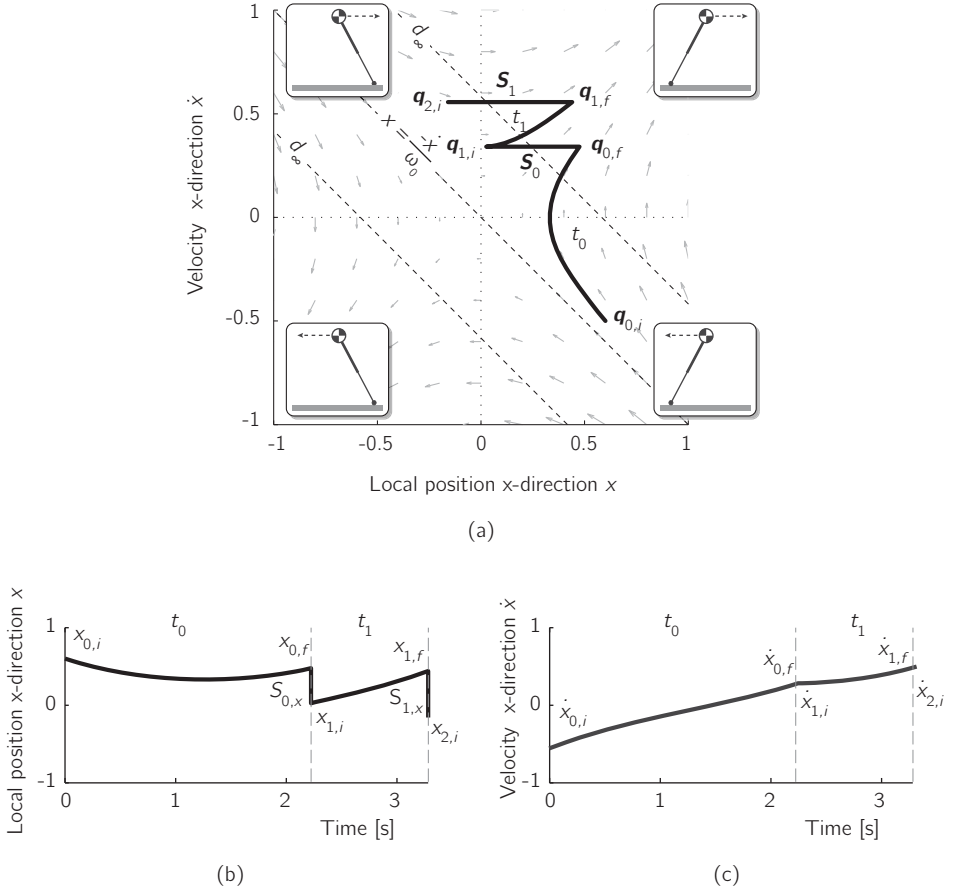


Figure A.2: Dynamics of the 3D-LIPM in x-direction (with g and z_0 of unit magnitude) for an example initial state $\mathbf{q} = (0.6, y, -0.5, \dot{y})^T$. The model's state is shown in state space in (a) and in the time domain in (b) and (c). For the state space plot, the boxed model pictures illustrate the model's configuration for the four quadrants of the plot. Continuous dynamics describe the evolution of initial state $\mathbf{q}_{0,i}$ to state $\mathbf{q}_{0,f}$ over time t_0 . The transition dynamics describe the instantaneous change of state $\mathbf{q}_{0,f}$ to state $\mathbf{q}_{1,i}$ due to step S_0 . This sequence is repeated for consecutive stance phases and steps. Any state that lies on the line $x = \frac{-\dot{x}}{\omega_0}$ will make the model come to a stop in x-direction, i.e., $\lim_{t \rightarrow \infty} \dot{x} = 0$ (i.e., the instantaneous capture point defined by Pratt et al., 2006). The model can only come to a stop for initial states $\mathbf{q}_{n,i}$ that lie inside the ∞ -step viable-capture basin (dashed lines labeled d_∞) due to the imposed stepping constraints, as described in Section A.2.2 (Koolen et al., 2012).

with $\omega_0 = \sqrt{\frac{g}{z_0}}$, for which g is the gravitational constant and z_0 the height of the point mass. Solving (A.2) results in a closed form solution for the stance phase dynamics,

$$\mathbf{p}_{n,f} = \mathbf{p}_{n,i} \cosh(\omega_0 t_n) + \frac{\dot{\mathbf{p}}_{n,i}}{\omega_0} \sinh(\omega_0 t_n) \quad (\text{A.3a})$$

$$\dot{\mathbf{p}}_{n,f} = \mathbf{p}_{n,i} \omega_0 \sinh(\omega_0 t_n) + \dot{\mathbf{p}}_{n,i} \cosh(\omega_0 t_n). \quad (\text{A.3b})$$

where t_n is the duration of the stance phase and subscript i and f refer to the initial and final model state respectively of a stance phase, which is indexed with subscript n , with $n \in \mathbb{N}_0$.

The transition dynamics are instantaneous and describe the changes in foot positions that occur when taking a step. It is assumed that a step has no instantaneous effect on the velocity of the point mass. The instantaneous state change is given by:

$$\mathbf{p}_{n+1,i} = \mathbf{p}_{n,f} - \mathbf{S}_n \quad (\text{A.4a})$$

$$\dot{\mathbf{p}}_{n+1,i} = \dot{\mathbf{p}}_{n,f}, \quad (\text{A.4b})$$

where $\mathbf{S}_n = (S_{n,x}, S_{n,y})^T$ describes the step size in x - and y -direction.

A.2.2 Stepping constraints

To model the limitations of a real robot, we impose two stepping constraints on the model as introduced by (Koolen et al., 2012). First, we model actuator saturation on a real robot by introducing a lower limit on the time between foot location changes:

$$t_n \geq t_{\min}. \quad (\text{A.5})$$

Second, we model the limited kinematic workspace of a real robot by introducing an upper limit on step length, i.e., the distance between subsequent point foot locations:

$$\|\mathbf{S}_n\| \leq l_{\max}. \quad (\text{A.6})$$

Due to these constraints, the model can only operate in a subset of the state space. The subset consist of all states for which the model has the ability to come to a stop. For states outside of this subset the model will accelerate without the possibility to decelerate. The subset is spanned by model states $\mathbf{q}_{n,i}$ that lie within the ∞ -step viable-capture basin as introduced in (Koolen et al., 2012) and is given by

$$\left\| \mathbf{p}_i + \frac{\dot{\mathbf{p}}_i}{\omega_0} \right\| < \frac{l_{\max}}{e^{\omega_0 t_{\min}} - 1} = d_{\infty}. \quad (\text{A.7})$$

In Figure A.2, the basin boundary is indicated by the dashed lines labeled d_{∞} .

A.3 Walking gait

Our proposed foot placement controller has the ability to bring the model to any desired feasible state. In this chapter, we select a more practical application of the controller by bringing the model to a state that is part of a desired walking gait. This requires that the model should not only arrive at the desired state, but should also be capable of maintaining the desired gait cycle. This requires a passed minimum step time when the gait cycle requires another step to be taken.

The desired gait cycle is set to a humanlike two-step cyclic gait with an alternating left and right step. If the model has obtained the desired gait cycle, then

$$\mathbf{q}^* = \mathbf{q}_{n+2} = \mathbf{q}_n, \quad (\text{A.8})$$

with corresponding step time $t^* = t_{n+2} = t_n$. The step size of the desired gait cycle is,

$$\mathbf{S}_n = \begin{pmatrix} S_x^* \\ S_y^*(-1)^n \end{pmatrix}, \quad (\text{A.9})$$

with x and y being the forward and lateral direction of movement respectively.

The control objective is a desired state within the gait cycle. For this chapter, we select the state at the end of the stance phase as a reference state within the gait cycle:

$$\mathbf{q}_f^* = \begin{pmatrix} x_f^* \\ y_f^* \\ \dot{x}_f^* \\ \dot{y}_f^* \end{pmatrix} = \begin{pmatrix} \frac{1}{2}S_x^* \\ \frac{1}{2}S_y^*(-1)^n \\ \frac{1}{2}\omega_0 S_x^* \coth(\frac{1}{2}\omega_0 t^*) \\ \frac{1}{2}\omega_0 S_y^* \tanh(\frac{1}{2}\omega_0 t^*)(-1)^n \end{pmatrix}. \quad (\text{A.10})$$

For all figures throughout this chapter, we use an example desired gait cycle, which is depicted in Figure A.3. For this gait cycle $t^* = 1.5$, $S_x^* = 0.75$ and $S_y^* = 0.3$. These three parameters uniquely describe the gait cycle and set the average forward velocity to $S_x^*/t^* = 0.5$. We set the model parameters g , z_0 , l_{\max} and t_{\min} to unit magnitude.

A.4 Control problem

To let the model reach the desired state \mathbf{q}_f^* within the gait cycle, the controller can adjust the step time t_n as well as the step location $S_{n,x}$ and $S_{n,y}$ over a finite number of N steps, while satisfying the stepping constraints (Section A.2.2). This results in

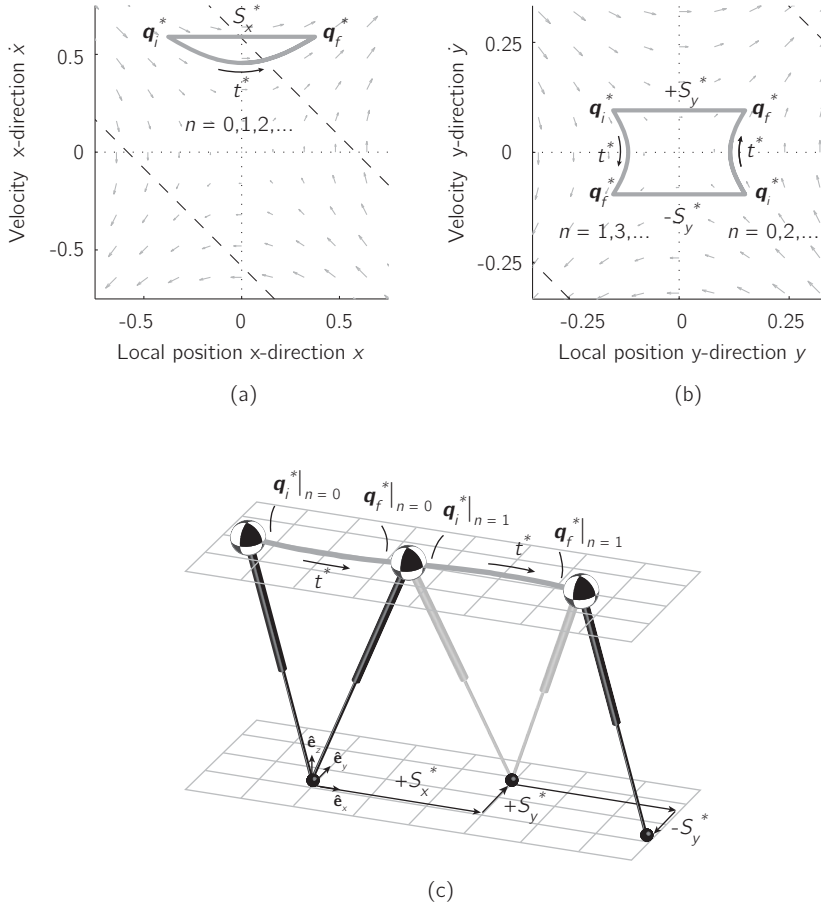


Figure A.3: Example two-step gait cycle for the 3D-LIPM. The gait cycle is described by $\mathbf{S}^* = (0.75, 0.3)^T$, $t^* = 1.5$. (a) State space in x . (b) State space in y . (c) 3D global representation of the evolution of the model state.

the following formal description of the control problem:

$$f(\mathbf{q}_{0,i}, t_0, \dots, t_N, \mathbf{S}_0, \dots, \mathbf{S}_{N-1}) = \mathbf{q}_f^* \quad (\text{A.11a})$$

$$t_n \geq t_{\min} \quad \text{for } n = 0 \dots N \quad (\text{A.11b})$$

$$\|\mathbf{S}_n\| \leq l_{\max} \quad \text{for } n = 0 \dots N-1 \quad (\text{A.11c})$$

in which function f gives the state of the system after the N th step. This function can be derived from (A.3) and (A.4) and is given by:

$$f(\mathbf{q}_{0,i}, t_0, \dots, t_N, \mathbf{S}_0, \dots, \mathbf{S}_{N-1}) = \begin{pmatrix} \mathbf{p}_{0,i} \cosh(\omega_0 T(N)) + \frac{\dot{\mathbf{p}}_{0,i}}{\omega_0} \sinh(\omega_0 T(N)) \\ - \sum_{i=0}^{N-1} \mathbf{S}_i \cosh(\omega_0 (T(N) - T(i))) \\ \mathbf{p}_{0,i} \omega_0 \sinh(\omega_0 T(N)) + \dot{\mathbf{p}}_{0,i} \cosh(\omega_0 T(N)) \\ - \sum_{i=0}^{N-1} \mathbf{S}_i \omega_0 \sinh(\omega_0 (T(N) - T(i))) \end{pmatrix} \quad \text{with } T(i) = \sum_{n=0}^i t_n. \quad (\text{A.12})$$

There are many combinations of step locations, step sizes, and total number of steps for which the model will reach the desired gait cycle. We have chosen an approach where we minimize the required number of steps, for two reasons. First, because in case of a disturbance, it is beneficial to quickly return to the desired gait cycle in a small number of steps in order to withstand a possible new disturbance. Second, making a step is potentially costly. Using many steps may be disadvantageous from an energetic point of view and always involves risk: any step can be misplaced.

Finding a controller that satisfies the control problem (A.11) for a minimal number of steps N can be done using numerical optimization methods. However, the non-deterministic nature of these optimization methods makes it unattractive for real-time implementation on a robot.

Therefore, we adopt a different approach to synthesize a foot placement controller. We start by checking if there is a solution to the control problem for $N = 0$. If there is no solution, we repeat the procedure after an incremental increase of N . For each N , the problem that needs to be solved is different, since N determines the number of free (control) parameters and constraints (see Table A.1). For example, a 1-step strategy has four free parameters and four equality constraints making this a fully constrained problem.

In the next section, we will show that our approach leads to an overall foot placement controller that consists of multiple simple closed-form solutions. The proposed controller solves the control problem for any number of steps.

Table A.1: Parameters and constraints for different number of steps.

	0-step	1-step	2-step	N-step
Free parameters				
total number	1	4	7	$3N + 1$
in t	t_0	t_0, t_1	t_0, t_1, t_2	t_0, \dots, t_N
in S	-	S_0	S_0, S_1	S_0, \dots, S_{N-1}
Equality constraints				
total number	4	4	4	4
in f	$f() = q_f^*$	$f() = q_f^*$	$f() = q_f^*$	$f() = q_f^*$
Inequality constraints				
number	1	3	5	$2N + 1$
in t	$t_n \geq t_{\min}$	$t_n \geq t_{\min}$	$t_n \geq t_{\min}$	$t_n \geq t_{\min}$
in S	-	$\ S_n\ \leq l_{\max}$	$\ S_n\ \leq l_{\max}$	$\ S_n\ \leq l_{\max}$
Problem				
type	over- constrained	fully constrained	under- constrained	-

A.5 Dynamic Foot Placement controller

The Dynamic Foot Placement controller outputs the next step location and step time, expressed in terms of the control parameters $S_{x,n}$, $S_{y,n}$ and t_n . We will derive expressions for these control parameters for each initial model state. The foot placement controller consists of four N -step strategies with $N = 0, 1, 2, (N > 2)$. Each N -step strategy will result in an $(N - 1)$ -step strategy up to a 0-step strategy, as demonstrated for an example 3-step strategy in Figure A.4.

A.5.1 0-step strategy

If the initial state is already on the gait cycle or will arrive at the gait cycle without taking a step, then the following should hold:

$$\mathbf{q}_{0,f} = \mathbf{q}_f^* \quad \wedge \quad t_0 \geq t_{\min}. \quad (\text{A.13})$$

The control parameters are then given by $S_{0,x} = S_x^*$, $S_{0,y} = S_y^*$ and

$$t_0 = \omega_0^{-1} \log \left(\frac{\dot{x}_f^* + \sqrt{\dot{x}_f^{*2} + \omega_0^2 x_{0,i}^2 - \dot{x}_{0,i}^2}}{\omega_0 x_{0,i} + \dot{x}_{0,i}} \right), \quad (\text{A.14})$$

which is found by solving (A.13) for t in which $\mathbf{q}_{0,f}$ is given by (A.3).

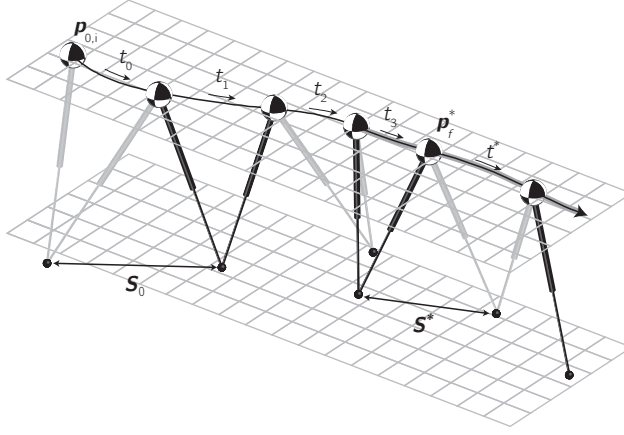
A.5.2 1-step strategy

The 1-step strategy is fully constrained (Table A.1), which means that a unique solution exists for the control parameters $S_{x,0}$, $S_{y,0}$, t_0 and t_1 . To derive an expression for these parameters it is important to acknowledge the following: since a step has no instantaneous effect on the model velocities, we know that the velocities in the x - and y -direction at the moment of the step should match the velocities of the desired gait cycle at some instant of the gait.

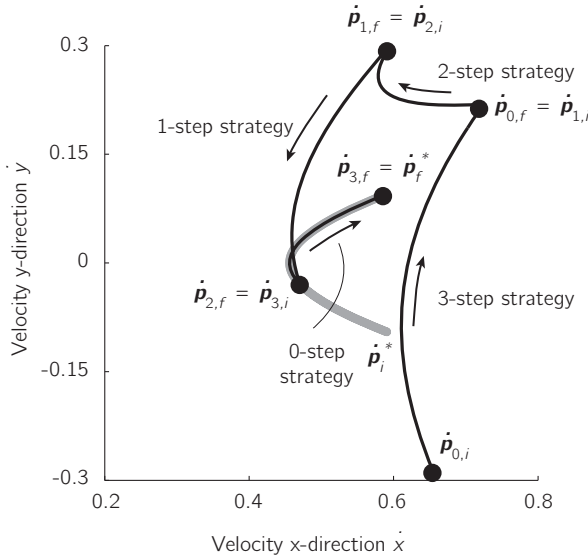
To further clarify this fact, let us consider the model velocities $\dot{\mathbf{p}}$ shown in the phase space diagram depicted in Figure A.4b. Here, we see a 1-step strategy that is part of a 3-step strategy. We see that, going from a 1-step strategy to a 0-step strategy, the phase space trajectory of the model velocities intersects the phase space trajectory of the possible gait-cycle velocities. At the instant that the velocities match, a step is taken and the model evolves to the state \mathbf{q}_f^* .

Consequently, for a 1-step strategy to be feasible, an intersection $\dot{\mathbf{p}}_{0,f} = \dot{\mathbf{p}}_{1,i}$ should occur. This means that the following expression, based on (A.3b), should hold,

$$\mathbf{p}_{0,i} \omega_0 \sinh(\omega_0 t_0) + \dot{\mathbf{p}}_{0,i} \cosh(\omega_0 t_0) = \mathbf{p}_f^* \omega_0 \sinh(\omega_0 (-t_1)) + \dot{\mathbf{p}}_f^* \cosh(\omega_0 (-t_1)). \quad (\text{A.15})$$



(a)



(b)

Figure A.4: Example 3-step strategy of the model in initial state $\dot{\mathbf{q}}_{0,i}$ to the desired state $\dot{\mathbf{q}}_f^*$ part of the desired gait cycle (highlighted by the thick grey line). The initial state is $\dot{\mathbf{q}}_{0,i} = (-0.25, 0.58, 0.65, -0.30)^T$. All step constraints described in Section A.2.2 are satisfied. (a) 3D global representation of the evolution of state component \mathbf{p} . (b) The evolution of the velocities in x- and y-direction, i.e., state component $\dot{\mathbf{p}}$. Black dots indicate the states just after a step.

This expression can be solved to find the stance phase durations t_0 and t_1 . We omit the expressions for t_0 and t_1 because of their length.

With the known stance phase durations t_0 and t_1 , we can also derive the expression for the step size S_0 from (A.3a) and (A.4a),

$$\begin{aligned} S_0 &= p_{0,f} - p_{1,i}, & \text{with} & & (A.16) \\ p_{0,f} &= p_{0,i} \cosh(\omega_0 t_0) + \frac{\dot{p}_{0,i}}{\omega_0} \sinh(\omega_0 t_0) \\ p_{1,i} &= p_f^* \cosh(-\omega_0 t_1) + \frac{\dot{p}_f^*}{\omega_0} \sinh(-\omega_0 t_1). \end{aligned}$$

The last part of the 1-step strategy is to check if the found step durations t_0 and t_1 and step size S_0 are within the stepping constraints, (A.5) and (A.6). If this is not the case, the 2-step strategy should be considered.

A.5.3 2-step strategy

A 2-step strategy is underconstrained (Table A.1), meaning that multiple solutions can exist for the available control parameters S_0 , S_1 and stance durations t_0 , t_1 and t_2 . The constraint equation (A.12) in case of a 2-step strategy becomes

$$f(q_{0,i}, t_0, t_1, t_2, S_0, S_1) = q_f^*. \quad (A.17)$$

Solving (A.17) for S_0 , S_1 results in

$$\begin{aligned} S_0 &= - \left(\frac{\dot{p}_{0,i}}{\omega_0} \cosh(\omega_0 (t_0 + t_1)) + p_{0,i} \sinh(\omega_0 (t_0 + t_1)) \right. \\ &\quad \left. - \frac{\dot{p}_f^*}{\omega_0} \cosh(\omega_0 t_2) + p_f^* \sinh(\omega_0 t_2) \right) \frac{1}{\sinh(\omega_0 t_1)} \end{aligned} \quad (A.18)$$

$$\begin{aligned} S_1 &= \left(- \frac{\dot{p}_f^*}{\omega_0} \cosh(\omega_0 (t_1 + t_2)) + p_f^* \sinh(\omega_0 (t_1 + t_2)) \right. \\ &\quad \left. + \frac{\dot{p}_{0,i}}{\omega_0} \cosh(\omega_0 t_0) + p_{0,i} \sinh(\omega_0 t_0) \right) \frac{1}{\sinh(\omega_0 t_1)}. \end{aligned} \quad (A.19)$$

We can set three of the seven free control parameters (Table A.1) and thereby derive a value for all parameters. An example option would be to set all stance durations t_0 , t_1 and t_2 to t_{\min} , which we have done for the visualization of the control performance in Section A.6. Though this approach might result in a stepping strategy that does not use the absolute minimum number of steps for some model states, Section A.6 demonstrates that the overall performance of the controller is still close to optimal.

A.5.4 ($N > 2$)-step strategy

For all model states that cannot evolve to the gait cycle using N -step strategies for $N \leq 2$, we adopt a single step strategy. Though more suited stepping strategies for $N > 2$ can be derived, these were found to be complex and result in a negligible increase in stepping performance.

The model state should quickly be brought to a region in state space for which N -step strategies for $N \leq 2$ do apply, consequently t_n is set to t_{\min} . A corresponding effective step location is a point at an offset from the instantaneous capture point (Pratt et al., 2006) and was introduced as part of the constant offset controller, explained in (Hof, 2008):

$$\mathbf{s}_n = \mathbf{p} + \frac{\dot{\mathbf{p}}}{\omega_0} + \begin{pmatrix} \frac{-S_x^*}{e^{\omega_0 t_n^*} - 1} \\ \frac{S_y^* (-1)^n}{e^{\omega_0 t_n^*} + 1} \end{pmatrix}. \quad (\text{A.20})$$

If this point is not within reach due to stepping constraints, we step on the instantaneous capture point or maximally towards this point if it is also out of reach.

A.6 Control performance

In the previous section, we introduced the Dynamic Foot Placement controller. In this section, we discuss the performance of this controller. The performance is discussed in terms of the numbers of steps it takes to reach the desired gait cycle (Section A.6.1) and the time response (Section A.6.2).

A.6.1 Number of steps

The goal of the Dynamic Foot Placement controller is to get the model to the desired gait cycle from every possible initial state with the least number of steps. We check how well the controller reaches this goal by comparing the required number of steps to the absolute minimal number of steps required. The numerical method used to determine the absolute minimal number of steps is explained in the appendix. We show the results for the special case of 2D walking, in which $S_y^* = 0$, $y = 0$ and $\dot{y} = 0$. We use this special case, because for this case the results can easily be visualized in a graph, since the state space is only 2-dimensional instead of 4-dimensional for the case of 3D walking.

Figure A.5c shows the absolute minimal number of steps needed to get to the desired gait cycle for a set of initial states. It shows that it is possible to get to the desired gait cycle from all initial states within the ∞ -step viable-capture basin. Figures

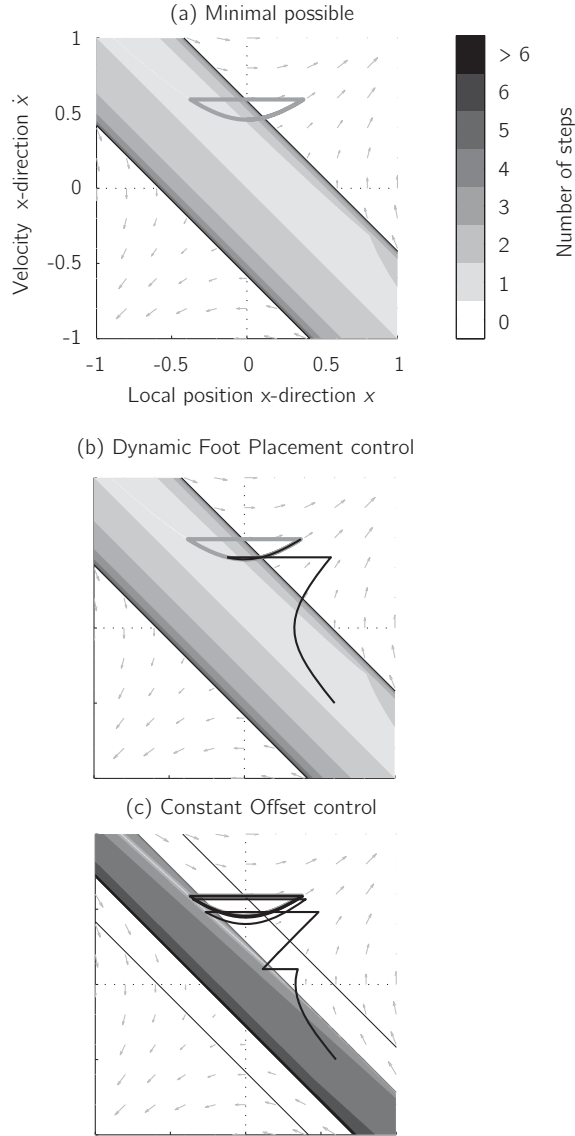


Figure A.5: State space in the x-direction with the number of steps it takes to reach the desired gait cycle as a function of the initial state. The desired gait cycle is highlighted by the thick grey lines. (a) shows the absolute minimal number of steps it takes to reach the desired gait cycle. (b) and (c) show the number of steps takes for respectively the Dynamic Foot Placement controller and the constant offset controller. For constant offset controller, we define that the gait cycle is reached as the difference with the gait cycle is less than 10^{-3} . The black line in (b) and (c) is an example path for both controllers with an initial state $(x_i, \dot{x}_i) = (0.6, -0.5)$.

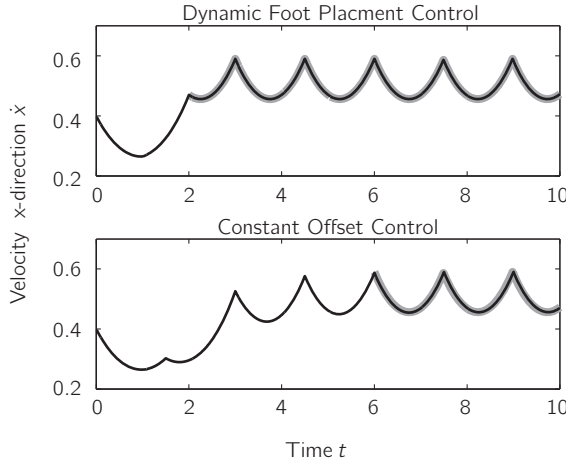


Figure A.6: The convergence of the velocity in x-direction to the desired limit cycle for the Dynamic Foot Placement controller and the constant offset controller. The desired gait cycle is indicated by the thick grey lines.

A.5b and A.5c show the number of steps that it takes to get to the desired gait cycle for respectively the Dynamic Foot Placement controller and the constant offset controller. The number of steps for the Dynamic Foot Placement controller is almost equal to the absolute minimal number of steps. Only for initial states close to the lower d_∞ boundary, the number of steps is one higher for some initial conditions. The number of steps of the constant offset controller is in theory infinite since the convergence is asymptotical. However for this test, we assume that the gait cycle is reached when the difference with the gait cycle is less than 10^{-3} . With this assumption, the number of steps for the constant offset controller is still much higher than the minimal number of steps. In addition, there is a large range of initial states that are within the ∞ -step viable-capture basin, but do not reach the desired gait cycle using the constant offset controller.

A.6.2 Time response

Figure A.6 shows an example of how the velocity in x-direction evolves to the desired gait cycle from a disturbed state for both the Dynamic Foot Placement controller and the constant offset controller. The velocity in x-direction is representative for all the four state variables in \mathbf{q} . For the Dynamic Foot Placement controller, the state evolves to the desired gait cycle within a finite number of steps. For the constant offset controller, the state converges asymptotically to the desired gait cycle. This means that the gait cycle will only be reached if time goes to infinity.

A.7 Discussion

The goal of this study is to synthesize a general foot placement controller, which can predict an appropriate step location and step time that will bring a bipedal robot to any desired gait cycle in a minimal number of steps. To arrive at comprehensible control strategies, we used a simple gait model and adopted an incremental approach to solve the control problem. The use of this approach and the model has its benefits but also introduces some limitations.

Incrementally solving the control problem for different N allowed us to derive closed-form expressions for the control parameters. These expressions give direct insight in the relation between the walking objective (in this case a desired walking gait in a minimal number of steps) and the foot placement control (step time and step location) that is required to reach this objective. We demonstrated that a total of only four step strategies was required to effectively bring the model to the desired gait cycle from any feasible model state.

Another benefit from this approach is that the walking objective does not have to be a gait cycle per se. A high-level controller can use the Dynamic Foot Placement controller to track a desired gait pattern, which could include reaching a standstill, changing the walking speed (Figure A.7), making a turn (Figure A.8) or reaching

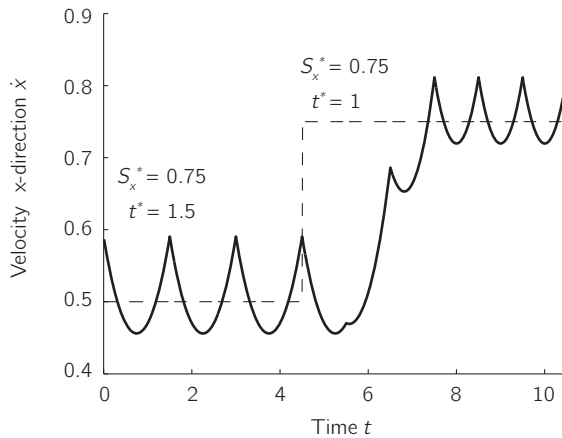


Figure A.7: Simulation results of a change in walking speed using the Dynamic Foot Placement controller. A speed change is achieved by changing the desired gait parameters. For the depicted speed change, the desired speed S_x^*/t^* is changed from 0.5 to 0.75. The new desired speed is reached within three steps after the desired speed change.

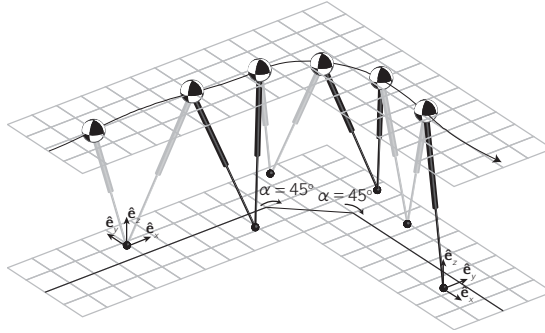


Figure A.8: Simulation results of a change in walking direction using the Dynamic Foot Placement controller. A change in walking direction is achieved by rotating the local coordinate frame in the x - y plane over an angle α . The depicted 90° turn is in this case achieved by rotating the coordinate frame over 45° after the first step and again 45° after the second step.

any other desired system state.

A limitation of the approach is that we optimized our controller to a minimum number of steps, though other optimization criteria might also be relevant. Other relevant optimization criteria could be, for example, minimization of the time required to reach the state or minimization of the amount of mechanical work required by the actuators. In the near future, we plan to study how the foot placement strategies are influenced by the selected optimization criterion or by combinations of criteria.

Though the 3D-LIPM enabled us to derive these simple stepping strategies, it is a very simplistic representation of a real robot. By modeling only center-of-mass dynamics and not taking impact dynamics into account, we neglect many dynamic aspects of true dynamic walking. However, we believe it can be successfully applied to control a complex biped robot, similar to the successful application of the 3D-LIPM in the walking and balancing algorithms of the twelve-degree-of-freedom biped robot M2V2 (Pratt et al., 2012). It should not be attempted to forcefully mimic the 3D-LIPM dynamics on the complex biped, as is typically done for ‘Zero Moment Point’-based control approaches (Kajita et al., 2003). The evolution of the complex biped will inevitably deviate from the evolution that is predicted by the simple model. The simple nature of Dynamic Foot Placement controller allows for real-time execution on the robot, which allows the controller to continuously adapt to the current state of the robot. The output of the Dynamic Foot Placement controller can be used as an approximation for an adequate step time and step location for the real robot. Biomechanical studies (Hof et al., 2005, 2010) have shown that such simple foot placement approximations, based on simple inverted pendulum models, show good

correlation with human foot placement strategies.

A.8 Conclusion

In this chapter, we presented the Dynamic Foot Placement controller: a controller that outputs the next step location and step time based on the desired gait cycle and the current state of the system. We investigated the performance of this controller in a simulation study and shown that it can get the model to a desired gait cycle from every feasible state within a finite number of steps. In addition, we compared the performance of the Dynamic Foot Placement controller to the frequently used constant offset controller. We showed that the Dynamic Foot Placement controller outperforms the constant offset controller, in both the number of steps it takes to reach the desired gait as well as the size of the region in state space for which it can reach the desired gait.

Appendix

Minimal number of steps

Figure A.5a shows the absolute minimal number of steps it takes to reach the desired cyclic gait. In this section, we describe the numerical method used to determine the absolute minimal number of steps. The method determines iteratively the set of states A_N for which it is possible to reach the desired gait cycle within N steps based on the set A_{N-1} . Two steps are taken to get A_N from A_{N-1} . First, set A_{N-1} is expanded to B_N by adding all states that can reach A_{N-1} by making a step with a step size smaller or equal than the maximal step size l_{\max} . Next, A_N is determined as all states that will reach a state in set B_N with $t \geq t_{\min}$. The first set B_0 is equal to the final state in gait cycle q_f^* . In pseudocode this process looks as follows:

```

for  $N = 0$  to maximal number of steps do
  if  $N = 0$  then
     $B_N \leftarrow \{q_f^*\}$ 
  else
     $B_N \leftarrow \{q : q - (S^T, 0, 0)^T \in A_{N-1} \text{ with } \|S\| \leq l_{\max}\}$ 
  end if
   $A_N \leftarrow \{q : g(q, t) \in B_N \text{ with } t \geq t_{\min}\}$ 
end for

```

in which $g()$ represents the stance phase dynamics as given in (A.3).

References

- Ahmadi, M. and Buehler, M. (2006). “Controlled passive dynamic running experiments with the arl-monopod ii”. *IEEE Transactions on Robotics*, 22(5), pp. 974–986.
- Alexander, R. (1988). “Elastic mechanisms in animal movement”. Cambridge University Press Cambridge.
- Anderson, D.E., Madigan, M.L., and Nussbaum, M.A. (2007). “Maximum voluntary joint torque as a function of joint angle and angular velocity: Model development and application to the lower limb”. *Journal of Biomechanics*, 40(14), pp. 3105–3113.
- Andrews, B., Miller, B., Schmitt, J., and Clark, J.E. (2011). “Running over unknown rough terrain with a one-legged planar robot”. *Bioinspiration & Biomimetics*, 6, p. 026009.
- Asano, F. (2009). “Effects of swing-leg retraction and mass distribution on energy-loss coefficient in limit cycle walking”. *Proceedings of IEEE/RSJ International Conference on Intelligent Robots and Systems*, pp. 3214–3219.
- Benson, D.A., Huntington, G.T., Thorvaldsen, T.P., and Rao, A.V. (2006). “Direct trajectory optimization and costate estimation via an orthogonal collocation method”. *Journal of Guidance Control and Dynamics*, 29(6), pp. 1435–1440.
- Blanchard, B., Verma, D., and Peterson, E. (1995). “Maintainability: A key to effective serviceability and maintenance management”, volume 13. Wiley-Interscience.
- Blickhan, R. (1989). “The spring-mass model for running and hopping”. *Journal of biomechanics*, 22(11), pp. 1217–1227.
- Blickhan, R. and Full, R.J. (1993). “Similarity in multilegged locomotion: Bouncing like a monopode”. *Journal of Comparative Physiology A: Neuroethology, Sensory, Neural, and Behavioral Physiology*, 173(5), pp. 509–517.
- Blum, Y., Lipfert, S.W., Rummel, J., and Seyfarth, A. (2010). “Swing leg control in human running”. *Bioinspiration & Biomimetics*, 5, p. 026006.
- Boer, T. de (2012). “Foot placement in robotic bipedal locomotion”. Phd thesis, Delft University of Technology.
- Cavagna, G.A., Heglund, N.C., and Taylor, C.R. (1977). “Mechanical work in terrestrial locomotion: two basic mechanisms for minimizing energy expenditure”.

- American Journal of Physiology- Regulatory, Integrative and Comparative Physiology, 233(5), p. 243.
- Cherouvim, N. and Papadopoulos, E. (2005). *"Single actuator control analysis of a planar 3dof hopping robot"*. Proceedings of Robotics: science and systems I, pp. 145–152.
- Chevallereau, C., Westervelt, E.R., and Grizzle, J.W. (2005). *"Asymptotically stable running for a five-link, four-actuator, planar bipedal robot"*. The International Journal of Robotics Research, 24(6), p. 431.
- Cho, B.K., Kim, J.H., and Oh, J.H. (2011). *"Online balance controllers for a hopping and running humanoid robot"*. Advanced Robotics, 25, 9(10), pp. 1209–1225.
- Collins, S., Ruina, A., Tedrake, R., and Wisse, M. (2005). *"Efficient bipedal robots based on passive-dynamic walkers"*. Science, 307(5712), pp. 1082–1085.
- Coros, S., Beaudoin, P., and Panne, M. van de (2010). *"Generalized biped walking control"*. Proceedings of SIGGRAPH, pp. 1–9.
- Daley, M.A. and Usherwood, J.R. (2010). *"Two explanations for the compliant running paradox: reduced work of bouncing viscera and increased stability in uneven terrain"*. Biology Letters, 6(3), pp. 418–421.
- Delft Biorobotics Lab (2012). *"Website Delft Biorobotics Lab"*. URL <http://dbi.tudelft.nl>.
- Elliott, G.G.A. (2012). *"Design and evaluation of a quasi-passive robotic knee brace: on the effects of parallel elasticity on human running"*. Ph.D. thesis, Massachusetts Institute of Technology.
- Ernst, M., Geyer, H., and Blickhan, R. (2009). *"Spring-legged locomotion on uneven ground: A control approach to keep the running speed constant"*. International Conference on Climbing and Walking Robots, pp. 639–644.
- Full, R.J. and Koditschek, D.E. (1999). *"Templates and anchors: neuromechanical hypotheses of legged locomotion on land"*. Journal of Experimental Biology, 202(23), pp. 3325–3332.
- Garg, D., Patterson, M., Hager, W.W., Rao, A.V., Benson, D., and Huntington, G. (2010). *"A unified framework for the numerical solution of optimal control problems using pseudospectral methods"*. Automatica, 46(11), pp. 1843–1851.
- Garg, D., Patterson, M.A., Francolin, C., Darby, C.L., Huntington, G.T., Hager, W.W., and Rao, A.V. (2011). *"Direct trajectory optimization and costate estimation of finite-horizon and infinite-horizon optimal control problems using a radau*

- pseudospectral method*". Computational Optimization and Applications, 49(2), pp. 335–358.
- Ghigliazza, R.M., Altendorfer, R., Holmes, P., and Koditschek, D. (2005). "A simply stabilized running model". SIAM Review, 47(3), pp. 519–549.
- Grabowski, A.M. and Herr, H.M. (2009). "Leg exoskeleton reduces the metabolic cost of human hopping". Journal of Applied Physiology, 107(3), pp. 670–678.
- Gregorio, P., Ahmadi, M., and Buehler, M. (1997). "Design, control, and energetics of an electrically actuated legged robot". IEEE Transactions on Systems, Man, and Cybernetics, Part B, 27(4), pp. 626–634.
- Grizzle, J.W. (2012). "Youtube channel dynamic leg locomotion". URL <http://www.youtube.com/user/DynamicLegLocomotion>.
- Grizzle, J.W., Hurst, J., Morris, B., Park, H.W., and Sreenath, K. (2009). "Mabel, a new robotic bipedal walker and runner". Proceedings of the American Control Conference, pp. 2030–2036.
- Haberland, M., Karssen, J.G.D., Kim, S., and Wisse, M. (2011). "The effect of swing leg retraction on running energy efficiency". Proceedings of IEEE/RSJ International Conference on Intelligent Robots and Systems, pp. 3957–3962.
- He, J.P., Kram, R., and McMahon, T.A. (1991). "Mechanics of running under simulated low gravity". Journal of Applied Physiology, 71(3), pp. 863–870.
- Hirose, M. and Ogawa, K. (2007). "Honda humanoid robots development". Philosophical Transactions of the Royal Society A: Mathematical, Physical and Engineering Sciences, 365(1850), pp. 11–19.
- Hobbelen, D.G.E. (2008). "Limit cycle walking". Phd thesis, Delft University of Technology.
- Hobbelen, D.G.E. and Wisse, M. (2007a). "A disturbance rejection measure for limit cycle walkers: the gait sensitivity norm". IEEE Transactions on Robotics, 23(6), pp. 1213–1224.
- Hobbelen, D.G.E. and Wisse, M. (2007b). "Limit cycle walking". Humanoid Robots, Human-like Machines.
- Hobbelen, D.G.E. and Wisse, M. (2008). "Swing-leg retraction for limit cycle walkers improves disturbance rejection". IEEE Transactions on Robotics, 24(2), pp. 377–389.
- Hodgins, J., Koechling, J., and Raibert, M. (1986). "Running experiments with a

- planar biped*". International Symposium on Robotics Research.
- Hodgins, J.K. and Raibert, M.N. (1991). "*Adjusting step length for rough terrain locomotion*". IEEE Transactions on Robotics and Automation, 7(3), pp. 289–298.
- Hof, A.L. (2008). "*The 'extrapolated center of mass' concept suggests a simple control of balance in walking*". Human Movement Science, 27(1), pp. 112–125.
- Hof, A.L., Gazendam, M.G.J., and Sinke, W.E. (2005). "*The condition for dynamic stability*". Journal of Biomechanics, 38(1), pp. 1–8.
- Hof, A.L., Vermerris, S.M., and Gjaltema, W.A. (2010). "*Balance responses to lateral perturbations in human treadmill walking*". Journal of Experimental Biology, 213, pp. 2655–2664.
- Honda (2012). "*Asimo by Honda*". URL <http://asimo.honda.com>.
- Hosoda, K., Takuma, T., and Nakamoto, A. (2006). "*Design and control of 2d biped that can walk and run with pneumatic artificial muscles*". Proceedings of IEEE-RAS International Conference on Humanoid Robots, pp. 284–289.
- Hürmüzlü, Y. and Moskowitz, G.D. (1986). "*The role of impact in the stability of bipedal locomotion*". Dynamical Systems, 1(3), pp. 217–234.
- Hurst, J., Chestnutt, J., and Rizzi, A. (2007). "*Design and philosophy of the bi-masc, a highly dynamic biped*". Proceedings of IEEE International Conference on Robotics and Automation, pp. 1863–1868.
- Hurst, J.W. and Rizzi, A.A. (2008). "*Series compliance for an efficient running gait*". IEEE Robotics & Automation Magazine, 15(3), pp. 42–51.
- Hutter, M., Remy, C.D., Hoepflinger, M.A., and Siegwart, R. (2011). "*Scarleth: Design and control of a planar running robot*". Proceedings of IEEE/RSJ International Conference on Intelligent Robots and Systems, pp. 562–567.
- Hyon, S.H. and Mita, T. (2002). "*Development of a biologically inspired hopping robot-kenken*". Proceedings of IEEE International Conference on Robotics and Automation, volume 4, pp. 3984–3991.
- Jindrich, D.L. et al. (2002). "*Dynamic stabilization of rapid hexapedal locomotion*". Journal of Experimental Biology, 205(18), pp. 2803–2823.
- Kajita, S., Kanehiro, F., Kaneko, K., Fujiwara, K., Harada, K., Yokoi, K., and Hirukawa, H. (2003). "*Biped walking pattern generation by using preview control of zero-moment point*". Proceedings of IEEE International Conference on Robotics and Automation, pp. 1620–1626.

- Kajita, S., Kanehiro, F., Kaneko, K., Yokoi, K., and Hirukawa, H. (2001). “*The 3d linear inverted pendulum mode: A simple modeling for a biped walking pattern generation*”. Proceedings of IEEE/RSJ International Conference on Intelligent Robots and Systems, volume 1, pp. 239–246.
- Kajita, S., Nagasaki, T., Kaneko, K., Yokoi, K., and Tanie, K. (2005). “*A running controller of humanoid biped hrp-2lr*”. Proceedings of IEEE International Conference on Robotics and Automation, pp. 616 – 622.
- Kajita, S. and Tani, K. (1991). “*Study of dynamic biped locomotion on rugged terrain—derivation and application of the linear inverted pendulum mode—*”. Proceedings of IEEE International Conference on Robotics and Automation, volume 2, pp. 1405–1411.
- Karssen, J.G.D., Haberland, M., Wisse, M., and Kim, S. (2011). “*The optimal swing-leg retraction rate for running*”. Proceedings of IEEE International Conference on Robotics and Automation, pp. 4000–4006.
- Kim, S., Clark, J.E., and Cutkosky, M.R. (2006). “*isprawl: Design and tuning for high-speed autonomous open-loop running*”. The International Journal of Robotics Research, 25(9), pp. 903–912.
- Knox, B.T. (2008). “*Design of a biped robot capable of dynamic maneuvers*”. Master’s thesis, Ohio State University.
- Koolen, T., Boer, T. de, Rebula, J., Goswami, A., and Pratt, J. (2012). “*Capturability-based analysis and control of legged locomotion, part 1: Theory and application to three simple gait models*”. The International Journal of Robotics Research, 31(9), pp. 1094–1113.
- Leva, P. de (1996). “*Adjustments to zatsiorsky-seluyanov’s segment inertia parameters*”. Journal of biomechanics, 29(9), pp. 1223–1230.
- Linde, R.Q. van der (2001). “*Bipedal walking with active springs, gait synthesis and prototype design*”. Ph.D. thesis, Delft University of Technology, Delft, The Netherlands.
- Linde, R.Q. van der and Schwab, A.L. (2011). “*Multibody dynamics b*”. URL <http://bicycle.tudelft.nl/schwab/wb1413spring2012/MultibodyDynamicsB.pdf>.
- Liu, W. and Nigg, B.M. (2000). “*A mechanical model to determine the influence of masses and mass distribution on the impact force during running*”. Journal of Biomechanics, 33(2), pp. 219–224.
- McGeer, T. (1990a). “*Passive bipedal running*”. Proceedings of the Royal Society of

- London. Series B, Biological Sciences, 240(1297), pp. 107–134.
- McGeer, T. (1990b). “*Passive dynamic walking*”. The International Journal of Robotics Research, 9(2), pp. 62–82.
- McMahon, T.A. and Cheng, G.C. (1990). “*The mechanics of running: How does stiffness couple with speed?*” Journal of Biomechanics, 23(SUPPL. 1), pp. 65–78.
- Millard, M., Wight, D., McPhee, J., Kubica, E., and Wang, D. (2009). “*Human foot placement and balance in the sagittal plane*”. Journal of Biomechanical Engineering, 131(12), p. 121001.
- MIT Leg Laboratory (2012). “*Website MIT leg laboratory*”. URL <http://www.ai.mit.edu/projects/leglab>.
- Mombaur, K.D., Longman, R.W., Bock, H.G., and Schloder, J.P. (2005). “*Open-loop stable running*”. Robotica, 23(01), pp. 21–33.
- Morris, B., Westervelt, E.R., Chevallereau, C., Buche, G., and Grizzle, J.W. (2006). “*Achieving bipedal running with rabbit: Six steps toward infinity*”. Fast Motions in Biomechanics and Robotics, volume 340 of *Lecture Notes in Control and Information Sciences*, pp. 277–297.
- Müller, R. and Blickhan, R. (2010). “*Running on uneven ground: Leg adjustments to altered ground level*”. Human movement science, 29(4), pp. 578–589.
- Nagasaka, K., Kuroki, Y., Suzuki, S., Itoh, Y., and Yamaguchi, J. (2004). “*Integrated motion control for walking, jumping and running on a small bipedal entertainment robot*”. Proceedings of IEEE International Conference on Robotics and Automation, volume 4, pp. 3189–3194.
- Niiyama, R. and Kuniyoshi, Y. (2009). “*Design of a musculoskeletal athlete robot: A biomechanical approach*”. Proceedings of 12th International Conference on Climbing and Walking Robots and the Support Technologies for Mobile Machines, pp. 173–180.
- Niiyama, R., Nishikawa, S., and Kuniyoshi, Y. (2012). “*Biomechanical approach to open-loop bipedal running with a musculoskeletal athlete robot*”. Advanced Robotics, 26, 3(4), pp. 383–398.
- Össur (2012). “*Website Össur*”. URL <http://www.ossur.com>.
- Owaki, D. and Ishiguro, A. (2007). “*Mechanical dynamics that enables stable passive dynamic bipedal running-enhancing self-stability by exploiting nonlinearity in the leg elasticity*”. Journal of Robotics and Mechatronics, 19(4), p. 374.

- Owaki, D., Koyama, M., Yamaguchi, S., and Ishiguro, A. (2009). "*A two-dimensional passive dynamic running biped with elastic elements*". Dynamic Walking.
- Owaki, D., Koyama, M., Yamaguchi, S., Kubo, S., and Ishiguro, A. (2010). "*A two-dimensional passive dynamic running biped with knees*". Proceedings of IEEE International Conference on Robotics and Automation, pp. 5237–5242.
- Playter, R., Buehler, M., and Raibert, M. (2006). "*Bigdog*". Proceedings of SPIE, volume 6230, p. 62302O.
- Playter, R.R. (1994). "*Passive dynamics in the control of gymnastic maneuvers*". Phd thesis, Massachusetts Institute of Technology.
- Poulakakis, I. and Grizzle, J.W. (2009a). "*Modeling and control of the monopedal robot thumper*". Proceedings of IEEE International Conference on Robotics and Automation, pp. 3327–3334.
- Poulakakis, I. and Grizzle, J.W. (2009b). "*The spring loaded inverted pendulum as the hybrid zero dynamics of an asymmetric hopper*". IEEE Transactions on Automatic Control, 54(8), pp. 1779–1793.
- Pratt, G.A. and Williamson, M.M. (1995). "*Series elastic actuators*". Proceedings of IEEE/RSJ International Conference on Intelligent Robots and Systems, volume 1, pp. 399–406.
- Pratt, J.E., Carff, J., Drakunov, S.V., and Goswami, A. (2006). "*Capture point: A step toward humanoid push recovery*". Proceedings of IEEE-RAS International Conference on Humanoid Robots, pp. 200–207.
- Pratt, J.E., Chew, C.M., Torres, A., Dilworth, P., and Pratt, G. (2001). "*Virtual model control: An intuitive approach for bipedal locomotion*". The International Journal of Robotics Research, 20(2), p. 129.
- Pratt, J.E., Koolen, T., De Boer, T., Rebula, J., Cotton, S., Carff, J., Johnson, M., and Neuhaus, P. (2012). "*Capturability-based analysis and control of legged locomotion, part 2: Application to m2v2, a lower-body humanoid*". The International Journal of Robotics Research, 31(10), pp. 1117–1133.
- Raibert, M. (1986). "*Legged robots that balance*". MIT press Cambridge, MA.
- Raibert, M., Blankespoor, K., Nelson, G., Playter, R., et al. (2008). "*Bigdog, the rough-terrain quadruped robot*". Proceedings of the 17th World Congress, pp. 10823–10825.
- Raibert, M.H. and Brown Jr, H.B. (1984). "*Experiments in balance with a 2d one-legged hopping machine*". Journal of Dynamic Systems, Measurement, and Con-

- trol, 106, p. 75.
- Raibert, M.H., Brown Jr, H.B., and Chepponis, M. (1984). “*Experiments in balance with a 3d one-legged hopping machine*”. The International Journal of Robotics Research, 3(2), p. 75.
- Raibert, M.H., Brown Jr, H.B., Chepponis, M., Koechling, J., and Hodgins, J.K. (1989). “*Dynamically stable legged locomotion*”. Technical report, DTIC Document.
- Rao, A.V., Benson, D.A., Darby, C., Patterson, M.A., Francolin, C., Sanders, I., and Huntington, G.T. (2010). “*Algorithm 902: Gpops, a matlab software for solving multiple-phase optimal control problems using the gauss pseudospectral method*”. ACM Transactions on Mathematical Software, 37(2), pp. 1–39.
- Reuijl, D.M. (2012). “*Optimal leg compliance for rejecting disturbances in bipedal running*”. Master’s thesis, Delft University of Technology.
- Rummel, J. and Seyfarth, A. (2008). “*Stable running with segmented legs*”. The International Journal of Robotics Research, 27(8), p. 919.
- Saranli, U., Buehler, M., and Koditschek, D.E. (2001). “*Rhex: A simple and highly mobile hexapod robot*”. The International Journal of Robotics Research, 20(7), pp. 616–631.
- Sato, A. and Buehler, M. (2004). “*A planar hopping robot with one actuator: design, simulation, and experimental results*”. Proceedings of IEEE/RSJ International Conference on Intelligent Robots and Systems, volume 4, pp. 3540–3545.
- Schwab, A.L. and Wisse, M. (2001). “*Basin of attraction of the simplest walking model*”. Proceedings of ASME Design Engineering Technical Conferences.
- Schwind, W.J. and Koditschek, D.E. (1997). “*Characterization of monopod equilibrium gaits*”. Proceedings of IEEE International Conference on Robotics and Automation, volume 3, pp. 1986–1992.
- Seyfarth, A. and Geyer, H. (2002). “*Natural control of spring-like running: optimized self-stabilization*”. Proceedings of the Fifth International Conference on Climbing and Walking Robots, pp. 81–85.
- Seyfarth, A., Geyer, H., Günther, M., and Blickhan, R. (2002). “*A movement criterion for running*”. Journal of Biomechanics, 35(5), p. 649.
- Seyfarth, A., Geyer, H., and Herr, H. (2003). “*Swing-leg retraction: a simple control model for stable running*”. Journal of Experimental Biology, 206(15), pp. 2547–2555.

- Sreenath, K. (2011). *"Feedback control of a bipedal walker and runner with compliance"*. Ph.D. thesis, University of Michigan.
- Srinivasan, M. and Ruina, A. (2005). *"Computer optimization of a minimal biped model discovers walking and running"*. *Nature*, 439(7072), pp. 72–75.
- Strogatz, S. (1994). *"Nonlinear dynamics and chaos: With applications to physics, biology, chemistry, and engineering"*. Westview Pr.
- Tajima, R., Honda, D., and Suga, K. (2009). *"Fast running experiments involving a humanoid robot"*. *Proceedings of IEEE International Conference on Robotics and Automation*, pp. 1571–1576.
- Takenaka, T., Gomi, H., Hamaya, K., Takemura, Y., Matsumoto, T., Yoshiike, T., Nishimura, Y., Akimoto, K., et al. (2009). *"Leg joint assist device for leg type movable robot"*. EP Patent 1,442,846.
- Townsend, M.A. (1985). *"Biped gait stabilization via foot placement"*. *Journal of Biomechanics*, 18(1), pp. 21–38.
- Vukobratovic, M. and Juricic, D. (1969). *"Contribution to the synthesis of biped gait"*. *IEEE Transactions on Biomedical Engineering*, BME-16(1), pp. 1–6.
- Weyand, P.G., Bundle, M.W., McGowan, C.P., Grabowski, A., Brown, M.B., Kram, R., and Herr, H. (2009). *"The fastest runner on artificial legs: different limbs, similar function?"* *Journal of Applied Physiology*, 107(3), pp. 903–911.
- Wight, D.L. (2008). *"A foot placement strategy for robust bipedal gait control"*. Ph.D. thesis, University of Waterloo.
- Wight, D.L., Kubica, E.G., and Wang, D.W.L. (2008). *"Introduction of the foot placement estimator: A dynamic measure of balance for bipedal robotics"*. *Journal of Computational Nonlinear Dynamics*, 3(1), 011009.
- Wisse, M. (2004). *"Essentials of dynamic walking; analysis and design of two-legged robots"*. Phd thesis, Delft University of Technology.
- Wisse, M., Atkeson, C.G., and Kloimwieder, D.K. (2005a). *"Swing leg retraction helps biped walking stability"*. *Proceedings of IEEE-RAS International Conference on Humanoid Robots*, pp. 295–300.
- Wisse, M., Atkeson, C.G., and Kloimwieder, D.K. (2006). *"Dynamic stability of a simple biped walking system with swing leg retraction"*. *Fast Motions in Biomechanics and Robotics*, volume 340 of *Lecture Notes in Control and Information Sciences*, pp. 427–443.

- Wisse, M., Schwab, A.L., Linde, R.Q. van der, and Helm, F.C.T. van der (2005b). *"How to keep from falling forward: elementary swing leg action for passive dynamic walkers"*. IEEE Transactions on Robotics, 21(3), pp. 393–401.
- Zeglin, G. and Brown, B. (1998). *"Control of a bow leg hopping robot"*. Proceedings of IEEE International Conference on Robotics and Automation, volume 1, pp. 793–798.

Acknowledgements

A PhD project is something you cannot do without support, especially when it involves the design and construction of experimental hardware, like a running robot. Throughout my PhD project, I have enjoyed the support of a great number of people. In this acknowledgement, I would like to thank a few of them especially.

To start I would like to thank my advisor Martijn Wisse. Many years ago, you incited my interest for walking robots with your enthusiastic demonstrations during an open house of the university. You always managed to motivate me, even when the robot broke down for the umpteenth time. Regrettably, I am your last PhD student to study legged locomotion for now, as your research scope is switched to more applied robotics, where there is not yet use for legged locomotion. I hope that with the ever-increasing performance of walking robots, you will return to this research field someday in the future. Next, I would also like to thank my promotor Frans van der Helm. Despite of your busy schedule, you always tried to give feedback on my papers, even if that meant working way into the night.

For the design and construction of the running robot, I received a lot of help from the technical staff of the lab, Eelko van Breda, Jan van Frankenhuyzen, and Guus Liqui Lung, the staff of the machine shop, Hans Drop, John Dukker, and Andries Oort and HBO-student Dennis Lakerveld. I am grateful for all your help, because I would have never been able to build a robot like this without you guys. Also, you were a great help every time the robot broke down, with your support the robot was up and running again in no time.

During this PhD project, I had the pleasure to coach a number of students. I would like to thank Tim van Oijen, Karin Griffioen, Leonard van Bommel, Niels van der Geld, David Reuijl, and all the BSc students for the pleasant collaboration and I hope that you learned as much as I learned from coaching you.

In addition, I want to thank my roommates, Tomas de Boer, Wietse van Dijk, Shiqian Wang, Michiel Plooi, and Wouter Wolfsdag and all the other colleagues from the Biorobotics Lab for the great times. I loved our discussions during the lunch and the Friday's '4 uur, bier uur'. I think it is great that although our research topics are very diverse, we had very in-depth discussions.

A special thanks also goes to Matt Haberland and Sangbae Kim of the Biomimetic Robotics Laboratory at MIT. It was great working together with you on our joint study into the effects of swing-leg retraction.

Last but not least, I would like to thank my family and friends for their support throughout this PhD project and especially my dear girlfriend, Suzanne, for standing by me. The help of you all, with for example proofreading and cover design, was fantastic. It was not always easy, but with the support of all of you, I made it to the end!

About the author



J.G.D. (Daniël) Karssen was born on August 7, 1981 in Naarden, The Netherlands. His secondary education consisted of a MAVO education at Ministerpark, Naarden (1994-1998) and a VWO education at Sint Vituscollege, Bussum (1998-2001). He received his BSc degree in Mechanical Engineering at Delft University of Technology in 2005, followed by his MSc degree (cum laude) in 2008. From 2008 until 2012, he continued with a PhD project on robotic bipedal running at the Delft Biorobotics Lab at Delft University of Technology of which this thesis presents the final results.

In the past decade, Karssen acquired a wide experience in the development of robotic systems, with a specialty in walking and running bipedal robots. For his final BSc project, he created a walking wheel to study the effect of the ankle joint on the sideways walking stability. In 2006, he did an internship at the robot lab of professor Ruina at Cornell University (USA) where he, as head of the mechanics team, developed a walking robot, capable of walking a marathon. Next, he designed a small passive walker that demonstrates the concept of passive dynamic walking for a tutorial at the Dynamic Walking 2008 conference. Since then this walker is used in a number of courses on walking robots all over the world and is sold at the Science Center in Delft. Most recently, Karssen designed and built a running robot as part of his PhD project, of which a detailed description can be found in Chapter 4 of this thesis.

Propositions

1. Nonlinear leg stiffness greatly improves the disturbance rejection behavior of bipedal runners. (Chapter 2 of this thesis)
2. Placing the torso center-of-mass at the hip joint results in poor disturbance rejection behavior. (Chapter 3 of this thesis)
3. Matching the ground speed with the foot prior to touchdown is not optimal. (Chapters 5 & 6 of this thesis)
4. Telescopic leg models wrongly predict the impact behavior of a kneed leg. (Chapter 6 of this thesis)
5. Runners with leg prostheses should be allowed to compete in the Olympics as long as they do not win any medals.
6. Robotics would benefit from a more scientific approach.
7. Introducing a robotic labor force will not increase unemployment.
8. Turning unknown unknowns into known unknowns is scientifically as important as turning known unknowns into known knowns.
9. The use of ghostwriters for writing scientific papers should be accepted.
10. Scientific papers should read like a comic book, with the figures telling the main message.

These propositions are regarded as opposable and defensible, and have been approved as such by the supervisor prof. dr. F.C.T. van der Helm.

Stellingen

1. Niet-lineaire beenstijfheid zorgt er voor dat tweebeinige renners veel beter met verstoringen kunnen omgaan. (Hoofdstuk 2 van dit proefschrift)
2. Het plaatsen van het massazwaartepunt van het bovenlichaam ter hoogte van de heup zorgt voor een slecht verstoringsgedrag. (Hoofdstuk 3 van dit proefschrift)
3. Het is niet optimaal om de voet stil te houden ten opzichte van grond vlak voor het neerkomen. (Hoofdstukken 5 & 6 van dit proefschrift)
4. Telescopische beenmodellen voorspellen het botsingsgedrag van een been met knie slecht. (Hoofdstuk 6 van dit proefschrift)
5. Zolang ze geen medailles winnen zouden hardlopers met beenprotheses moeten kunnen meedoen aan de Olympische Spelen.
6. Robotica is gebaat bij een meer wetenschappelijke aanpak.
7. Het inzetten van robots zal niet leiden tot een hogere werkloosheid.
8. Het vinden van problemen is wetenschappelijk net zo belangrijk als het vinden van oplossingen voor problemen.
9. Het inzetten van een ghostwriter voor het schrijven van wetenschappelijke artikelen zou moeten worden toegestaan.
10. Wetenschappelijke artikelen zouden moeten lezen als een stripboek, waarbij de plaatjes de hoofdboodschap vertellen.

Deze stellingen worden oponeerbaar en verdedigbaar geacht en zijn als zodanig goedgekeurd door de promotor prof. dr. F.C.T. van der Helm.

Robotic **Bipedal** Running

In the last decade, increasingly more prostheses for running are used successfully. The most well-known example is the paraplegic runner Oscar Pistorius, who managed to reach the semifinals of the 400m at the normal Olympics in 2012. To improve these prostheses even further more insight in the fundamentals of the human running gait is needed. In order to study the human running gait, the humanlike running robot Phides was developed. With this robot, an important part of the running gait was studied: the ability to handle disturbances, like sudden pushes or variations in floor height. The results of this research show that there are many opportunities to improve the disturbance rejection performance of bipedal running robots. In conclusion suggestions are given for improving future running prostheses, such that one day a paraplegic might win an Olympic medal!

